Freie Universität Berlin

Tunable plasmonic properties of nanostructures fabricated by shadow nanosphere lithography

Im Fachbereich Physik der Freien Universität Berlin

zur Erlangung des Grades eines

Doktors der Naturwissenschaften (Dr. rer. nat.)

eingereichte Dissertation

vorgelegt von

Piotr Patoka

aus Września, Polen

Institut für Experimentalphysik der Freien Universität Berlin

2011

Erstgutachter: Prof. Dr. Michael Giersig
Zweitgutachterin: Prof. Dr. Stephanie Reich
Tage der Disputation: 01.06.2011

After a certain high level of technical skill is achieved, Science and Art tend to coalesce in esthetics, plasticity, and form. The greatest scientists are always artists as well.
Albert Einstein

To my wife Anna

1. Introduction

The accelerating pace of discovery and innovation leads to converging of different areas of knowledge, which resulted in the emergence of new branches of science; nanotechnology is a prime example. Nanotechnology as a term is a direct result of the need of miniaturization. It describes the technology of manufacturing objects on a nanometer scale in a controllable way, leading to real-world applications. Nowadays, applications can be found in various fields such as nanoelectronics, security, information, medicine, and biotechnology. Furthermore, nanotechnology is the main motor in design and production of new and advanced materials. Most likely, nanotechnology will have an impact on the 21-century mankind similar to that semiconductor technology had during the last decades [1-3].

In fundamental research the focus of nanotechnology is mainly split in two. The first is the production and improvement of various manufacturing techniques, which aim in obtaining high quality structures while simultaneously reducing production costs to be able to compete with semiconductor technology. The second contains the characterization and fundamental understanding of the prepared systems. The research already led to the discovery of new and exciting material properties pushing the boundaries of the quantum world. As an example let us mention the optical response of metallic nanostructures, which takes place on a scale far below the classical diffraction limit of light. In the past 20 years these discoveries led to the vivid field of plasmonics, which explores the physics of surface plasmons. In the meantime a gradual change in focus can be observed in the plasmonics community leading to more efforts in designing applications. This change has emerged because the industrial needs in this field like optical data storage, lithography, and high density electronics approach fundamental limits. It is likely possible to overcome some of the technological challenges by applications exploiting the unique plasmonic properties of materials. Recent studies on plasmonic properties of materials lead to the

development of new plasmon – based optical elements and techniques, which are already in use. This includes waveguides, biosensors, optical- switches, and improvement in surface enhanced Raman spectroscopy (SERS) [4]. But these studies also led to the emergence of the phenomenon of SPASER (surface plasmon amplification by stimulated emission of radiation) which was first described in 2003 by Bergman and Stockman [5] and already announced in 2009 [6], or high harmonic generation mediated by plasmons [7]. The surface plasmons let finally overcome the limit of optical data storage [8-11], and found a broad application in bio-medicine for photostable labels, biosensors [12] and for thermal cancer therapy [13, 14]. For the last two decades, the interest in surface plasmons has grown, as can been seen by the number of publications on that topic, which increases by a factor of two every 5 years [15].

Recently, metal nanostructures have received considerable attention due to their ability to guide and manipulate light at the nanoscale and the pace of new inventions in the area has accelerated even further. The trigger was released by three milestones in plasmonics. In 1997 Takahara and coworkers suggested that metallic nanowires enable the guiding of optical beams with nanometer scale diameter [16]. Following that in 1998 Ebbesen and coworkers reported on the extraordinary optical transmission through subwavelength apertures in metal films which is supported by surface plasmons [17] and in 2000 Pendry suggested a possibility to use a thin metallic film as a perfect lens [18], which was actually a confirmation of theoretical predictions done by Veselago [19]. Definitely these findings had a great influence on most recent research on waveguides [20, 21] and metamaterials [22, 23]. The investigation of the plasmonic properties of samples requires structured surfaces (since surface plasmons cannot be excited on a planar flat film). However, the techniques for preparation of samples with structures in the nanometer range are expensive and limited to a small number of materials. Thus, they often stay in the way of the advance in science, leaving some place for much cheaper fabrication methods and investigation for new material properties.

1.1 Scope of this work

The scope of this thesis is to find an answer to the question, if and how one can manipulate the optical responses of specimen by use of different nanostructures and various materials. The realization of this aim was obtained in two steps. The first one includes the fabrication and structural investigation of large area (> cm^2) arrays of

nanostructures of different morphology, which are prepared using a lithographic method based on a self-assembly of two-dimensional colloidal crystals. The second one includes the optical characterization of the obtained nanostructures and investigation of the influence of the structure on the plasmonic response of light matter interaction like surface plasmon / polariton, extraordinary light transmission as well as coupling of surface plasmons to different nanostructures. Mechanisms of the interaction of light with structures such as quasitriangluar nanoislands, arrays of subwavelength holes or nanowires are addressed and discussed here. We are focused on investigations of the influence of the structure's geometry on the optical responses, especially on those induced by light in combination with metal surface plasmons. Since, these nanostructures form arrays, thus the diffraction of light and accompanying effects are expected, including Wood's anomaly. On this basis, we would like to show that the plasmonic response is tunable, and efficiently controlled by the morphology of the fabricated structures.

The outline of this work is divided as follows: At first, theoretical considerations on the topic of plasmonics will be presented to fully understand the processes, which take place during the interplay of the light with the metallic structures. Following that the experimental part will give an insight in the preparation of the various nanostructures used throughout the thesis and also present the characterization of the samples. The main part of the thesis will then focus on the investigation and discussion of the plasmonic properties of the prepared structures. An outlook to possibilities and future experiments will close the thesis.

2. Theoretical background

In this section we will present the theoretical background that is necessary to understand the experimental results. The main question that we want to address here is: What exactly is the field of plasmonics?

2.1 Plasmonics as a discipline

In the very vibrant field of nanophotonics where the interaction of electromagnetic radiation with structures of sizes comparable to or smaller than the wavelength is studied, plasmonics is by far the most vivid.

The basis of plasmonic processes lies in the interaction of the radiation with the conduction electrons in the metallic structures. These range from corrugated surfaces and interfaces to structures of nanometers in size. In these so called nanoparticles, confinement of the plasmons lead to large enhancements in the electromagnetic field in dimensions smaller than the wavelength, i.e., in the truly subwavelength regime. Hence scientists seek to harness this resonant interaction to control light on a subwavelength scale and thus to manipulate interactions between light and matter. The notion of plasmonics is a description of the science and technology of metal based optics.

Plasmonics as a field of science and technology is not older than a decade. Yet its origins lie in the turn of XX century, when the foundations of two important ingredients of this branch of science were lain – surface plasmon polaritons and localized plasmon resonance. First, Sommerfeld theoretically studied electromagnetic surface modes on metal wires. He calculated the solution of Maxwell's equations for wave propagation along a cylindrical metal surface [24]. These surface modes, also called surface waves for radio waves, are electromagnetically equivalent to and thus are a direct predecessor for surface plasmons polaritons in the visible domain. Nearly a

decade later, in 1908, Gustav Mie established a clear mathematical foundation on scattering of light on small spherical particles [25]. This formalism was later applied by successors as fundamentals for description of localized surface plasmon resonances in metallic nanoparticles. Some details about this approach will be presented in the following section.

Throughout the 20th century both of phenomena have been rediscovered in a variety of different contexts. Nowadays, the variety of topics on plasmonics derives in part from important developments in experimental and numerical techniques trying to match the results of experiments with those of theory [26]. Some of the areas of possible plasmonic applications that are either already being investigated or are being considered are presented in the diagram [Fig. 2.1]

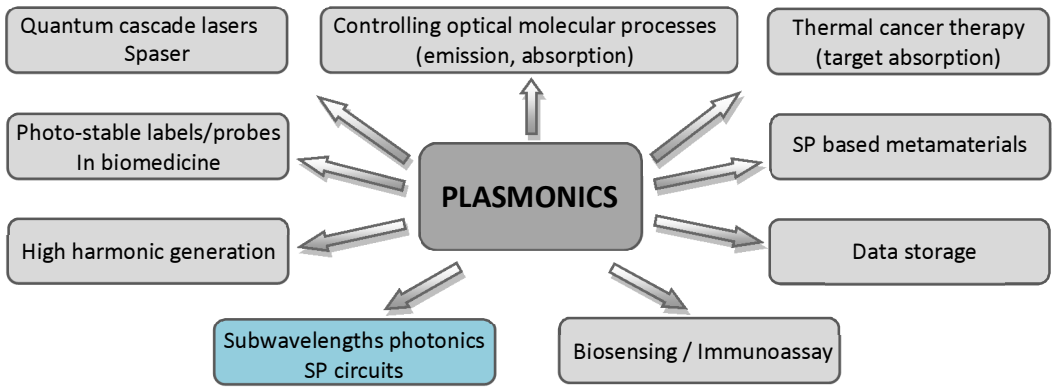

Fig. 2.1 *Importance of plasmonics in the confinement and control of light in the subwavelength regime [26].*

2.2 Theoretical considerations on Plasmonics

In this section, we will give a short introduction to surface plasmons and their dispersion relation. Prior to the explanation, a short glance back will be given and the theoretical models of Drude, Mie, and Gans will shortly be described because of their importance to the field of plasmonics.

2.2.1 Mie theory

Relative simplicity and versatility are the advantages of the classical Mie theory suggested by Gustav Mie in 1908 [25], which describe the mechanism for the absorption of light by small metal particles by solving Maxwell's equations. The theory

is based on the assumptions that while the electromagnetic field interacts with the particle an induced charge separation on the particle's surface succeed. This charge separation is a cause for an occurring restoring force. It has been shown that such absorption of light in the UV-Vis region by metallic particles is sensitive to many geometrical as well as environmental factors [27]. Solving Maxwell's equations lead to a relationship for the extinction cross-section for metallic nanoparticles

$$\sigma_{ext} = \sigma_{abs} + \sigma_{sca} \qquad \text{(Eq. 2.1)}$$

where σ_{ext} , σ_{abs} , σ_{sca} are the extinction, absorption and scattering cross-section, respectively.

Although both absorption and scattering processes occur simultaneously, there are incidents where either one of the two dominates. Taking into account small particles in comparison to the wavelengths of the light (particle radius $R \ll \lambda$) only absorption is significant. Using a complex expression for the dielectric constant [Eq. 2.2]

$$\varepsilon(\omega) = \varepsilon'(\omega) + i\varepsilon''(\omega) \qquad \text{(Eq. 2.2)}$$

where $\varepsilon'$and ε'' are the real and imaginary part of the dielectric function of the metallic nanoparticles, respectively, while ω is the angular frequency of the exciting radiation according to the Drude model [28]. Based on the assumptions that the particles are spherical, small, and embedded in an isotropic and non-absorbing medium with a dielectric constant $\varepsilon_m = n_m^2$, Mie calculated the extinction cross section of such solution where its real part is given by Eq. 2.3.

$$\sigma_{ext}(\omega) = 9\frac{\omega}{c}\varepsilon_m^{\frac{3}{2}} V_0 \frac{\varepsilon''(\omega)}{[\varepsilon'(\omega) + 2\varepsilon_m]^2 + \varepsilon''(\omega)^2} \qquad \text{(Eq. 2.3)}$$

where $V_0 = (4\pi/3)R^3$ is the volume of the spherical nanoparticle, c is the vacuum velocity of light, ε_m accounts for the dielectric constant of the host medium.
The above equation determines the shape of the absorption band of the particles. The bandwidth and the peak height are well approximated by $\varepsilon''(\omega)$. The position of the maximum absorption occurs when $\varepsilon'(\omega) \approx -2\varepsilon_m$ if $\varepsilon''(\omega)$ is small or if it is only weakly dependent on ω. One can also see from Eq. 2.3 that no size dependence of the peak position is predicted. Contrary to the theory, size dependence is observed in many experimental results [29-33]. From Eq. 2.3 one can deduce two limiting cases for which σ_{ext} is equal to zero. In the first case, the complex part for the dielectric

constant is zero ($\varepsilon''(\omega) = 0$), i.e., the particle is non-absorbing (this applies to dielectric materials, i.e., quartz or sapphire, which do not absorb in visible range, that is why they are used as a substrates for transmission measurements). In the second case ($\varepsilon''(\omega) \to \infty$), the material reflects all of incoming radiation at this wavelength, i.e., the complex part of the dielectric function for metals has a large value in the visible making them very shiny and totally reflecting for the incoming light. Since the shape of nanoparticles is not limited to spherical, Mie's model had to be extended for other morphologies.

2.2.2 Gans theory

In 1912 Richard Gans presented his modification of the Mie theory, which extended the expression for the extinction cross-section of spheres to ellipsoidal particles [34]. With this expression the calculation of the absorption resonance for rod-like nanoparticles can be achieved.

Due to the ellipsoidal shape, two fundamental oscillation directions for the conduction electrons exist; the principle of these electronic oscillations named plasmons is introduced in section 2.2.4. The first one is along the short axis of the ellipsoid, the second one along the long axis. Both oscillations induce a charge separation and thus a localized plasmon resonance in the nanoparticle. The extinction cross-section [Eq. 2.4] proposed by Gans considered an ellipsoid that dimensions fulfill the condition: a > b = c as shown in Fig. 2.2.

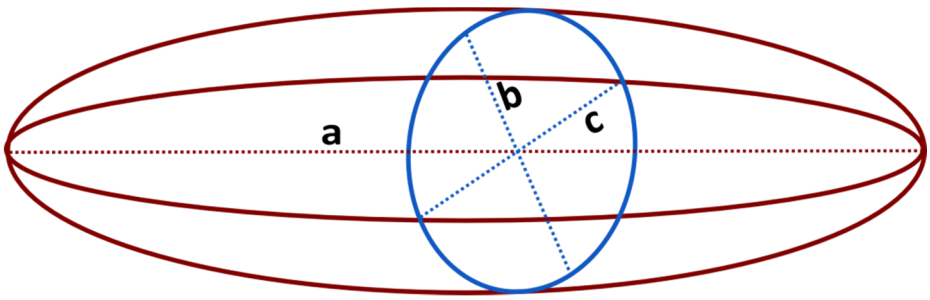

Fig. 2.2 *Schematic of an ellipsoidal particle with dimensions: a > b = c, where a is the dimension of the longitudinal axis, b and c are the dimensions of the transverse axes.*

$$\sigma_{ext}(\omega) = \frac{\omega}{3c}\varepsilon_m^{\frac{3}{2}} V_e \sum_j \frac{\left(\frac{1}{P_j^2}\right)\varepsilon''(\omega)}{\left[\varepsilon'(\omega) + \frac{1-P_j}{P_j}\varepsilon_m\right]^2 + \varepsilon''(\omega)^2} \quad \text{(Eq. 2.4)}$$

where P_j are the depolarization factors along the three axes of the ellipsoid, $V_e = \frac{4}{3}$abc is the volume of the ellipsoid, in this case b=c, thus $V_e = \frac{4}{3}ab^2$.

The depolarization factors P_j express a quantity of the force which seeks to restore the initial electron distribution along each of the axes of the ellipsoid [35]. They are defined as [36]:

$$P_a = \frac{1-e^2}{e^2}\left[\frac{1}{2e} ln\left(\frac{1+e}{1-e}\right) - 1\right] \quad \text{(Eq. 2.5)}$$

$$P_b = P_c = \frac{1-P_a}{2} \quad \text{(Eq. 2.6)}$$

where *e* is the ellipticity of the ellipsoid, which refers to its aspect ratio (long axis / short axis) and is denoted by

$$e = \sqrt{1 - \left(b/a\right)^2} \quad \text{(Eq. 2.7)}$$

These modifications give rise to two possible plasmon modes (longitudinal and transverse) for ellipsoidal nanoparticles. The longitudinal mode is thereby strongly dependent on the aspect ratio.

In the case of many metals, the region of absorption up to the bulk plasma frequency ω_p is dominated by the free electron behavior. Thus the dielectric response is well described by the simple Drude model, which will shortly be introduced in the following section.

2.2.3 Drude model

In 1900 German physicist Paul Drude, presented a new and audacious theory of electrical and thermal conduction of metals by applying the highly successful kinetic theory of gases to a metal, considered as a gas of electrons [37, 38]. Drude's model assumes that the conduction electrons in the metal can be treated like the molecules

in the kinetic gas theory. He proposed that the electrons are moving while the positive ionic background of the metal is immobile. During their flight, the electrons will constantly scatter on both the positive background as well as with other electrons. The situation is schematically shown in [Fig. 2.3].

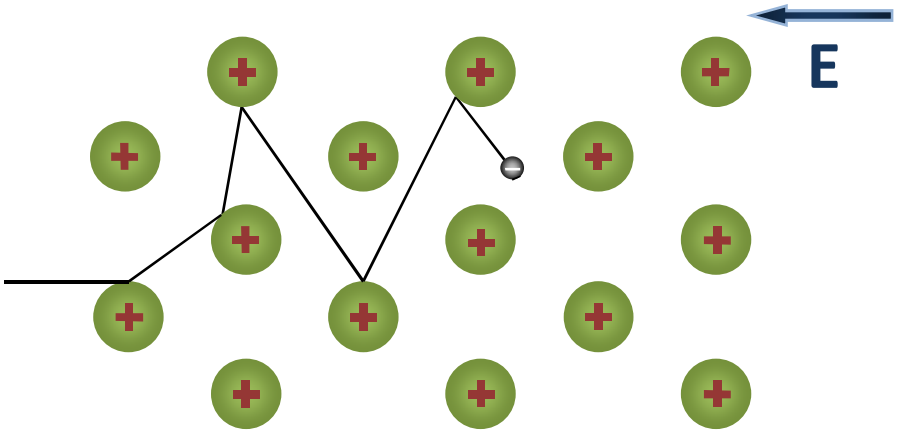

Fig. 2.3 *Drude's model electrons (shown in black) constantly collide between heavier, stationary crystal ions (shown in green).*

According to this free electron model, the dielectric function of such free electron gas can be represented as:

$$\varepsilon(\omega) = 1 - \frac{ne^2}{\varepsilon_0 m\omega^2} \qquad \text{(Eq. 2.8)}$$

where n is the electron density, ε_0 is the vacuum permittivity, e and m are electron charge and mass respectively.

In a medium with an equal concentration of positive and negative charges, the bulk plasma frequency can be represented as:

$$\omega_p^2 = \frac{ne^2}{\varepsilon_0 m} \qquad \text{(Eq. 2.9)}$$

Rewriting Eq. 2.8 with Eq. 2.9 results in the dielectric function given as:

$$\varepsilon(\omega) = 1 - \frac{\omega_p^2}{\omega^2} \qquad \text{(Eq. 2.10)}$$

Introducing of a constant offset ε_∞, which adds the effect of interband transitions at frequencies above plasma frequency, which the Drude model does not include, the dielectric function is denoted:

$$\varepsilon(\omega) = \varepsilon_\infty - \frac{\omega_p^2}{\omega^2} \qquad \text{(Eq. 2.11)}$$

All in this thesis presented models are used to interpret the plasmonic interaction with prepared various nanostructures. In the following section a more detailed description of what plasmons are will be given.

2.2.4 Plasmon

In metals a plasmon can be described as an oscillation of free electron density against the fixed positive ionic background. This oscillation is longitudinal and originates from long-range correlations of the electrons caused by Coulomb forces. To visualize this phenomenon one can imagine a rectangular metal slab which is placed in an external electric field which points to the left [Fig. 2.4]. Electrons will start to move to the right side simultaneously uncovering the positive cores (ions) on the left side. The electron movement will last until they will cancel the field inside the metal. If the external field will be switched off, the electrons will start to move to the left direction, repelled by each other and attracted to the positive ions which were left bare on the left side. The electrons will oscillate back and forth at the frequency given by equation 2.9.

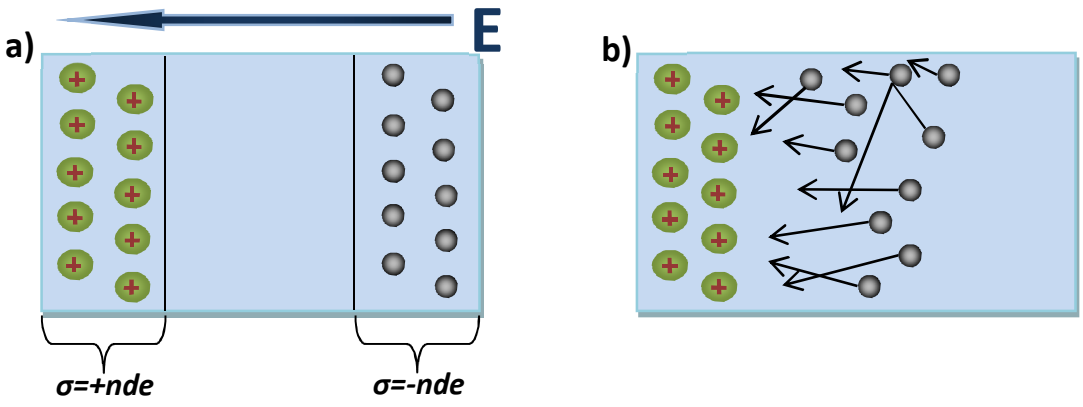

Fig. 2.4 *Simple schematic of plasma oscillations. Green spheres represent fixed positive background of ions and grey spheres represent the electron gas. a) The charges are separated due to the applied external electric field. b) Situation without external field. The electrons move back to cancel the charge separation.*

Such plasma oscillations in gaseous discharges were investigated theoretically and experimentally by Tonks and Langmuir [39]. These collective oscillations of plasma inside the metal with a frequency given by the Drude model (Eq. 2.9) are called volume or bulk plasmons.
Keeping in mind that the dielectric function [Eq. 2.11] is complex and introducing a damping coefficient, one can write:

$$\varepsilon(\omega) = \varepsilon^{\infty} - \frac{\omega_p^2}{(\omega^2 + i\gamma\omega)} \qquad \text{(Eq. 2.12)}$$

where γ represents the damping term, which connects the Fermi velocity and the electron mean free path between scattering events $\gamma = v_F/l$.
The real and imaginary parts of $\varepsilon(\omega)$ are denoted:

$$\varepsilon'(\omega) = \varepsilon_{\infty} - \frac{\omega_p^2}{(\omega^2 + \gamma^2)} \qquad \text{(Eq. 2.13)}$$

$$\varepsilon''(\omega) = \frac{\omega_p^2 \gamma}{\omega(\omega^2 + \gamma^2)} \qquad \text{(Eq. 2.14)}$$

From Eq. 2.13 it can be deduced that for whole frequency regime below the frequency of bulk plasmon of a metal, ε' is < 0. This is due to the electrons oscillating out of phase with the electric field vector of the light wave [32].

The condition where $\varepsilon'(\omega) = 0$ [40], determines the frequency of the longitudinal modes of oscillation. Thus the longitudinal plasma frequency can then be written as:

$$\omega_p^2 = \omega^2 + \gamma^2 \qquad \text{(Eq. 2.15)}$$

The oscillation lasts until the energy is lost due to damping. In a particle picture these oscillations are described as plasmons.
Plasmons play a large role in the optical properties of metals. Incoming light of frequency below the plasma frequency is reflected, because the electrons in the metal screen the electric field of the light. Light of frequency above the plasma frequency is transmitted, because the electrons cannot respond fast enough to screen it. Some metals, like gold and copper, on the other hand have electronic interband transitions

in the visible range, whereby specific colors are absorbed. The bulk plasmon reflects the material properties of a metal but this phenomenon can't carry information about its surface. From the point of view of this work another term has to be introduced, which accounts for these surface contributions, i.e., surface plasmons.

2.2.5 Surface plasmon

An important extension of the physical phenomenon of plasmons has been accomplished by the concept of "surface plasmons" (SPs). They are a result of solving Maxwell's equations giving a surface bound mode at the interface between a metal and a dielectric. In other words surface plasmons are electron oscillations that can exist at the interface of any two media, which have to fulfill one condition: the real part of the dielectric function of the materials has to change sign across the interface (e.g. a metal-dielectric interface: sheet in air, or thin film on a glass). In this interaction, the free electrons respond collectively by oscillating in resonance with the light wave. SPs have a lower energy than bulk plasmons.

The frequency ω of these longitudinal oscillations is tied to the wavevector k_{SP} by the dispersion relation $\omega(k_{SP})$. The wavevector k_{SP} lies parallel to the surface; $k_{SP} = 2\pi/\lambda_p$, where λ_p is the wavelength of the plasma oscillation. Solving Maxwell's equations under the appropriate boundary conditions yields the SP dispersion relation in the medium [41, 42], i.e., the frequency-dependent SP wavevector:

$$k_{SP} = k_0 \sqrt{\frac{\varepsilon_m \varepsilon_d}{\varepsilon_m + \varepsilon_d}} \qquad \text{(Eq. 2.16)}$$

where: ε_m is frequency-dependent permittivity of the metal , and ε_d the permittivity of the dielectric material, $k_0 = \omega/c$ is the free space wavevector.
SPs couple with a photon, the resulting hybridized excitation is called a surface plasmon polariton (SPP) [43]. This SPP can propagate along the surface of a metal [Fig. 2.5] until energy is lost either via absorption in the metal or radiation into free-space under some special conditions. The detailed description of this process is given below in section 2.2.6.

The existence of surface plasmons was first predicted in 1957 by R.H. Ritchie [44]. In the following two decades, surface plasmons were extensively studied by many scientists [41, 45-47].

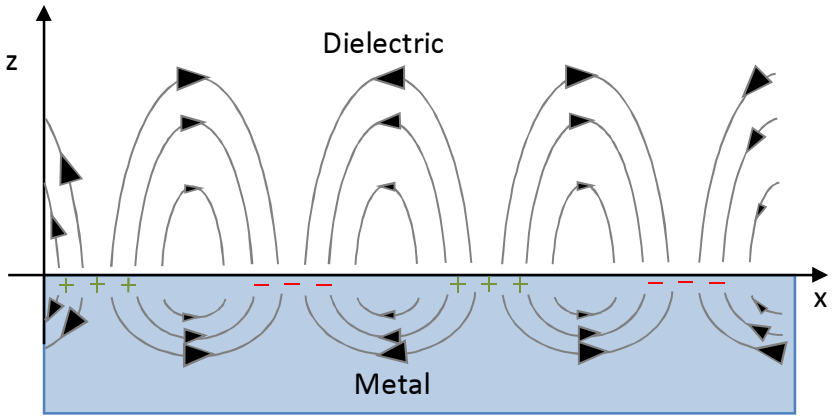

Fig 2.5 *Schematic diagram illustrating a surface plasmon polariton (after) [48].*

Since surface plasmons can be excited on any metal – dielectric interface, they will appear at large surfaces as well as on small ones like nanoparticles. The following section is devoted to surface plasmons on small particles.

2.2.6 Localized surface plasmons of spheres and rods

The dimensions of metallic nanoparticles are so small that light can easily penetrate the whole nanoparticle and grasp at all conduction band electrons. As mentioned in sections 2.2.1 and 2.2.2, the result of the electromagnetic wave and particle interaction is that the sea of conduction band electrons is displaced with respect to the positively charged ions that form the metallic lattice [Fig. 2.6]. These oscillations do not propagate on large distances, but only occur within the particle size. Hence, they are called localized surface plasmon and the frequency of these oscillations is the localized surface plasmon resonance (LSPR). Similar to the surface plasmon, the LSPR is sensitive to changes in the local dielectric environment (i.e. the local density of optical states (LDOS)) e.g. spherical shape) and size (i.e., for particles bigger than 20 nm) [30, 49-52] and to aspect ratio (e.g. ellipsoidal particles) [36, 53].

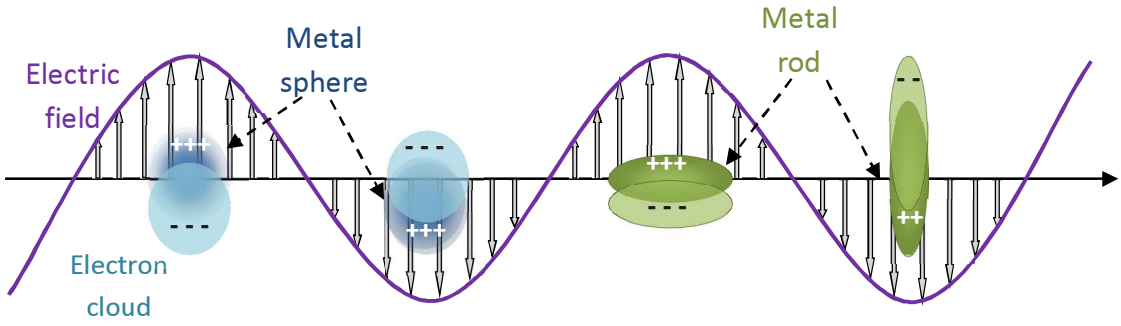

Fig. 2.6 *Schematic illustration of the excitation of dipolar surface plasmon oscillations. The electric field of an incoming electromagnetic wave induces a polarization of the free electrons with respect to the much heavier ionic core of a nanoparticle. A net charge difference is only felt at the nanoparticle boundaries (surface) which in turn acts as a restoring force. In this way a dipolar oscillation of electrons is created – a localized surface plasmon resonance. In the case of rods (right hand side of the image) two oscillations the longitudinal and transverse surface plasmon resonances can be excited.*

2.3 Coupling to surface plasmons - Surface plasmons on grids

As already mentioned, the interaction between the surface charges and the electromagnetic field results in the excitation of SPPs. Their dispersion relation $\omega(k_x)$ lies right of the light line, which means that the surface plasmon polaritons have a larger wavevector than light waves of the same energy $\hbar\omega$, propagating along the surface [Fig. 2.7] [41].

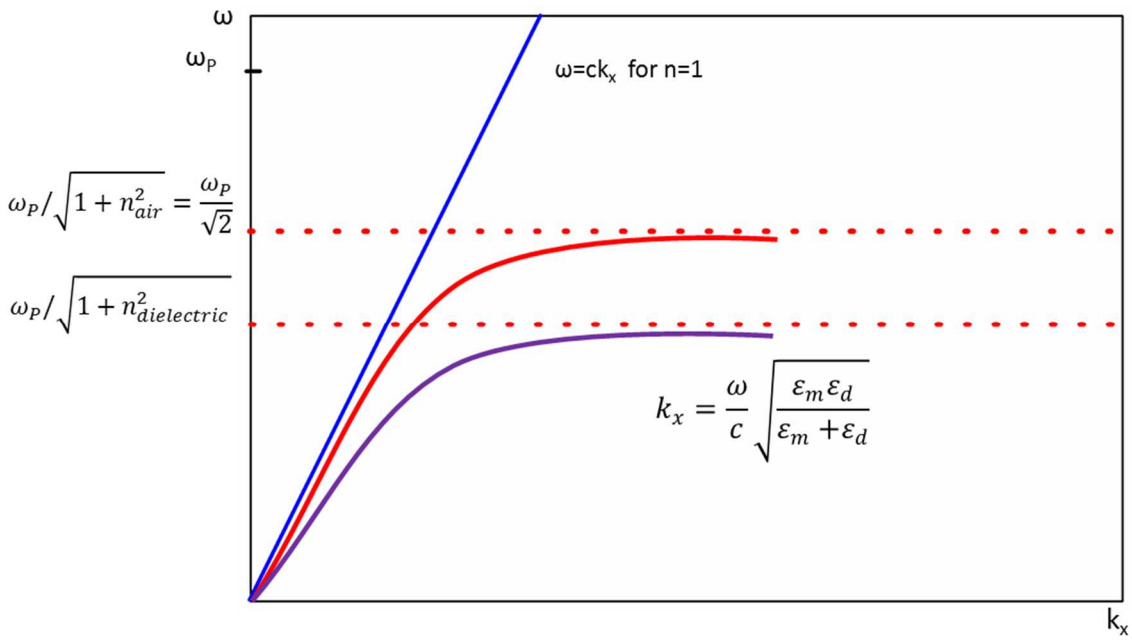

Fig. 2.7 *Dispersion curve for surface plasmon polaritions. For small wavevectors k_x, the surface plasmon polariton curve (red) approaches the light line (blue).*

To obtain a resonant excitation one needs a frequency and momentum matching of the incoming light and the surface plasmon polariton. From the dispersion relation it is obvious that there is a momentum mismatch between the incoming light and the surface plasmon so that coupling is prohibited. To efficiently couple the light to a surface plasmon two rules have to be obeyed. First, the momentum has to be conserved to make coupling physically possible, and second, one has to match the light frequency to the excitation frequency of the SP. There are three main techniques by which the missing momentum can be provided. The first one makes use of prism coupling to enhance the momentum of the incidence light [47, 48]. The second one involves scattering from topological defects on the surface, such as subwavelength protrusions or holes, which provide a convenient way to generate SPs locally [54, 55]. The third method makes use of a periodic corrugation of the metal's surface [56], widely described by Raether [41]. Indeed, already in 1902 Wood reported anomalous behavior in the diffraction of the light by metallic diffraction gratings [57] – some of these phenomena are known to arise from coupling to SPs. The diffraction (scattering) of light by a metallic diffraction grating allows incident light to be momentum matched and thus coupled to SPs [41]. Importantly the reverse process also allows the

otherwise non-radiative SP mode to couple with light in a controlled way with good efficiency [58, 59], which is relevant for developing SP – based photonic circuits.

2.3.1 One dimensional wire gratings

In case of one-dimensional metallic wire-like gratings the coupling of a photon to the surface plasmon is possible when momentum is conserved. This can take place when the structure is illuminated with TM (transverse – magnetic) – polarized light (p-polarization) where the $\vec{E}$ field vector is perpendicular to the wires. Additionally the free-space wavevector k_0 is perpendicular to the wires and forms an angle θ_0 with the normal vector of the grating plane. Then the photons couple to the surface plasmons with a momentum transfer nG ($n = \pm 1, \pm 2, \pm 3 \ldots$) delivered by the grating, where $G = 2\pi/d$ is the reciprocal lattice vector, n is the coupling order and d is a grating period. For this particular case the SPs can be excited when the relation [41, 60, 61]:

$$\pm k_{SP} = k_0 \sin\theta_0 \mp nG \qquad \text{(Eq. 2.17)}$$

is fulfilled. Thereby k_{SP} denotes the momentum of the SP wavevector.
In other words, SPs are excited although the wavevector $\vec{k}_{SP}$ differs from the momentum component of the incident photons because of momentum transfer from the grating.
For normal incidence ($\theta_0 = 0°$) equation 2.17 simplifies to:

$$\pm k_{SP} = \mp nG \qquad \text{(Eq. 2.18)}$$

2.3.2 Square and hexagonal hole arrays

The presented method of providing the missing momentum also includes the cases of a subwavelength hole array or periodic corrugations in the film. The basic principle of coupling photons to surface plasmons for such two dimensional arrays is similar to the one dimensional case of wire gratings. In the two dimensional case the periodicity of the lattice plays a more important role and includes the symmetry properties of the arrays. The use of a square lattice was studied in detail by Ebbesen and coworkers who in 1998 presented that coupling of photons to SPs on a square array of subwavelength holes of cylindrical shape is possible [17]. This publication gave the start point to the

field of plasmonics. The excitation of oscillations of surface charges at the metal interface is possible if their momentum matches the momentum of the incident photon and the grating as follows:

$$k_{SP} = k_x \pm iG_x \pm jG_y \quad \text{(Eq. 2.19)}$$

where, $k_x = (2\pi/\lambda)\sin\theta_0$ is the component of the incident photon's wavevector in the plane of the array and $G_x = G_y = 2\pi/a_0$ are the grating momentum wavevectors for a square array, and a_0 is a grating periodicity (interhole distance).

From Eq. 2.16 it follows that the two interfaces to the metallic film are distinguishable, i.e., if the hole array was deposited on a glass substrate then one has to take into account the air-metal and metal-glass substrate interface while resonant modes have different energies on each side. At normal incidence ($\theta_0 = 0°$) Eq. 2.16 and Eq. 2.19 reduce to [62]:

$$\lambda\sqrt{i^2 + j^2} = a_0\sqrt{\frac{\varepsilon_m\varepsilon_d}{\varepsilon_m+\varepsilon_d}} \quad \text{(Eq. 2.20)}$$

where λ denotes a wavelength at which the resonance is expected, while i and j are scattering orders of the array, denoted as integers $(0, \pm1, \pm2)$.

In the case of hexagonal arrays, the wavevector for the major crystal orientation will differ from each other. The wavelength at which SP resonances are expected is given by combination of Eq. 2.16 and Eq. 2.19, and including reciprocal unit vectors for hexagonal lattice the Eq. 2.20 changes its form to:

$$\lambda\sqrt{\frac{4}{3}(i^2 + j^2 + ij)} = a_0\sqrt{\frac{\varepsilon_m\varepsilon_d}{\varepsilon_m+\varepsilon_d}} \quad \text{(Eq. 2.21)}$$

2.3.3 Wood's anomalies

Beside the coupling into the surface plasmons, the incoming light on to the gratings of various morphology can induce a different effect, namely Wood's anomaly [63]. It occurs when light diffracted by the metal grating becomes tangential to the metal

surface and is not transmitted through the sample. The conditions for the occurrence of the Wood's anomaly are similar to those for coupling of the light into surface plasmons (Eq. 2.19), with only one difference: the k_{SP} has to be replaced by the wavevector of the grazing light. The latter one has a magnitude of:

$$k_{WA} = \frac{2\pi\varepsilon_d}{\lambda} \qquad \text{(Eq. 2.22)}$$

Thus, in case of hexagonal lattice the wavelengths at which Wood anomalies are expected for normal incidence is denoted:

$$\lambda_{WA} = \frac{a_0}{\sqrt{\frac{4}{3}(i^2 + j^2 + ij)}}\sqrt{\varepsilon_d} \qquad \text{(Eq. 2.23)}$$

2.3.4 Extraordinary light transmission through hole arrays

The transmission properties of a subwavelength hole in a metal film have been under investigation since the first predictions by Bethe [64] in 1944, who predicted that the transmission efficiency of a single subwavelength aperture is scaling as r/λ^4 (where r is a hole radius). Accordingly, for a hole of 150 nm diameter one expects transmission efficiency on the order of 10^{-3}. In 1998 Ebbesen et al. showed that the transmission of light through an array of holes in a silver film exhibits high intensity [62] for certain ranges of wavelengths in the visible regime. This is not in agreement with the predictions of Bethe for a single hole. Thus it was clear that an array by itself acts as an active medium. Ghaemi et.al attributed this extraordinary light transmission to the coupling of light to the surface plasmons [62]. They showed that it is in very good agreement with theory [Eq. 2.20]. These results gave rise to the field of plasmonics, where light is controlled, guided, and manipulated by the nanostructured material.

The square array of holes was prepared by focused ion-beam milling. This technique is very expensive and time consuming leading to a low efficiency, limiting this method to simple shaped structures and small sample volume.

Here, we present a low-cost, fast and efficient method to prepare various nanostructures. We are able to prepare 1D arrays of nanowires, hexagonal arrays of subwavelength holes, as well as triangular shaped nanoislands with hexagonal symmetry.

The question is if one can manipulate the plasmonic responses of the sample with usage of different structures and different materials?

3. Sample preparation and structural characterization

This section contains fundamental information about the sample preparation and structural characterizations of the obtained structures. It includes the basic concept of shadow nanosphere lithography (SNSL), and a description of all lithographic steps. Other techniques which are also involved are discussed, for example, the modification of polystyrene (PS) colloidal crystals by reactive ion etching, and electron beam evaporation, including the shadow approach. SNSL allows for the preparation of structures of various morphology such as arrays of wires, holes, and triangular shaped particles, out of diversified materials [65, 66]. These structures will be further investigated for their plasmonic properties, which leads to a selection of appropriate materials in the fabrication process. Furthermore we present the experimental setups used for the detailed structural characterization of the samples. A discussion about results of characterization of crystal structures composed of arrays of triangles, holes, and wires will be given.

3.1 Colloidal mask preparation

The basis of NSL is a self-assembly of a hexagonal closed-packed (hcp) monolayer of polystyrene (PS) latex spheres [67-73]. Since production of such spheres is well-established on the market there is a huge possibility to choose between various size and chemical stabilization of PS micro and sub-micron spheres, also known as PS latex. Polystyrene spheres used in this work range between 440 and 1710 nm in diameter. Usually latex beads are shipped in water solutions with 4 or 8% concentration of solid which had to be increased. For this purpose centrifugation (Laborfuge 400R, Heraeus)

at 5000-6000 rpm for 15-30 min (depending on sphere size), followed by redispersion in an ethanolic/water polystyrene solution to a concentration of 30% was prepared and thoroughly mixed in a ultrasonic bath (Sonorex, 40 W) for 30 min. The prepared solution was slowly applied on a water surface using a glass pipette. All PS monolayers were assembled inside a 20 cm diameter Petri dish [Fig. 3.1a].

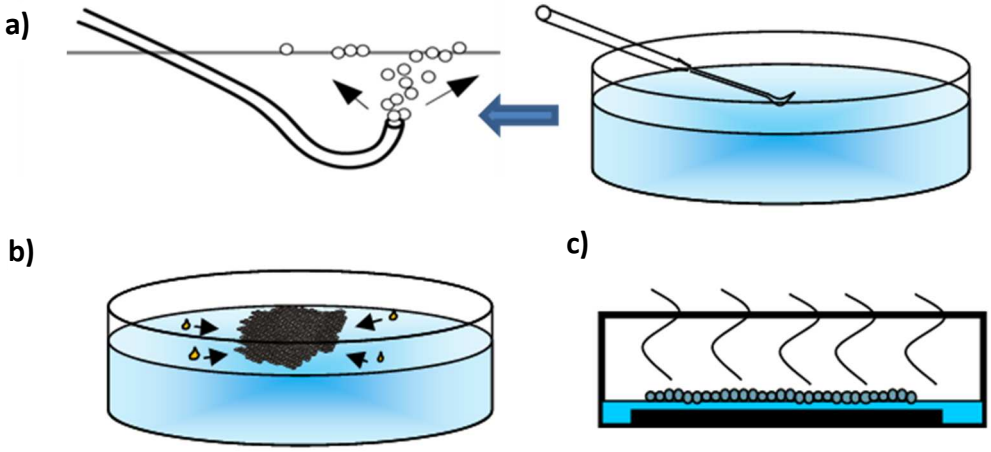

Fig. 3.1 *Colloidal mask preparation: a) applying of the solution to the water surface, b) addition of surfactant - close packing and c) deposition of a monolayer on a substrate.*

During the preparation one has to take into account the amount of the applied solution onto the water surface, leaving some place for stress relaxation and to avoid the formation of cracks in the lattice during the following steps of the preparation. At this stage the monolayer had crystals of 2 cm^2 in size, with very irregular shapes. To promote the growth of large crystals, the beaker was gently tilted to produce waves on the surface. After this treatment, crystals of about 50 cm^2 were created showing clear diffraction colors, which are an indication of the formation of monocrystals.

By adding a small amount of surfactant [Fig 3.1b] a hexagonal close-packed hcp layer of spheres was formed and then anchored with one side to the edge of a Petri dish. Next, the desired substrates needed to be prepared. The samples were cut from wafers into 10x10 mm^2 pieces and pre-cleaned by 5 minutes ultrasonication and rinsing with 2-propanol. Following this, the substrates were submerged for 30-60 minutes in a standard cleaning solution (SC1) [74] of 7% NH_4OH/30% H_2O_2/Milli-Q water (vol. ratio 1:1:5) at 80°C, then rinsed thoroughly in Milli-Q water. The substrates

were put into water at the opposite side of the anchored mask to avoid its destruction, placed at the bottom of the beaker, and aligned under the PS monolayer. Most of the water from the Petri's dish was pumped out slowly (about 50 ml/min) with a membrane pump until the mask nearly touched the surface of the substrate. Finally, the monolayer was deposited onto the substrate by slow evaporation of the rest of the water [Fig. 3.1c].

In Fig. 3.2 we present the results of the PS mask preparation. The first observable effect confirming the formation of a hexagonal crystal structure is the appearance of iridescent colors.

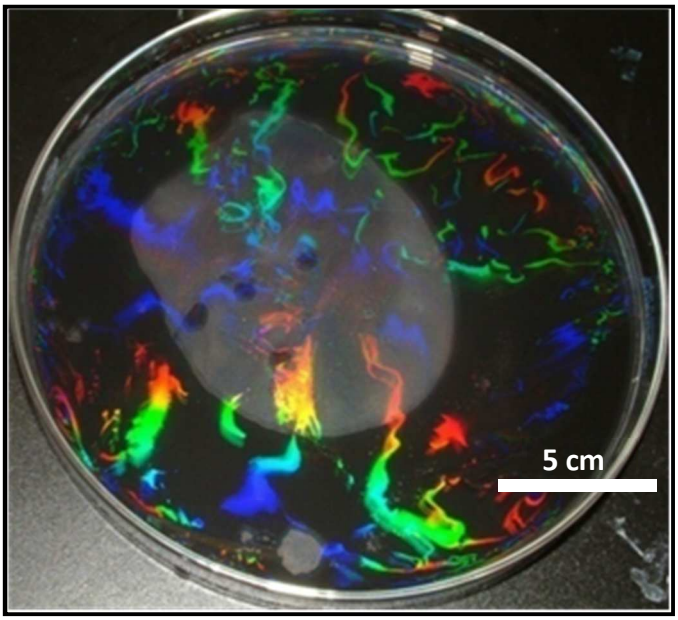

Fig. 3.2 *Photograph of a colloidal mask on a water before close-packing.*

The structure was observed for monolayers that are built of particles with sizes between 440 and 1710 nm. The next step in the sample preparation was the transfer of the mask onto the substrate. The final result of this procedures is presented in Fig. 3.3. Depending on the mask quality, one or more iridescent colors were observed on the surface of the substrates.

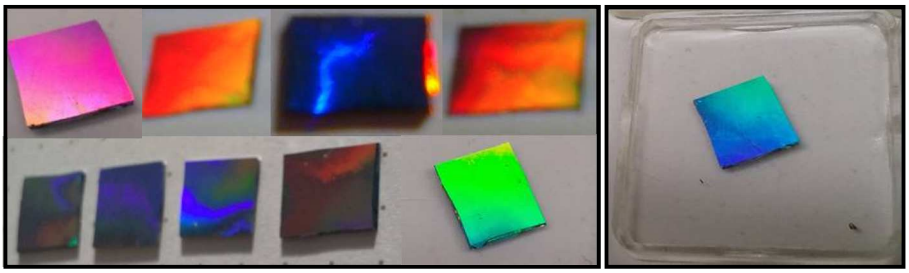

Fig. 3.3 *Photograph of PS-masks on a silicon substrate.*

For more detailed studies the samples were routinely studied with scanning electron microscopy (SEM). In this case SEM - Supra 55 with Gemini® column, from LEO Electron Microscopy Group was used to image the surface of the samples over large areas, which is very helpful to estimate the quality of the final structure. The images were acquired at an acceleration voltage of 2-6 kV for nonconductive, and 3-25 kV for conductive substrates, using an in-lens detector. Figure 3.4 shows exemplary results of the imaging of masks prepared with different sizes of the latex spheres: 440, 720 and 980 nm respectively. One can see that the result of the colloidal mask preparation technique is a monolayer of latex spheres assembled into a lithographic mask and transferred to a solid substrate.

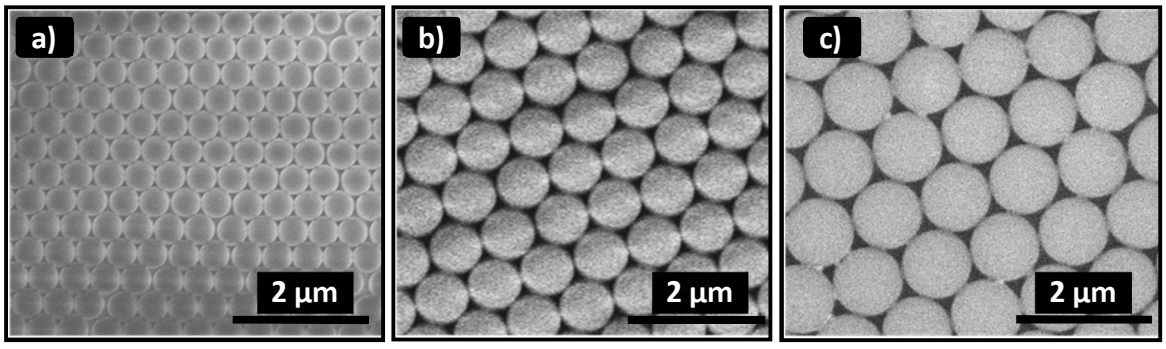

Fig. 3.4 *SEM images of colloidal masks deposited on the substrate. Sphere sizes were: a) 440 nm, b) 720 nm, and c) 980 nm.*

These colloidal masks can be modified by reactive ion etching (RIE), which enhances the NSL to produce structures of different morphologies. The details about this process are presented in the following section.

3.2 Mask modification - RIE

The PS-masks deposited on the substrates can be modified in a post treatment etching process in which the diameter of the spheres can be reduced in a controllable way to a desired size. For this reason previously prepared samples were introduced to the reactive ion etching process (RIE). The RIE process utilizes dissociation and ionization of neutral gas in an alternating electrical field and consists of two simultaneous sub-processes: First ions that were accelerated in an electric field collide with PS molecules and fracture them into radicals. This directional mechanical bombardment is called physical etching. Secondly, at the same time as the physical etching, an isotropic chemical etching caused by highly reactive neutral radicals diffusing to all surfaces proceeds [75]. During the RIE process, the side products of both etching mechanisms are constantly removed from the reaction chamber by a vacuum pump [Fig. 3.5].

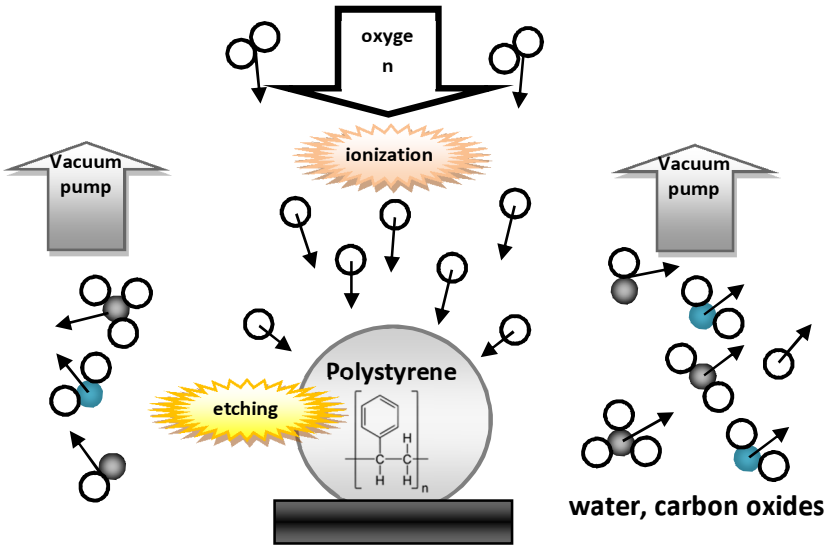

Fig. 3.5 *Reactive ion etching.*

The reactivity ratio: isotropic/anisotropic of sub-processes can be controlled with a content of the procedure in which the most important parameters are the gas composition, plasma energy, pressure, and flow rate of reactive gas as well as the processing time. All details on RIE processes can be found in Ref. [76].

The etching is a very homogeneous process but to assure a good result one needs to fix the latex spheres on the substrates to avoid any movement during further processing. To ensure this, samples covered with latex particles were put on a heating plate at 105°C (temperature is slightly above the glass transition temperature of the PS particles) for ca. 10 s [Fig. 3.6]. This duration was derived experimentally and depends much on the thickness and heat conductivity of the substrate.

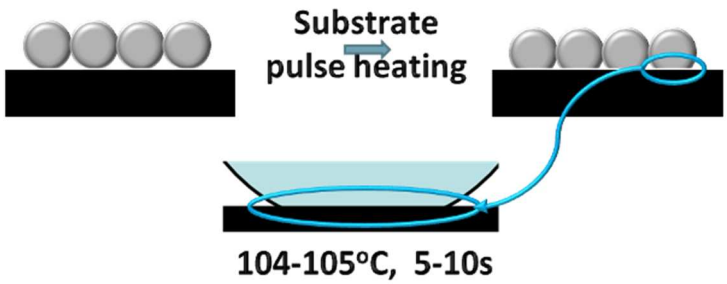

Fig. 3.6 *Fixing of the PS mask to a substrate.*

All samples that needed a RIE mask modification are processed using a Mulitplex Atmospheric Cassette System (MACS) from Surface Technology Systems with the electrodes in the reactor in parallel-plate configurations. PS spheres are etched using a 60 W RF power plasma at a pressure of 8 Pa, while etching ion-compositions include argon and oxygen. The amount of applied gases can vary depending on the size of the used spheres. For smaller spheres (around 500 nm in diameter) one should use more oxygen, which causes that the etching is more aggressive. Such a procedure requires shorter process time. In contrary, for larger particles one should extend the etching duration and reduce the amount of oxygen gas. The process time for needs of this work varied from 0 to 65 seconds.

The results of the etching of the PS sphere masks are presented in Fig. 3.7. PS 440 nm mask is deposited on α-Al_2O_3 substrate, annealed for 5 s at 105°C and etched in periods of 20 – 50 s using Ar/O_2 (10/35 sccm) plasma, driven at 60 W and 8 Pa. The samples were characterized by SEM [Fig. 3.7], showing the reduced size of the spheres while the etching time was extended. Small difference in processing time (5 s) led to noticeable changes in the beads' diameter, starting from not processed 440 nm PS-masks [Fig. 3.7a], the resulting diameters for process durations of 20, 35, 40, 45 and 50 s are 390, 370, 340, 300 and 285 nm respectively [Fig. 3.7b-f].

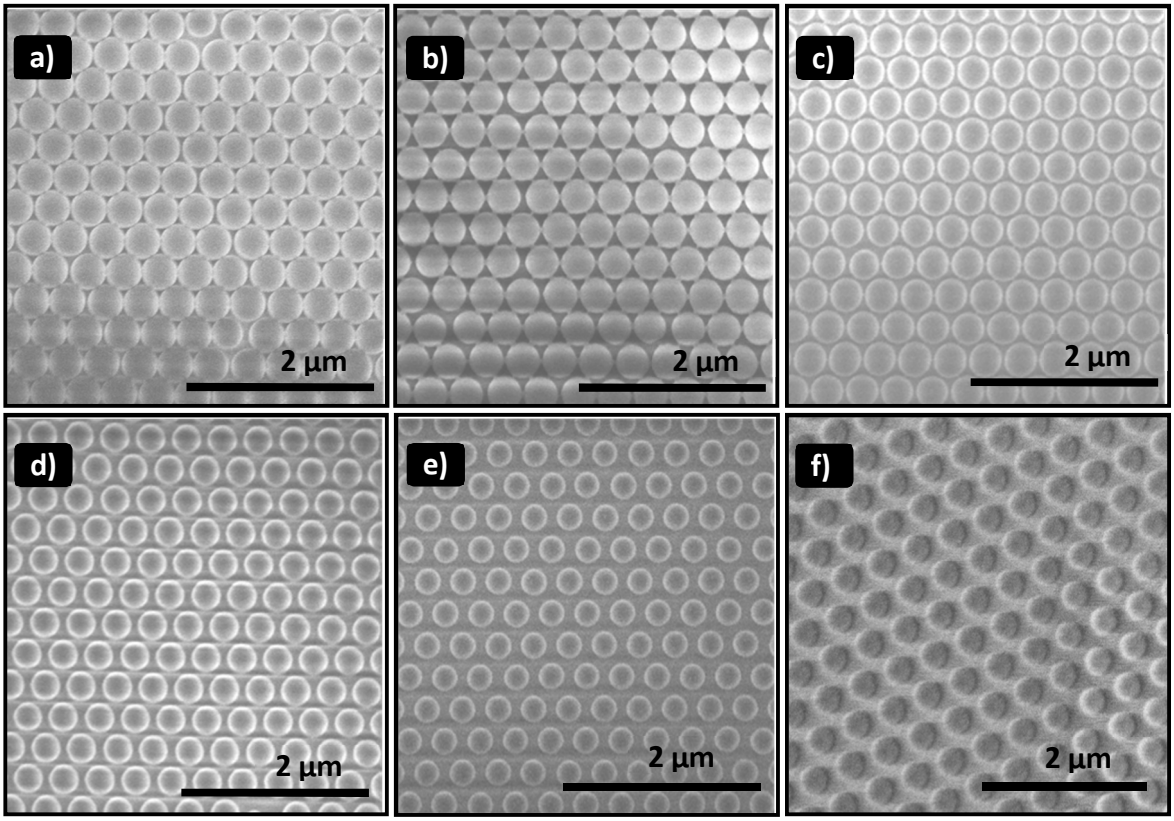

Fig. 3.7 *SEM images of etched PS-masks. RIE process duration: a) 0 s, b) 20 s, c) 35 s, d) 40 s, e) 45 s and f) 50 s.*

It was mentioned in the previous section, that one needs to fix the latex spheres to the substrates before introducing the samples to the reactive ion etching process. The role and results of thermal treatment of the samples is presented in Fig. 3.8. The SEM image [Fig. 3.8a] reveals the power of physical interaction during the RIE process on a not annealed sample. The ion bombardment effects the PS spheres: they are displaced, thus inducing random disorder in the periodic lattice. On the other hand, latex particles which were previously fused to the substrate resist on movement and remain on place during the plasma treatment as shown on Fig. 3.8b.

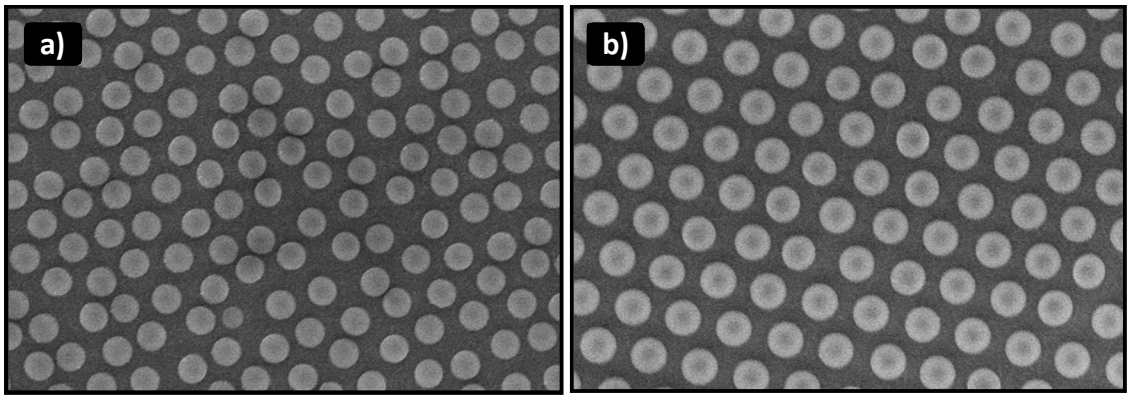

Fig. 3.8 *Scanning electron micrograph of a PS monolayer after RIE process a) without and b) with previously fixation of the latex spheres to the substrate.*

The prepared colloidal masks transferred to the solid substrates can act as a shadow mask for the material deposition process which is the basis of the NSL. Since the metal deposition process is very crucial for the structure development a brief introduction to the evaporation setup will be given.

3.3 Material deposition

All evaporation processes were done using a modified e-beam evaporator (BAK 640, Unaxis). Since the machine is a high-throughput system, it has an umbrella shaped holder for 24 5" wafers, as shown in figure 3.9a. Such a setup could not provide the necessary sample position control, therefore a separated holder is designed for shadow nanosphere lithography (SNSL) purposes [Fig 3.9b] which gives the necessary degrees of freedom to position the sample, of which the most crucial is the incident angle θ for the fabrication process.

The distance between sample and evaporation source was 50 cm. Therefore it was safe to consider the trajectories of atoms that hit the sample as parallel to each other. During all deposition processes the base pressure in the chamber was lower than 1.3×10^{-5} Pa, while the material deposition rate was kept constant at 0.5 Å/s. The thickness of the deposited material was controlled by a built-in quartz-crystal microbalance (QCM).

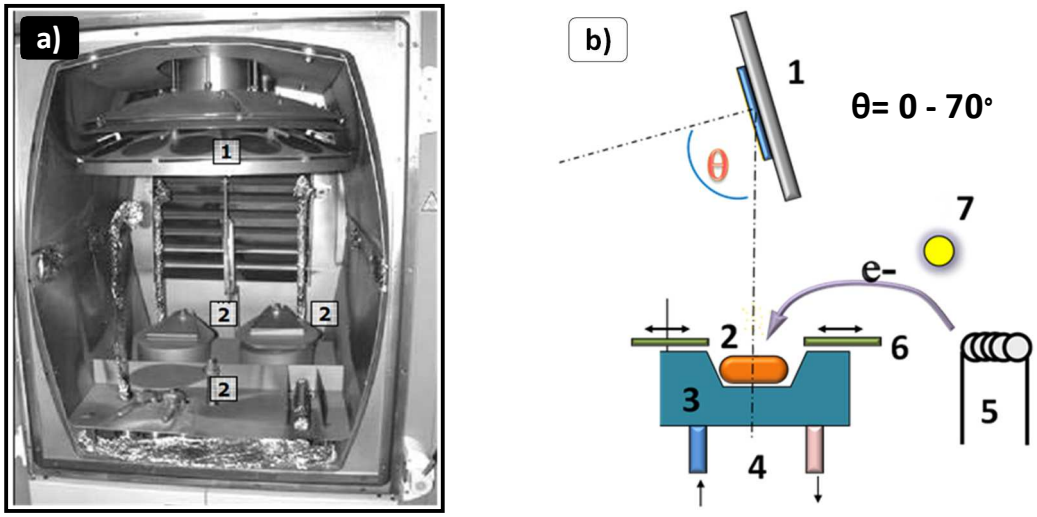

Fig. 3.9 *Evaporation setup for SNSL. a) Vacuum chamber of BAK 640: (1) rotation high-throughput holder, (2) evaporation sources, b) Schematic of evaporation system setup and orientation of a substrate during deposition process: (1) sample holder,(2) evaporation source, (3) crucible,(4) water cooling,(5) electron source,(6) shutter,(7) magnetic field.*

3.4 Mask lift off

After the material was transferred to the substrate, the PS mask could be removed in two ways depending on the thickness of the deposited film: 1) film thickness below 50 nm - adsorption of PS spheres to an adhesive tape (Tesa film), then peeling it from the substrate; 2) film thickness above 50nm - lift-off treatment is based on ultrasonication of the samples in tetrahydrofuran (THF) , 1-methyl 2-pyrrolidone (NMP), or toluene (in some cases acetone was a sufficient solvent). Depending on the film thickness and type of the structure ultrasonication took from 30 seconds up to 1 hour. The temperature of the dissolving medium was increased up to about 70°C to improve cleaning. After THF, NMP or toluene treatment, the sample was rinsed several times with 2-propanol or acetone, then in Mill-Q water, and dried in a stream of argon.

In the next sections, the results on the evaporation of the metals through ordinary and modified masks of the nanospheres will be presented. The requirements for the evaporation setup and influence of the mask on the final form of the structure will also be discussed.

3.5 Creation of triangular shaped metallic nanoislands

The simplest nanostructure that one can create with this lithographic method was an array of triangular shaped nanoislands. The production procedure consisted of use of a not modified colloidal crystal deposited on a substrate as a mask for a material deposition process. During material evaporation the sample was set normal to the evaporation directions, i.e., there was no tilt between material source and sample (θ = 0°).

The material evaporation and mask lift off process resulted in an array of triangular shaped particles. Atomic force microscopy was used to characterize the dimensions of the nanostructures. The AFM measurements were performed with Dimension 3100 with Nanoscope IV controller from Veeco. The samples were scanned in tapping mode using silicon tips, which had a nominal resonant frequency of 150 and 300 kHz respectively. Both kinds of AFM sensors had a tip radius of less than 10 nm according to the data provided by the manufacturer (Veeco Probes).

The exemplary results of the sample preparation are presented in Fig. 3.10. Here, a gallery of arrays of different sized triangles is depicted. The initial spheres used for fabrication of triangles were: a) 380 nm, b) 540 nm, c) 980 nm d) and e) 1710 nm in diameter.

It is clear that triangular particles follow the geometrical dependencies derived from the lithographic masks, thus their morphology can be easily deducted from the mask parameters. The sizes of these particles are proportionally to the diameter D_0 of the spheres used to build the mask. The height of the particle h, its separation S_d and surface $S_{\blacktriangle}$ is easily calculated from simple geometric considerations as shown in Fig. 3.11.

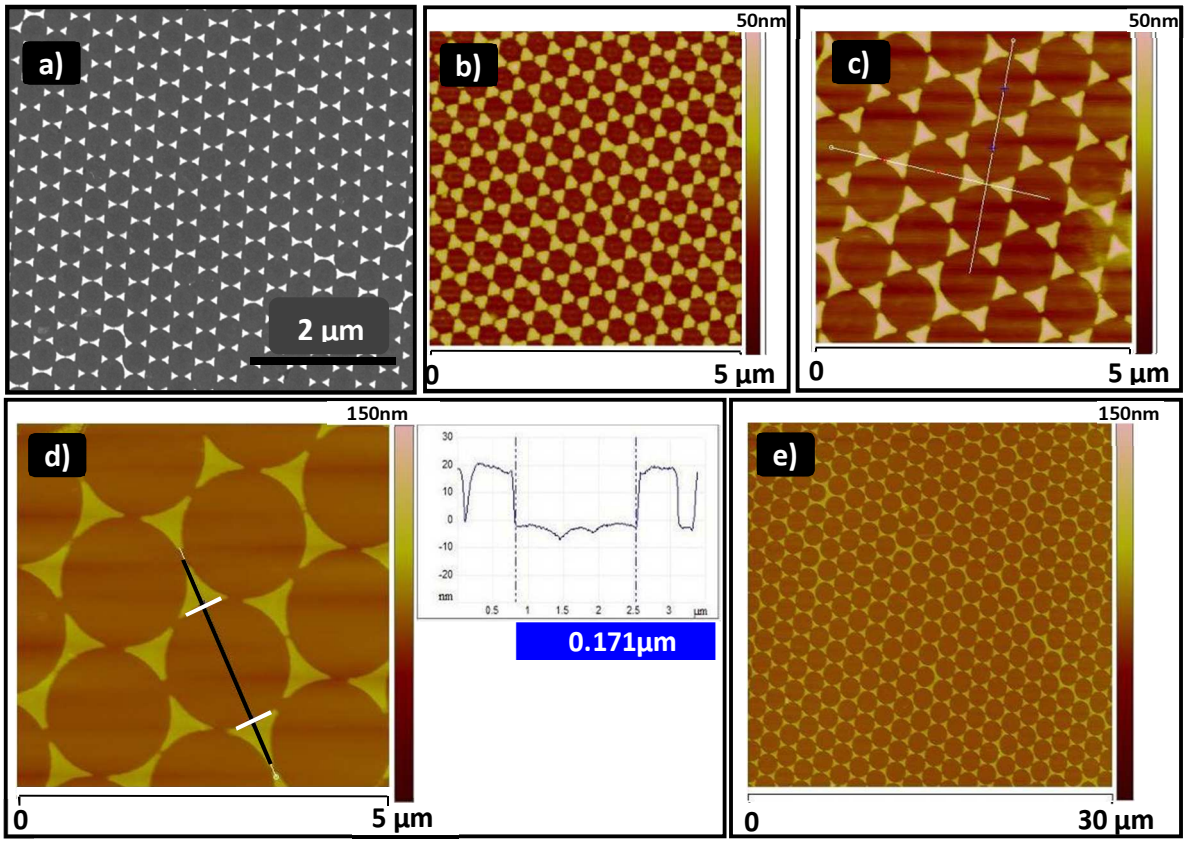

Fig. 3.10 *Nanotriangles arrays fabricated with different colloidal mask size: a) 380 nm, b) 540 nm, c) 980 nm, d) and e) 1710 nm, respectively.*

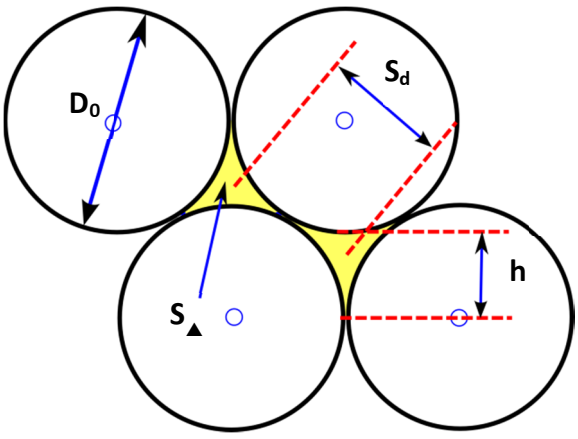

$$h = \frac{\sqrt{3}}{2} D_0 - \frac{1}{2} D_0 = D_0 \frac{(\sqrt{3}-1)}{2}$$

$$S_d = 2 * \frac{1}{3} * \frac{\sqrt{3}}{2} D_0 = D_0 \frac{\sqrt{3}}{3}$$

$$S_{\blacktriangle} = {D_0}^2 \frac{\sqrt{3}}{4} - 3 * \frac{1}{6} \pi \left(\frac{D_0}{2}\right)^2 =$$

$$= {D_0}^2 \frac{2\sqrt{3}}{8} - {D_0}^2 \frac{\pi}{8} = {D_0}^2 \frac{(2\sqrt{3}-\pi)}{8}$$

Fig. 3.11 *Some geometric dependencies of shape of particles obtainable by a perpendicular evaporation through the original masks.*

Since the preparation process requires only a deposition of the colloidal mask onto the substrate and subsequent evaporation of the metal, still one can encounter some defects in the final form of the structure. Here, the quality of the prepared mask and thus that of the used spheres have the most important influence on long periodicity and quality of the nanostructured arrays. Some of the typical defects which can be found in the samples are presented in Fig. 3.12. If the sphere size distribution reaches a coefficient of variation above 3% than one can expect a series of connected triangles, forming a line as depicted in Fig. 3.12a. This results from a smaller sphere which disturbs the desired hcp structure leaving a small gap between neighboring spheres. The second most common defect arises from an additional sphere appearing on the top of the monolayer. Such a sphere settles down directly in between the spheres and blocks an interstice from the deposition of material, which results in a missing particle in this place [Fig. 3.12b]. The last possible defect comes from insufficient close packing of the spheres, which produces pairs of triangles connected with their tips. The latter situation is presented in Fig. 3.12c. Still one has to remember about proper cleaning of the samples, because insufficient chemical or mechanical treatment may result in material residuals [Fig. 3.12d].

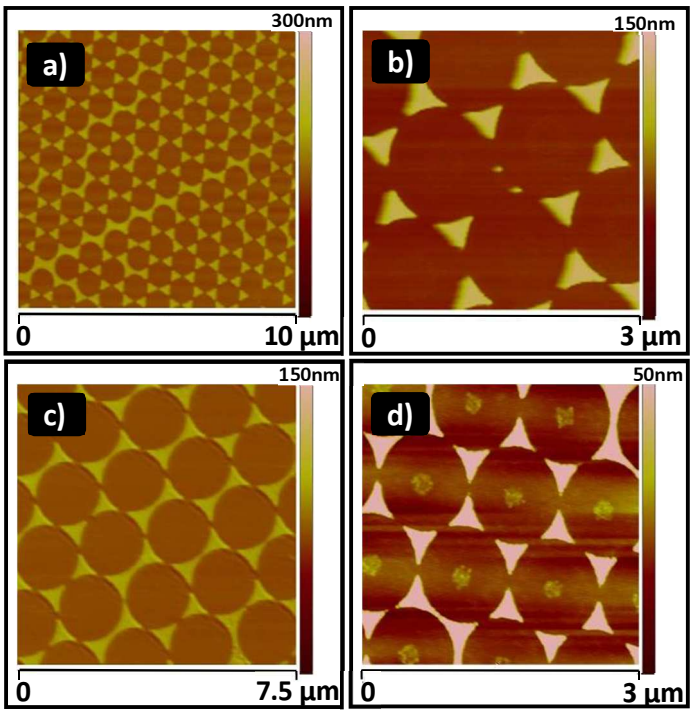

Fig. 3.12 *Possible defects in arrays of triangular particles: a) series of connected triangles – smaller sphere, b) missing triangles – multilayer colloidal mask, c) pairs or groups of connected triangles – insufficient close packing of monolayer, d) spheres residuals – inadequate sample cleaning.*

The perpendicular deposition of the material through a RIE modified mask may result in formation of structures with different morphologies. In the following section the preparation and structural characterization of nanohole arrays will be presented.

3.6 Creation of holes

As described in chapter 3.1.1 the etching process is increasing the area of the void spaces between the polystyrene spheres and causes the contact areas between them to split open and can be used for production of arrays of subwavelength holes in metallic films. In short, as in the case of triangular shaped structures a formed from PS-spheres with diameter of 440 nm monolayer was deposited on sapphire chips. As we know, this close-packed structure prohibits the growth of an array of particles. Thus the diameter of the PS-spheres had been reduced by means of reactive ion etching. Samples were modified in a RIE chamber using following constant parameters: Ar=10 sccm, O_2=35 sccm, P=60 W, p=8 Pa, while the process duration was varied between 20 and 50 s. Afterwards, the obtained structure was used as a mask in the metal evaporation process. The deposition of 50 nm of material (e.g., Aluminum) onto the samples took place under the same conditions as in case of formation of the nanotriangles: the evaporation angle was kept at θ = 0°. Finally, all samples were cleaned with standard mask lift-off procedure (see section 3.4).
The samples were routinely characterized under a scanning electron microscope, which confirmed the formation of a large area of defect-free arrays of subwavelength holes [Fig. 3.13a] with a high quality long range order [Fig. 3.13b].

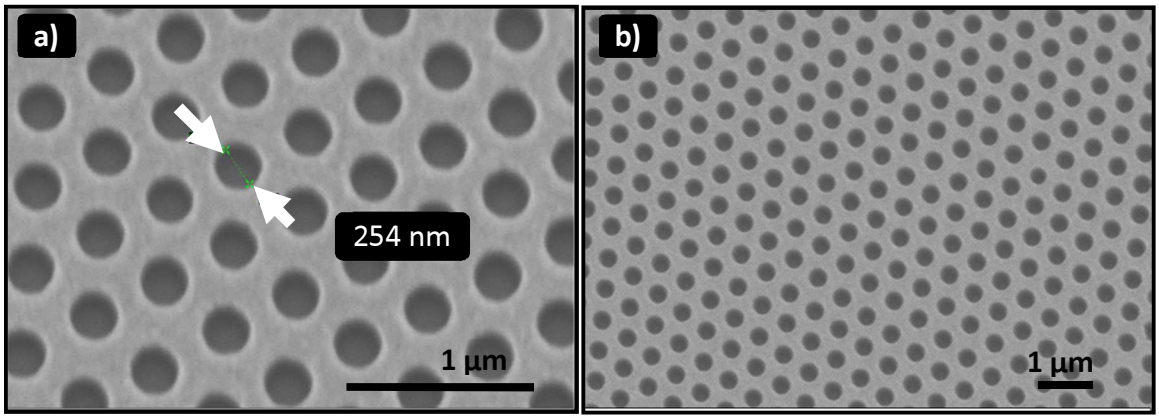

Fig. 3.13 *SEM image of a 50 nm thick Al film with subwavelength holes: a) the measured hole diameter was approximately 254 nm, b) the defect free area ranges hundreds of µm^2.*

Secondly the investigations of series of samples revealed that applying different etching times resulted in decreasing hole diameters in structures. The consequence of the RIE process duration set to 20, 30, 40, and 50 s and evaporation of 50 nm of Al were holes with diameters of 385, 340, 325, and 254 nm, respectively, as is shown in Fig 3.14.

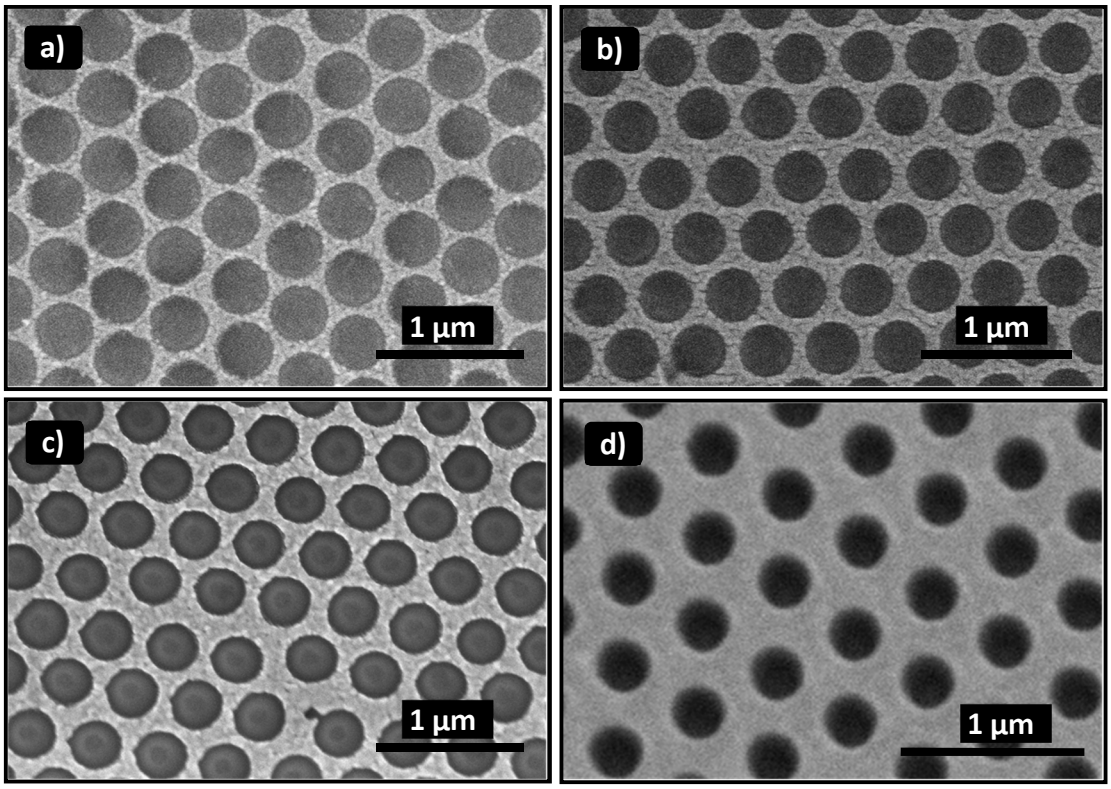

Fig. 3.14 *SEM images of nanoholes arrays. The diameter of a single hole is a) 385 nm, b) 340 nm, c) 325 nm and d) 254 nm.*

More detailed studies of the structural properties of the samples were performed using an atomic force microscope. The AFM investigation of the sample prepared with RIE time of 50 s revealed that single hole diameter was 250 nm [Fig. 3.15], which confirmed the adequately chosen etching parameters. The cross-section of a structured film presented on the right panel of a Fig. 3.15 shows that the evaporation process resulted in the desired film thickness of 50 nm. The local roughness of below 5 nm is an evidence of a smooth film surface. Additionally, the measurements reveal that the holes are free of any polymer residues [Fig. 3.14 and Fig. 3.15], which highly depends on the solvent used for the cleaning process and the duration of the ultrasonication. Figure 3.16 shows a comparison of the cross section of the hole arrays cleaned in THF ultrasonication bath for 3 min [Fig. 3.16a] and another sample cleaned

in Toluene in an ultrasonic bath for 30 min. The latter treatment removes completely the PS residues as presented in Figure 3.16b.

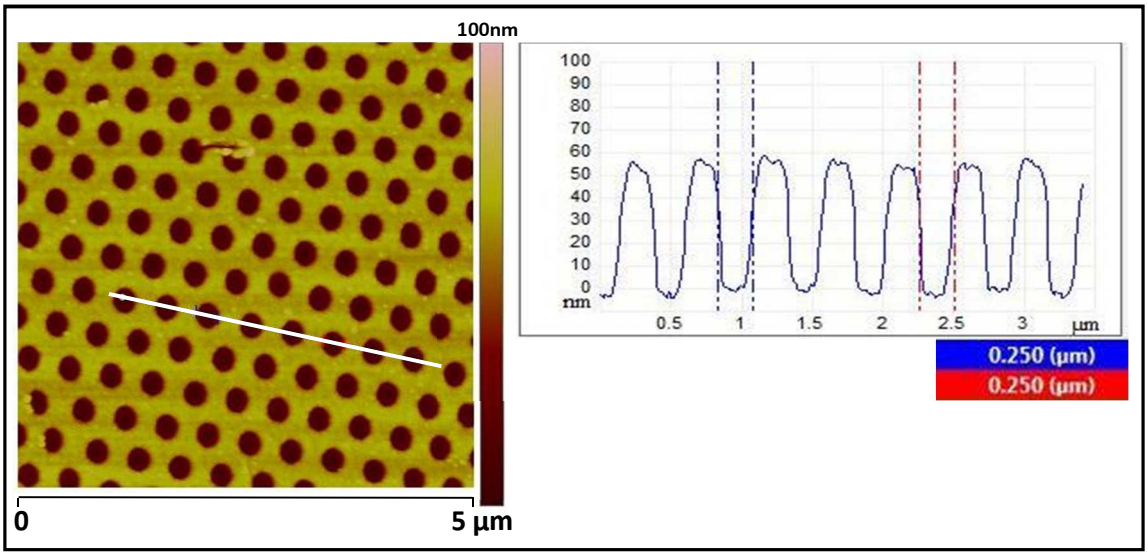

Fig. 3.15 *AFM image of an array of holes in a 50 nm thick Au film. Left side: topography image. Right side: cross-section image confirming that the observed hole diameter is 250 nm, while the hole periodicity is 470 nm. The measured film thickness is approx. 50 nm plus 2nm of a Ti buffer layer.*

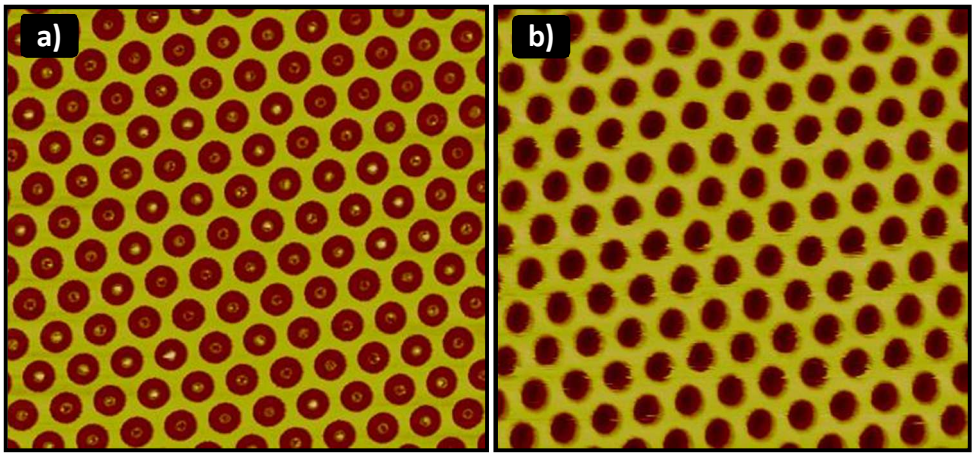

Fig. 3.16 *AFM topography images of an array of holes in a 50 nm thick Au film showing the importance of proper sample cleaning process a) sample sonicated for 3 min in THF - PS-residuals left, b) sample sonicated for 30 min in Toluene.*

The results show that the choice of the proper etching time lead to a desired hole size in a mesh of metal film. The hole diameter is not the only parameter that we are able to control, the initial size of the spheres used for mask preparation has influence on the interhole distance. Therefore, etching the colloidal monolayers prepared with

spheres of various sizes can be used to change the geometry of the final form of the nanostructure. The gallery of AFM images [Fig. 3.17] shows different hole arrays, which were prepared by RIE on masks. The initial sphere diameter was: a) 440, b) 540, c) 980, and d) 1200 nm. The mesh size was 255, 320, 700, and 720 nm, respectively.

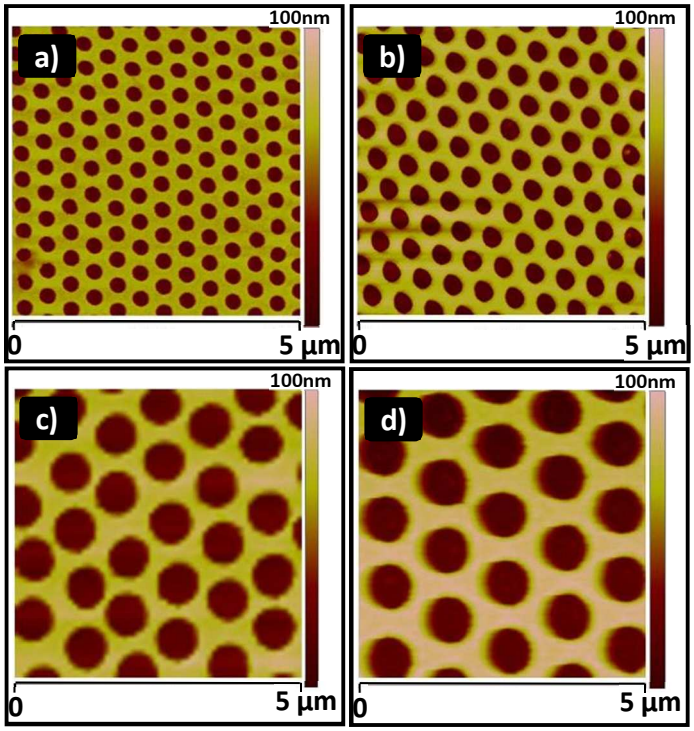

Fig. 3.17 *Series of nanohole arrays with initial sphere/hole size of: a) 440 nm / 255 nm, b) 540 nm / 320 nm, c) 980 nm / 700 nm and d) 1200 nm / 720 nm.*

The etching process, change of evaporation angle and the orientation of the crystalline of the mask can lead to the formation of wire-like structures. The details on the preparation of such structures will be presented in the next section.

3.7 Creation of wires

To fabricate nanowires by means of NSL, one has to know the orientation of the mask (before or after etching) on the substrate prior to the material evaporation, since the orientation of the mask is not controlled during the monolayer preparation. The orientation of the PS - mask can usually be checked afterwards by laser diffraction, as the particles remain in high quality long-range order. It is therefore possible to observe diffraction patterns and thus gain the necessary information about orientation and spacing within. Such a diffraction pattern for 440 nm particles is presented in Fig. 3.18a. To obtain such a pattern the laser wavelength has to be adjusted to the particle

size. For very small particles a UV laser is necessary or scanning electron microscopy (SEM) imaging can be used to determine the orientation of the high symmetry directions of the lattice/crystal.

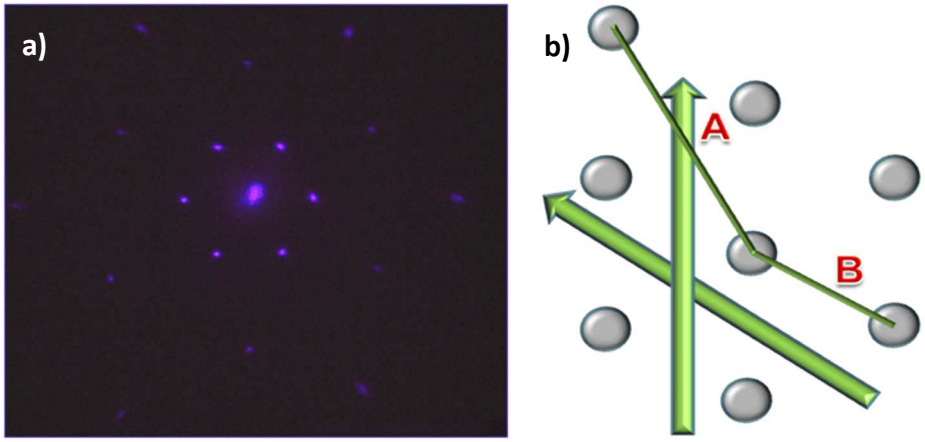

Fig. 3.18 *Determination of mask orientation: a) Macroscopic laser diffraction pattern used for measuring the orientation of latex nanosphere mask, b) real space image of the position of the spheres and possible evaporation directions (green arrows), A and B denote the two high-symmetry directions of the structure, respectively.*

The key aspect for the fabrication of nanowires is thus the orientation of the sample during the evaporation. To ensure a proper generation of nanowires the sample normal must be tilted by a minimum of θ = 60°. Additionally, the projection of the tilting axis to the sample's surface must be perpendicular to one of the high symmetry axes of the mask crystal. Previously, triangular shaped nanoparticles or the hexagonal lattice of holes were generated when the sample's normal is parallel to the evaporation beam (θ = 0°).

Following the mask creation procedure we have prepared at first a monolayer of 440 nm latex spheres, which was deposited on sapphire substrates. After the drying process the samples were modified in a RIE chamber using following constant parameters: Ar=10 sccm, O_2=35 sccm, P=60 W, p=8 Pa. Process duration was varying between 45 and 55 s. In the next step samples were installed in the EBE system and 100 nm of Gold and Fe preceded with a buffer layer of 2 nm of Titanium (thin Ti film acts as an adhesive layer for the desired materials [78]) was deposited under an angle of θ = 70°. Finally, all samples were cleaned as before and dried under an Ar stream. Afterwards, we characterized the samples by means of SEM and AFM. As is shown on the scanning electron microscope micrographs [Fig. 3.19a] a highly oriented and long range nanowire array is obtained. The defect free array covers an area up to hundreds

of square micrometers [Fig. 3.19b]. The two lower panels show atomic force micrographs of the structural properties of the obtained wires [Fig. 3.19c and d].

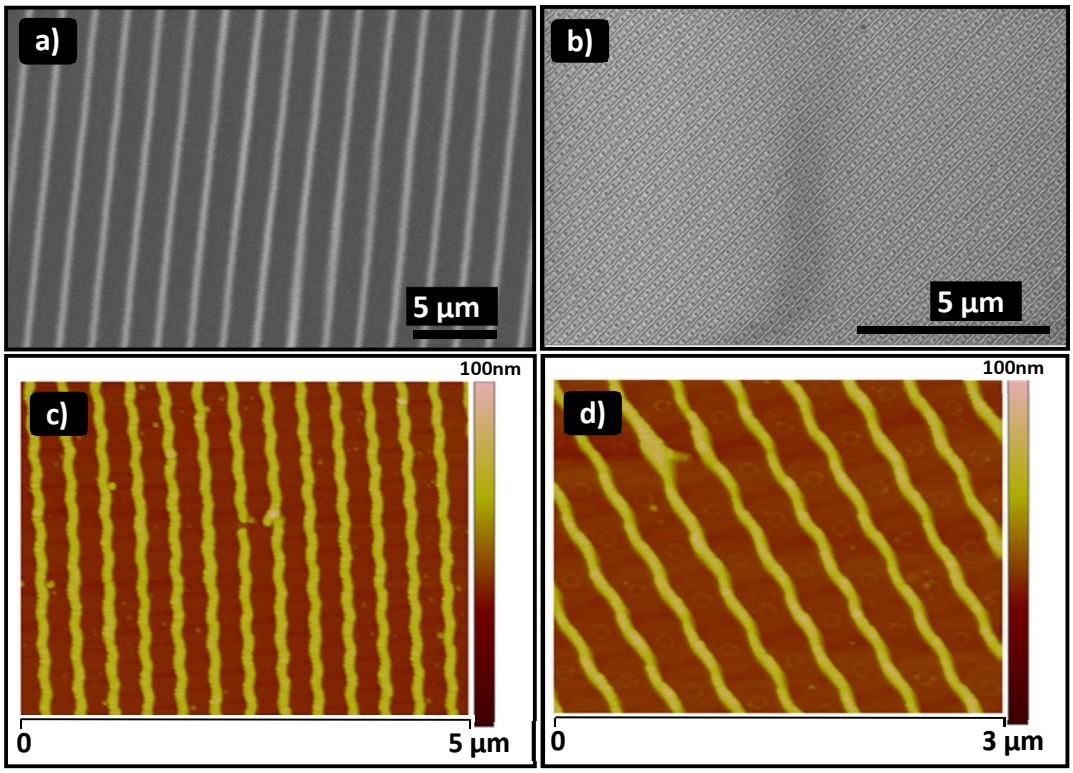

Fig. 3.19 *Experimental results of the obtained nanowire array: a) and b) SEM images, c) and d) atomic force microscopy imaging.*

It is clear that the spheres' shape has a strong influence on the final form of the nanowires leaving periodic half spherical curvature. This leads to a more complex structure than a one dimensional grating made of straight wires with cubic or rectangular cross-sections. Gratings having wires with a rectangular cross section are sometimes denoted as slit gratings.

An additional profile measurement was performed perpendicular to the direction of the wires [Fig. 3.20]. In this case, the spectral period of 386 nm was estimated. This value corresponds well to the used nanosphere diameter. AFM measurements pointed to a wire thickness of ca. 35 nm. In this case a gap size between two wires modulates among 210 nm and 255 nm when to half spherical curvatures are convex and concave to each other, respectively. The change of gap size is present in the horizontal as well as the vertical direction referring to the position of the wires.

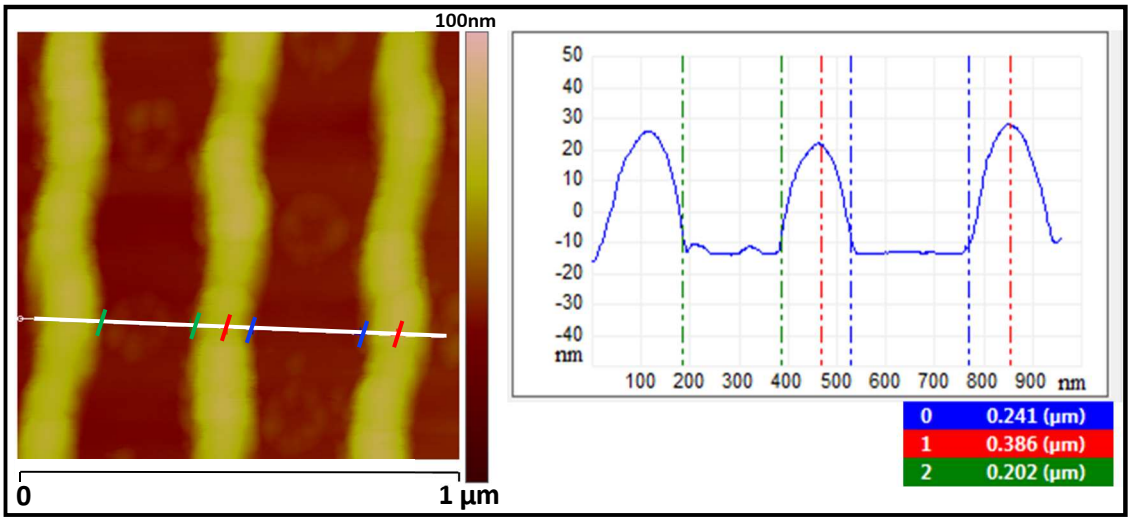

Fig. 3.20 *Structural properties of Au nanowires. Line width is 140 nm, thickness is 35 nm and distance between neighboring lines is 240 nm. The sphere size used for preparation is 440 nm in diameter.*

The geometric parameters can be controlled by the etching process (wires width and gap size) or by use of different size of spheres (periodicity). In Fig. 3.21 AFM images of nanowire arrays are presented. Their periodicity was changed by use of spheres which initial diameters of: 440, 540, and 1200 nm.

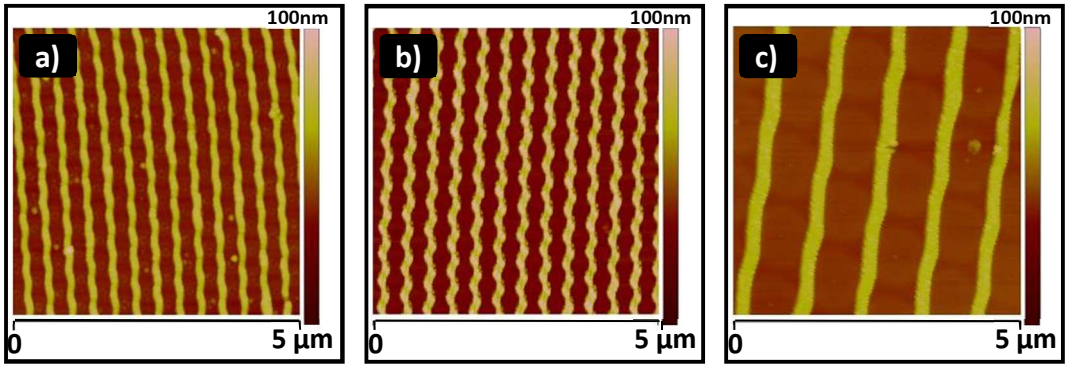

Fig. 3.21 *Change of structural properties of the nanowire array by choice of spheres of initial diameter: a) 440 nm, b) 540 nm, and c) 1200 nm.*

Such a multistep preparation process requires high precision in every step. Small mistakes can lead to unplanned defects in the final form of the structure. Beginning from the mask preparation one has to avoid drowning of the spheres because this will lead to defects like single spheres on top of the multilayer but even more to multilayer crystals. So during the RIE process it is crucial to control the parameter space because this directly affects the structural properties and thus the quality of the layers. For example, if the etching time is too long, an inhomogeneous shape of the etched spheres might be the result, which directly leads to a varying width and nonlinear wires [Fig. 3.22b]. Finally, finding the correct evaporation direction with respect to the crystal orientation and deposition of material along the principle direction (for details see page 37) and angle leave other possibilities for mistakes. Figure 3.22c presents results of incorrect orientation of PS-masks on substrates resulting in very short and mostly inhomogeneous wires.

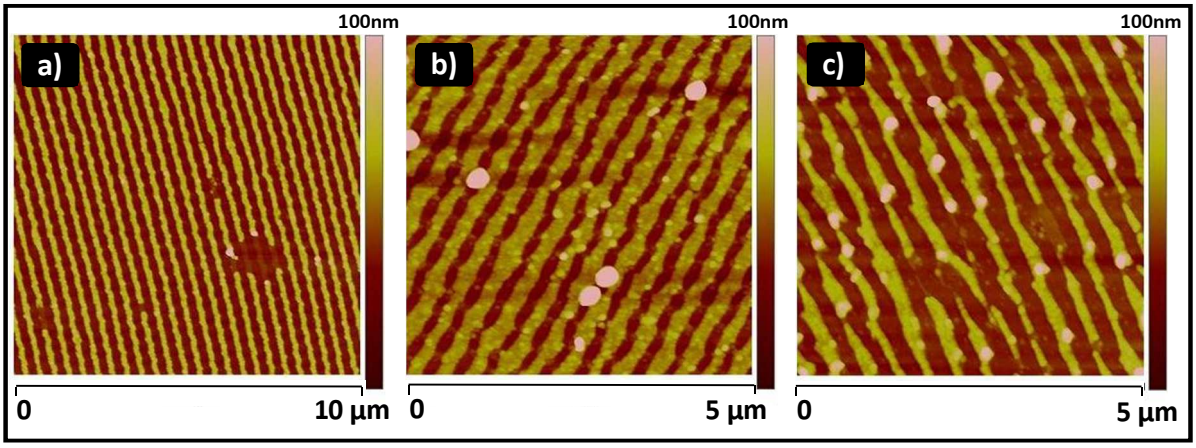

Fig. 3.22 *Defects in nanowire arrays caused by: a) extra spheres, b)bad etching c) wrong crystal orientation for evaporation.*

4. Sample characterization – optical properties

In this section we will focus on the plasmonic properties of the nanostructures of various morphology. The investigations require a selection of appropriate materials utilized for samples' preparation. Certainly gold is a right choice, since its optical response is well known. These optical properties as well as the influence of various structures on the plasmonic characteristics lead to different experimental possibilities in which gold is a leading medium; nevertheless for some structures other materials for comparison were used.

4.1 Experimental setup

Investigations of the optical properties were carried out with an UV-Vis-NIR spectrometer (Varian, Carry 5000) between 200 and 3000 nm. The spectrometer is equipped with two home build sample holders, which enabled to change the incidence angle θ_{inc} [Fig. 4.1a], as well as the sample rotation angle φ [Fig. 4.1b]. The sample can thus be rotated around the surface normal to change the angle between the light polarization and the nanostructure.

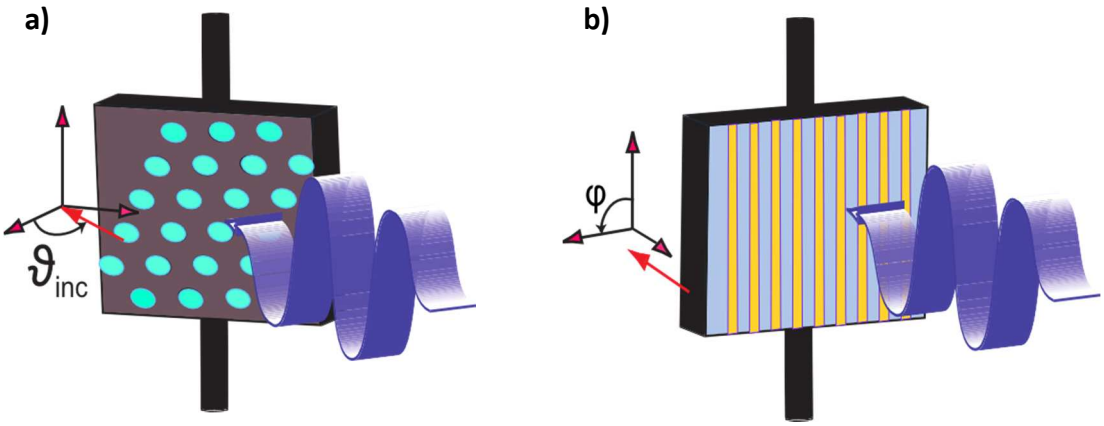

Fig. 4.1 *Home build sample holders used for far field measurements that enabled the change of two angles: a)* incidence angle θ_{inc}*,- for measurements of nanohole arrays b) rotation angle* φ *– for measurements of nanowire arrays.*

In addition near-field optical investigations were performed using a combined AFM/scanning near-field optical microscope (SNOM; Mutliview 1000, Nanonics Imaging Ltd). A schematic of the SNOM setup is shown on Fig. 4.2. A He-Cd laser set for operation at wavelength of 442 nm is used as an illumination source. In this setup light passes through a half-wave plate and a polarizer, this enabled a control of the intensity and the polarization. Afterwards the light is coupled into a multimode fiber with a tapered Al-coated tip, the aperture diameter of a fiber tip is between 50 and 100 nm. This offers the opportunity of local illumination of the sample. While working in transmission mode, the light is collected behind the sample through a microscope, and after passing a filter, it is directed to an avalanche photo diode.

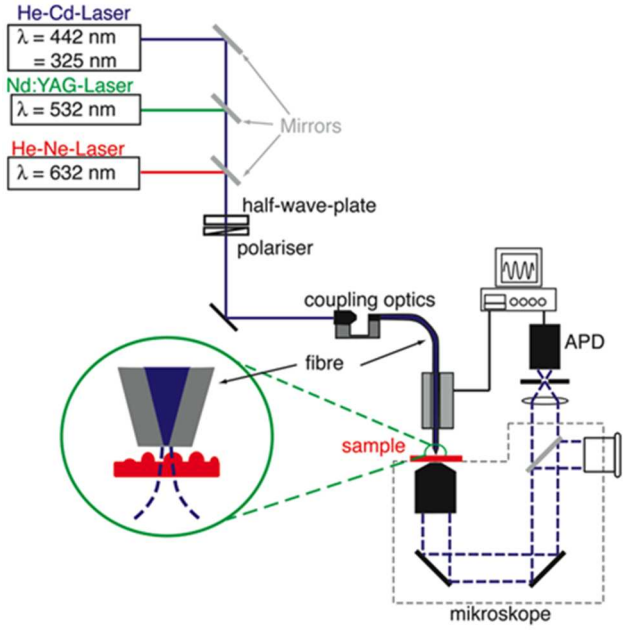

Fig. 4.2 *Schematic of the experimental setup for the illumination-mode SNOM measurements in transmission.*

4.2 Plasmonic properties of an array of triangular shaped gold nanoislands

In general nanoparticles with nonplatonic shapes (tubes, flakes, rods, prisms etc.) fabricated from different materials and by various techniques have recently attracted a lot of attention [79-87] mostly because of their interesting optical properties and the large variety of possible applications, i.e., for biosensing [88, 89], catalysis [90], or data storage [91]. As presented in section 2.1 materials that exhibit a large negative real and small positive imaginary dielectric function are capable of supporting a collective excitation of the conduction electrons known as plasmon excitation. In metal nanoparticles this leads to a localized surface plasmon resonance (LSPR) [25, 30, 51]. Recent works demonstrated that the position of the LSPR extinction maximum, λ_{max}, is sensitive to the size, shape, interparticle spacing, dielectric environment, and dielectric properties of the nanoparticles [92-96]. As a result, metallic nanoparticles that support LSPR are promising platforms as highly sensitive optical nanosensors, as photonic components, and in surface-enhanced spectroscopies [92, 97-100]. It is well established that Ag and Au nanoparticles support localized surface plasmon resonances that can be widely tuned from UV to near-IR regions of the electromagnetic spectrum [101, 102]. In this section the plasmonic properties of triangular shaped nanoparticles of different size established in a hexagonal array will be investigated.

To obtain a different size of triangular nanoparticles PMMA (poly-methylmethacrylate) and polystyrene nanospheres with diameters of, 380 (PMMA), 540, 980, and 1710 nm, were used. After transferring the mask to sapphire substrates a deposition of 2 nm Ti (adhesion layer) followed by 20 nm thick Au films was carried out in an e-beam evaporation-system with a base pressure of 10^{-7}mbar. After the cleaning procedure the samples were characterized for structural and optical properties.

The UV-Vis-NIR spectroscopy technique was chosen to examine the samples optically - especially for the existence of the surface plasmon resonances. Different from transmission measurements on other structures presented in the following sections, here the optical absorption data for the arrays of triangular particles were investigated, while absorbance is defined as:

$$A_\lambda = log(I_0 / I) \qquad \text{(Eq. 4.1)}$$

where I is transmitted light intensity and I_0 is the incident light intensity.

The experiments were carried out in the wavelength range between 200 – 3000 nm under normal incidence of light (no rotation or tilting was employed).The experimental spectra for 20 nm thick Au triangles on sapphire substrates deposited through masks with sphere diameters D_0 = 380, 540, 980 and 1710 nm are shown in Fig. 4.3 (the data were reproduced after [77]). The AFM images on the top of the chart represent the fabricated structure for each D_0. The aspect ratio between figures is kept, and reflects the difference in structures size. Each spectrum is strongly dominated by a pronounced resonance peak at a wavelength of 704 nm, 996 nm, 1417 nm and 2417 nm respectively (denoted in Fig. 4.3 for each series with a colored arrow with index 1). The position of each absorption feature strongly depends on D_0. It is expected, that these resonances are from a highly dispersive, plasmon – polaritonic mode, since similar resonances have been observed in metallic clusters [103, 104]. As it was shown by Peng et al. [105], one has to assume that these resonances (as well as higher order resonances marked on the chart with an arrow and index corresponding to the order of the resonance) can be viewed as circumferentially quantized surface plasmon waves. We ignore for the moment particle-particle interactions. Since each side of the quasitriangular particle equals approximately 1/6 of the sphere circumference πD_0, the circumference of the particle is $\pi D_0/2$, and thus the circumferential quantization condition requires that this circumference is equal an integer multiple of the wavelengths of the resonating surface/edge plasmon wave (λ_{SP}):

$$l\lambda_{SP} \approx \frac{\pi D_0}{2} \qquad \text{(Eq. 4.2)}$$

where l = 1, 2 ,3 ,4 is the integer for first (main peak), second, third and forth order of resonance respectively.

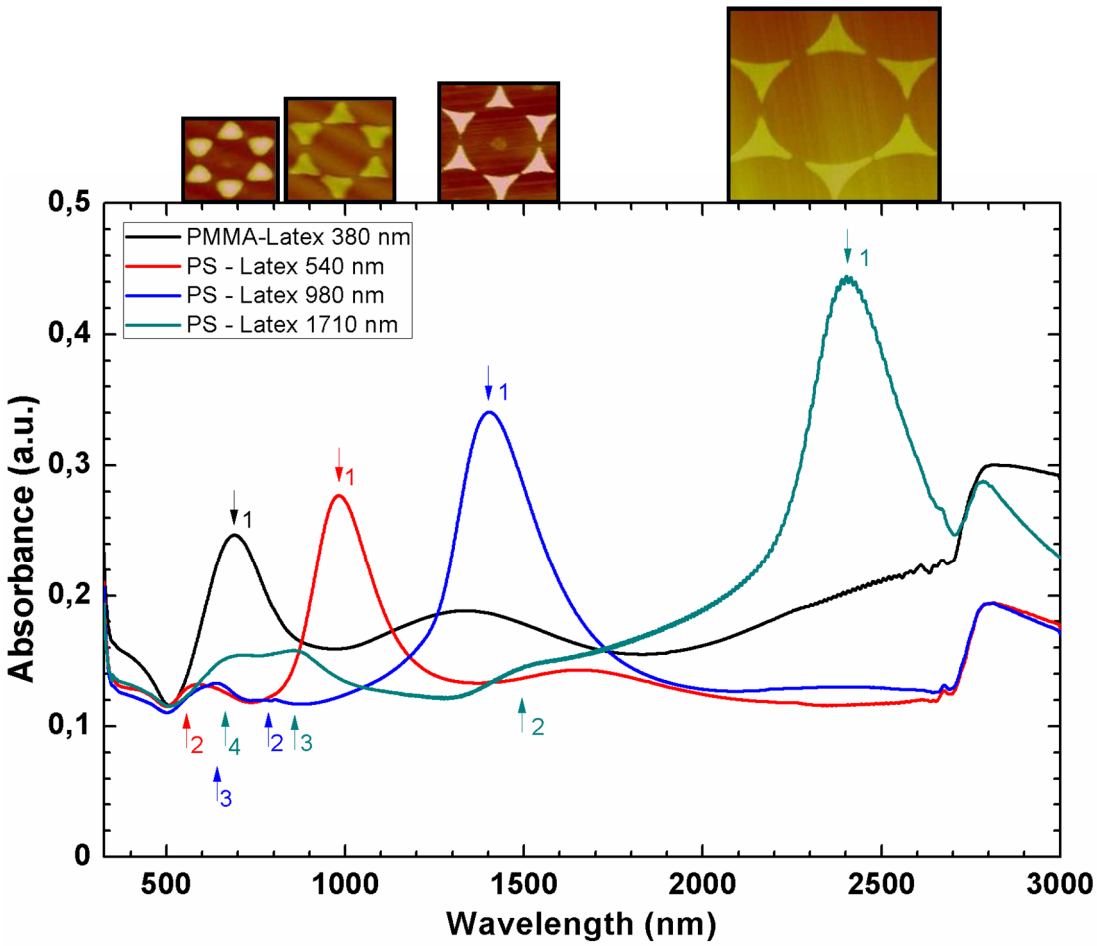

Fig. 4.3 *Measured optical absorbance (in arbitrary units) for the quasitriangle arrays with various* D_0. *The AFM images on the top of the chart represent fabricated structure for each* D_0. *Spectra of the light exhibit first (most pronounced), second, third and forth absorbance peaks for variously sized Au quasitriangular particles which were made of different sphere diameter for NSL as presented in a legend of the chart. Arrows with respective index mark absorbance peaks* (λ_{max}) *for adequate plasmon resonance order of the triangular particles. The wavelength at the maximum on each curve increases with the sphere diameter* D_0 *= 380, 540, 980, and 1710 nm.*

The other possible interpretation of the peaks at the positions marked as 2nd, 3rd and 4th order for the triangles fabricated with 540, 980, and 1710 nm respectively is that they belong to the transversal plasmon resonance, which occurs in a thickness of the structure. For the triangles made using of 380 nm spheres this peak is not visible, this could be due to the fact that the main absorbance peak is very pronounced and close enough to overlap small transversal resonance.

In Table 1 the measured (λ_{max}) and calculated λ_{SP} peak positions for different orders (l) and size of spheres used to fabricate arrays of gold nanoislands are gathered. The

values for λ_{SP}, were obtained by using Eq. 4.2 and the values for λ_{max} were taken from Fig. 4.3, where wavelengths were read for each arrow-mark (wavelength at a peak) for adequate D_0.

Table 1 *Calculated and measured resonance peak positions.*

	D_0 [nm]							
	380		540		980		1710	
l	λ_{max}	λ_{SP}	λ_{max}	λ_{SP}	λ_{max}	λ_{SP}	λ_{max}	λ_{SP}
1	704	597	996	848	1417	1539	2417	2686
2	-	298	596	424	799	769	1551	1343
3	-	198	-	282	658	513	875	895
4	-	149	-	212	-	385	709	671

Figure 4.4 shows the resonating mode dispersion plotted as $\omega n/2\pi c=1/\lambda_{max}$ versus $k/2\pi=1/\lambda_{SP}$. and l. n represents the effective refractive index of the medium which surrounds the nanoparticles (of order 1 in this case). Depending on D_0 more or less of higher order peaks are visible, i.e., for $D_0 = 1710$ nm four and for $D_0 = 380$ nm only one order is visible. In Fig. 3.26 the black squares are indexed with numbers indicating the resonance order (for l = 1, 2, 3, 4). All of the points congregate around a single line (magenta line in Fig. 4.4), which is drawn here just as a guide to the eye. This confirms that all of the resonances (measured and calculated) belong to a single mode. The solid blue line represents the corresponding light line (photon dispersion): $\omega=kc/n$ or simply $1/\lambda_{max}=1/\lambda_{SP}$.

For comparison with the experiment, Peng et al [105] performed simulations, based on the finite difference time domain (FDTD) computation scheme, and the results are presented in Fig 4.4. Here the white squares represent the simulated dispersion for arrays of triangular-shaped particles. Additionally, a simulated optical absorbance for quasitriangular arrays is depicted as the inset. The D_0 chosen for the simulations reflects the sphere diameter used for the experiment.

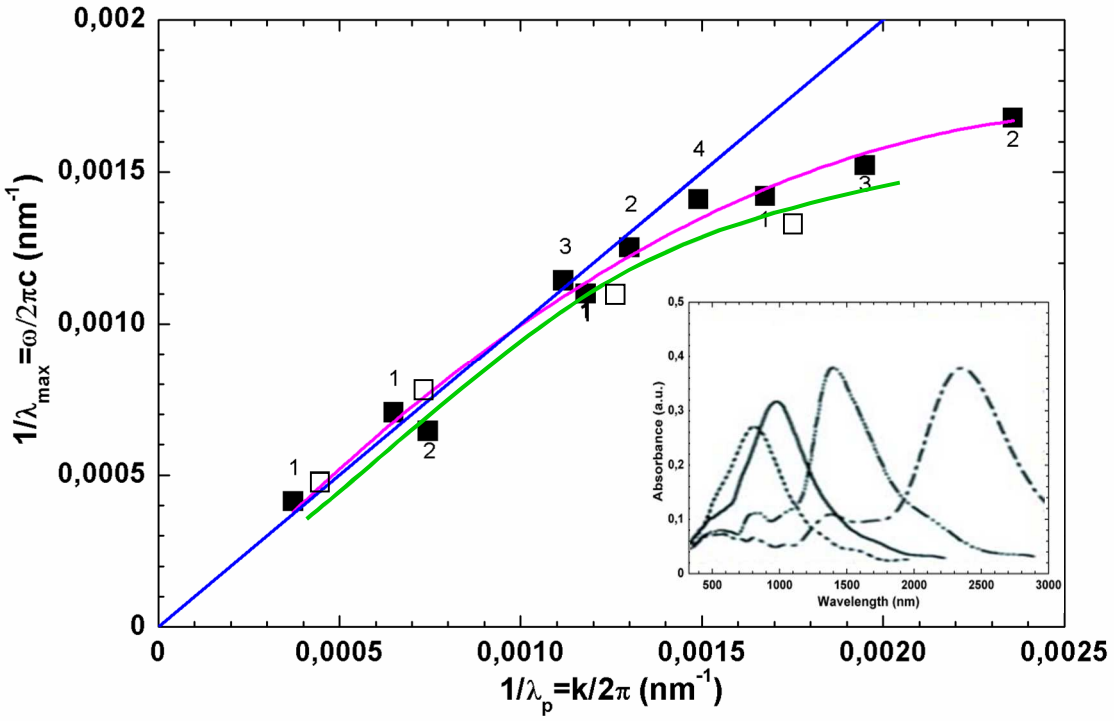

Fig. 4.4 *Measured and simulated dispersion of the resonating surface/edge plasmon in an array of quasitriangle nanoparticles: measured for all orders, where the numbers by the black squares indicate the corresponding order (for l = 1, 2, 3, 4) respectively. The solid blue line is the light line. The solid magenta line is a fit to the measured data. Simulated dispersion for arrays of triangles is depicted with white squares. The solid green line is a fit to the simulated data. The inset shows the simulated optical absorbance (in arbitrary units) for the quasitriangle arrays with various D_0, to be compared to the corresponding experimental data in Fig. 4.3.*

Clearly, all resonances belong to the single mode. The surface/edge plasmon mode in this quasitriangular nanoparticle lattice follows the photon line for wavevectors k<0.007 nm^{-1}. This is the retarded, or polaritonic regime, in which the mode is a photon-plasmon hybrid (plasmon polariton) [106]. For large wavevectors k>0.007 nm^{-1} (nonretarded regime), the dispersion curve deviates from the light line. This is due to presence of the Mie resonance in a center of mass [105 and references therein], which is the collective motion of the oscillating electron gas in a potential of the positive background. The above mentioned experimental results stay in a very good agreement with theoretical calculations as presented in Fig. 4.4. The fit to the simulated dispersion of the arrays of triangles is nearly identical with the guideline of the measured dispersion [106]. The above discussions regarding plasmonic features include only features which appear in Fig. 4.3 for wavelengths equal to and shorter

than the main absorbance peak position (different orders of surface/edge plasmon mode). Besides that, there is also an additional feature that can be seen. It is a red-shift and broadening of the resonance according to the 1st order surface/edge plasmon. This peak is noticeable for arrays of triangular particles fabricated with spheres of D_0 =380, 540 and 980 nm, at 1345 nm, 1675 nm, and 2414 nm, respectively. For the spheres of D_0 =1710 nm this peak is not present because it is a secondary maximum being beyond detector range. These features are most likely an outcome of connected triangles like those presented in Fig. 3.12a and c, which form a bigger surface (volume) in which surface plasmons can oscillate. As previously mentioned such imperfections can be produced due to mask imperfections or dislocations.
Following measurements of the triangular shaped nanoislands a characterization of the perforated films has been carried out.

4.3 Plasmonic properties of array of holes: Gold and Aluminum

The transmission properties of a subwavelength hole in a metal film have been studied since decades. But, the most intensive investigations have been carried out after Ebbesen and co-workers experimentally showed that the extension of a single hole to an array of subwavelength apertures leads to an enhanced transmission of light (as mentioned in section 2.3.3). Since first predictions for a single aperture published by Bethe in 1944 [64], many attempts to understand the transmission properties, which are fundamental in near-field optical microscopy were done. In addition a huge amount of theoretical [107-109] and experimental [110-113] studies have been carried out to understand the underlying physics. However, the results of the transmission measurements on these subwavelength hole arrays draw the attention to nanostructure films. There was a need to find the origins of the processes responsible for the reported enhanced transmission. There is still a lot of discussion and disagreement on the origin of the underlying physics describing the extraordinary transmission. The two approaches are: the model of coupling of light to surface plasmons [17, 62, 114] and the model of evanescent waves [115]. Finally, it was clarified [116] with advantage to the model of coupling to SP, which is connected to the geometrical parameters of the array of holes. Thus the change of parameters like hole depth and period has an influence to the plasmonic response. Still the recent works report only on results of optical properties of arrays with square symmetry of holes in films.
Therefore, in the following sections the experimental results on hexagonal arrays of holes in a gold and aluminum film will be presented. The characterization was carried

out on hole arrays in gold and aluminum films of thickness 20, 50 and, 120 nm. For the Au films a buffer layer of 2nm Ti was used, as in the case of nanotriangles. The measured hole diameter D_H is 250 nm and the interhole distance is kept constant at 470 nm.

4.3.1 Far field results

The far-field optical characterization results measured in the range between 200 and 2500 nm are shown in Fig. 4.5. The measurements show transmission spectra of samples taken under normal incidence, for a gold (panel a) and an aluminum (panel b) nanostructured film. Additionally, the spectra of 20 nm thick film (blue lines) are included for comparison. As expected, the solid and structured gold films show as spectral feature a pronounced peak at 2.5 eV (~500 nm) which origin is quite complex. Gold material as well as copper exhibit considerable overlapping of bulk plasmon resonance edge and interband transition in the visible range. [117]. Here one can observe the rising edge from 2.3 eV (540 nm) towards shorter wavelengths which is due to the bulk plasmon edge following with interband transition trough at around 2.5 eV, where d-electrons are promoted to the s-p conduction band [118]. The peak broadens slightly with decreasing the film thickness. Such effect is very pronounced in case of small nanoparticles, when the particle's radius is reduced, the conduction electrons (which are almost free) experience collisions not only with positive background but also with the surface. Thus, the electrons mean free path in Eq. 2.12 from section 2.2.4 is decreased causing the escalation of the damping factor γ which explains the broadening of the surface plasma resonance peak. Some additional features are visible in the spectra of gold hole arrays at 820 nm, 870 nm, and 1000 nm for all film thicknesses. These peaks tend to red shift and broaden with decreasing film thickness. The width of the peaks appears to be strongly dependent on the aspect ratio, i.e., the film thickness divided by the diameter of the cylindrical holes (t/D_H). For a film thickness to hole diameter ratio close to 0.1, the peaks are very broad and just discernible and when the ratio reaches ~0.5, the maximum sharpness is obtained. Further narrowing might depend on the quality of the individual holes [17]. In the study done by Ebbesen, he also claims that an array of such holes can present spectra with highly zero-order transmission (where the incident and detected light are collinear) at wavelengths which are longer than the period of the array (470 nm), beyond which no diffraction can occur. In our case the additional interesting features are the two pronounced peaks above 1000 nm which in fact is much longer than the hole diameter: the first one is centered around 1200 nm and the second one around 2100 nm, respectively. One can observe that while the film thickness is decreasing, the

peak intensity increases for the peak at 1100 nm and decreases for the peak at 2100 nm. Finally, for the 20 nm gold film only the first, strongly pronounced peak at 1000 nm remains. This behavior points towards a change in the oscillator strength.
Other additional features for array of holes can be connected to surface plasmons (SP) at maxima and following close to them Wood anomalies at minima positions [62, 113, 119]. To prove this statement, we have calculated with Eq. 2.21 wavelengths at which the surface plasmons are expected for both interfaces and are depicted with blue and black dashed lines in Fig. 4.5a. The peak positions for the metal – air interface are labeled as SP_A, the label SP_S is related to the peak positions for the metal-substrate interface. The numerical data is gathered in the Table 2. Additionally, for both dielectric materials boundaring with the hole arrays the positions of Wood's anomaly are calculated with Eq. 2.23 and depicted on the Fig. 4.5a. Here red dashed lines labeled as WA_A and magenta dashed lines labeled as WA_S represent positions for air and substrate respectively.

Table 2 *The calculated wavelengths at which surface plasmons (SP) or Wood's anomaly (WA) are expected in Au nanohole array.*

λ-SP_A	(i, j)	λ-SP_S	(i, j)	λ-WA_A	(i, j)	λ-WA_S	(i, j)
1218	(1, 0)	2168	(1, 0)	407	(1, 0)	724	(1, 0)
703	(1, 1)	1251	(1, 1)	235	(1, 1)	418	(1, 1)
460	(2, 1)	819	(2, 1)	203	(2, 0)	362	(2, 0)
351	(2, 2)	625	(2, 2)	-	-	273	(2, 1)
-	-	-	-	-	-	209	(2, 2)

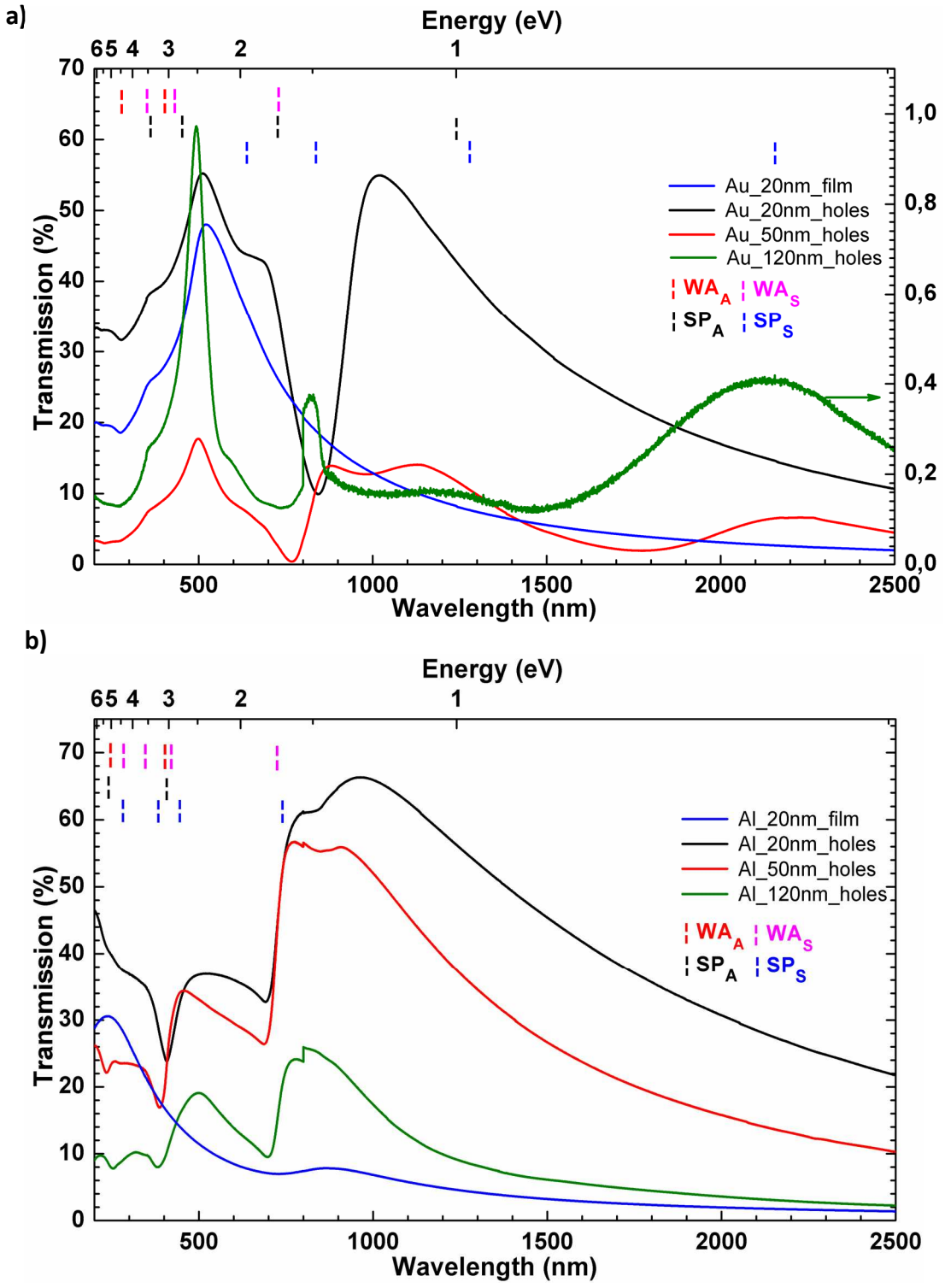

Fig. 4.5 *UV-Vis-NIR transmission spectra: a) Gold and b) Aluminum films with a thickness of 20 nm (blue line) and films with hole arrays showing differences in their spectral features. The film thickness is 20 nm, 50 nm and 120 nm and is represented with black, red, and green color line respectively. The red, pink, black and blue dashed lines denote the calculated positions at which Wood's anomaly and surface plasmons are expected. The A and S letter the metal - air and metal - sapphire interfaces respectively.*

One has to keep in mind that the Eq. 2.21 doesn't take into account the physical presence of the holes it just makes use of an array. It also doesn't consider the associated scattering losses. Besides, it neglects the interference between a predicted by Bethe direct transmission of light through the holes and the resonant one due to the excitation of surface plasmons, which can manifest with presence of Fano profiles on a spectra [120] and a red shift of the resonance [121].
The consequence of omission of the above facts is that calculated peak positions are at wavelengths slightly shorter than in experimental data presented in Fig. 4.5.
For the first approximation our calculations explain the features for wavelengths longer than 500 nm in the case of the 50 nm and 120 nm thick gold hole arrays [Fig. 4.5a, red and green line]. As it was mentioned before, at around 500 nm (2.5 eV), which is the wavelength region of the plasma edge and interband transition, the transmission is totally intermixed with peaks related to Wood's anomaly forming a complex pattern. Since this very simple single-interface-at-a-time approach is justified only for films that are much thicker than the field penetration depth (~20 nm), some discrepancy is expected for the 20 nm film. For this optically very thin film, a strong contribution resulting from the direct transmission is expected.
The shift of the peak is attributed to the coupling of the surface plasmons on both interfaces of the film and thus directly to the thickness of the metal film [122, 123].
Figure 4.5b shows the spectra for aluminum films. Once again the blue line represents the transmission spectrum for a solid film with thickness of 20nm. Here at 800 nm (1.5 eV) the known through related to interband transition is pronounced [124, 125]. In contrast to the gold spectra, the spectra for the aluminum films showed essentially similar results for the different film thicknesses; except for the overall scaling. Additionaly, there are no pronounced peaks related to a surface plasmon overlapped with interband transition edge in the visible. Besides, a bulk plasmon for Aluminum appears at high energy (15.2 eV) [126] which is beyond our interest). Unlike to the case of gold we didn't observe any features in the strongly subwavelength regime, i.e., for wavelengths larger than 1000 nm. The features below 750 nm are most likely due to Wood's anomalies. Both troughs near 700 and 400 nm have a Fano profile, pointing towards Wood anomalies mediated by surface plasmons. As for gold we have performed calculations to theoretically find the wavelengths at which the surface plasmons as well as Wood's anomaly could be present. The calculated data are present in the table 3.

Table 3 *The calculated wavelengths at which surface plasmons (SP) or Wood's anomaly (WA) are expected in Al nanohole array.*

λ-SP_A	(i, j)	λ-SP_S	(i, j)	λ-WA_A	(i, j)	λ-WA_S	(i, j)
408	(1, 0)	730	(1, 0)	407	(1, 0)	724	(1, 0)
230	(1, 1)	442	(1, 1)	235	(1, 1)	418	(1, 1)
		395	(2, 0)	203	(2, 0)	362	(2, 0)
		280	(2, 1)	-	-	273	(2, 1)
-	-	-	-	-	-	209	(2, 2)

The calculated values are plotted on Fig. 4.5b with the same symbols and color-scheme as for the gold samples. One can see that theoretical calculations stay in very good agreement with experimental results (keeping in mind the slight red shift which origin has been discussed before). It has been revealed that the feature at 750 nm is not just the result of broad plasma edge transmission peak. Here, we encounter the same situation as for the gold perforated films. The interband transition through is preceded by a peak attributed to a surface plasmon resonance, which is responsible for enhanced transmission of light in these wavelengths region. These features are followed by trough at 724 nm being a direct result of Wood's anomaly forming together a Fano profile. The same explanation applies to features which are present at higher energies. Here the most emphasized is a peak at around 500 nm and a trough at around 400 nm. In overall scaling, one can observe that all of the features tend to shift towards shorter wavelengths while the perforated film thickness is increased. This is the effect of the aspect ratio between the holes diameter and their depth, the same as described for the gold samples.

Additionally for both materials angle-dependent transmission measurements have been performed for the 50 nm thick films (Fig. 4.6). Already small changes in the incidence angle marked changes in zero-order transmission spectra which were recorded every 2°. In the case of Au at around 1000 nm a change in intensity and a shift of the structure with simultaneous peak splitting and movement in opposite directions is recognizable (Fig. 4.6a red dotted line). Such behavior can indicate the development of a band structure.

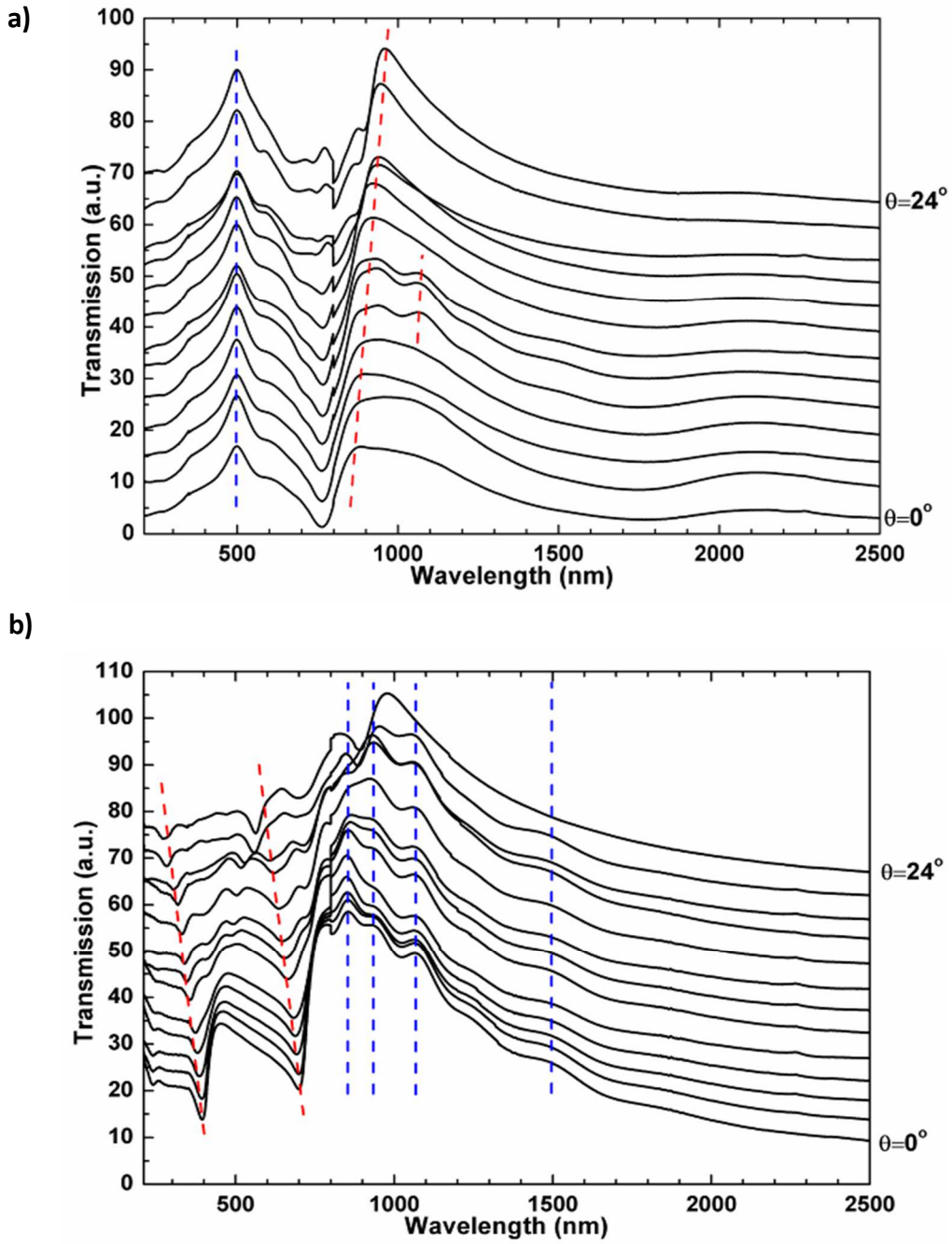

Fig 4.6 *Angle of incidence dependent optical spectra of a 50 nm thick perforated films. Blue and red dashed lines mark the features in spectra remaining on and changing their positions for: (a) gold and (b) aluminum as film material, respectively.*

To confirm this statement angle dependent measurements were performed, mapping the optical band structure for incident angles up to 24° along the ΓK-direction of the hexagonal array [Fig. 4.7]. In the graph the evolution of the peak at around 1000 nm

can be followed. Additionally, the calculated dispersion relation for the SP 2-1 mode (for the metal-substrate interface extended for the different incidence angles [127] Eq. 2.21) is included in the picture (dashed line). This calculated curve matches the measured (dotted line) dispersion very well and indicates the creation of the band structure, more precisely a plasmonic band structure since this peak is attributed to a surface plasmon. The peak at 500 nm remains on its position while the incidence angle is changed (blue dotted line in Fig. 4.6).

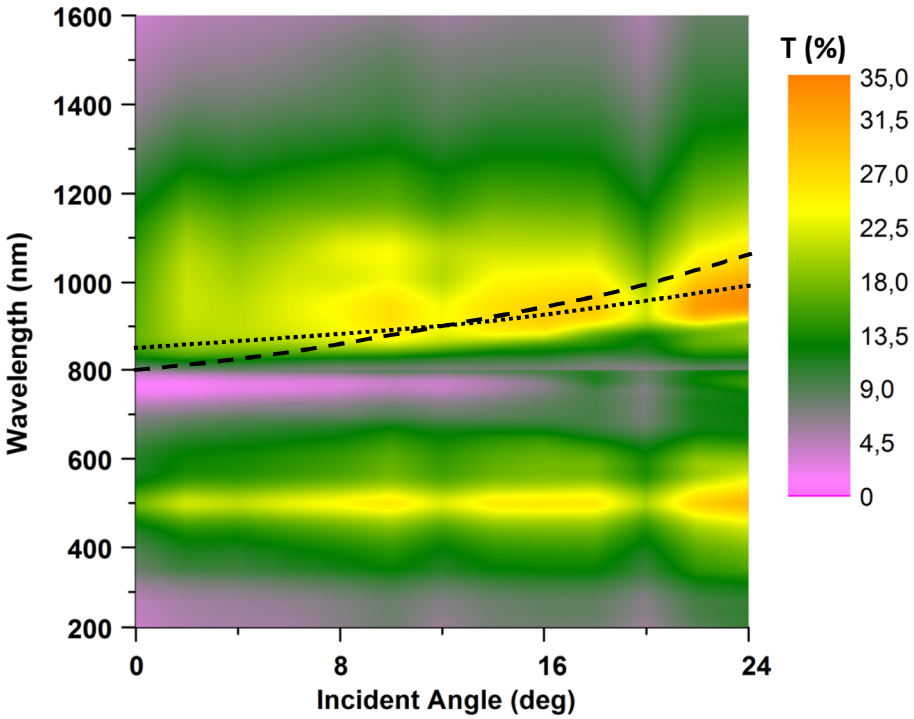

Fig. 4.7 *Angle dependent measurements of 50 nm thick gold perforated film along the Γ K-direction of the hexagonal array. The dotted line denotes the evolution of the measured SP peak, dashed line – theoretically calculated dispersion of the SP (2, 1) mode for the metal – substrate interface.*

For 50 nm thick perforated Al film the two high-energy troughs at 400 and 700 nm respectively are shifting (Fig. 4.6b red dotted lines) with increasing k parallel ($k_x = \left|\vec{k}_0\right| \sin\theta$). To prove the correct interpretation of these features, the results of angle dependent measurements were presented as a map of optical response, were one can follow the evolution of the recorded peaks and troughs [Fig. 4.8]. The changing positions of the surface plasmons are marked with black dashed lines indexed with the corresponding mode number. The Wood's anomaly related troughs are denoted with black dotted lines. Due to the change of the angle of incidence one

can observe that the Wood's anomaly give a rise to a set of minima which closely follow the measured maxima of the SP dispersion. Additionally the calculated dispersions of the two surface plasmons modes are denoted with red dashed lines, and they prove the correct interpretation of the corresponding to them measured surface plasmon modes. These confirm that recorded surface plasmon dispersion curves for aluminum film with subwavelength holes indicate the creation of the plasmonic band structure, as it was presented in the case of gold samples, but unexpectedly Al manifests richer plasmonic band structure in the visible regime than gold perforated films.

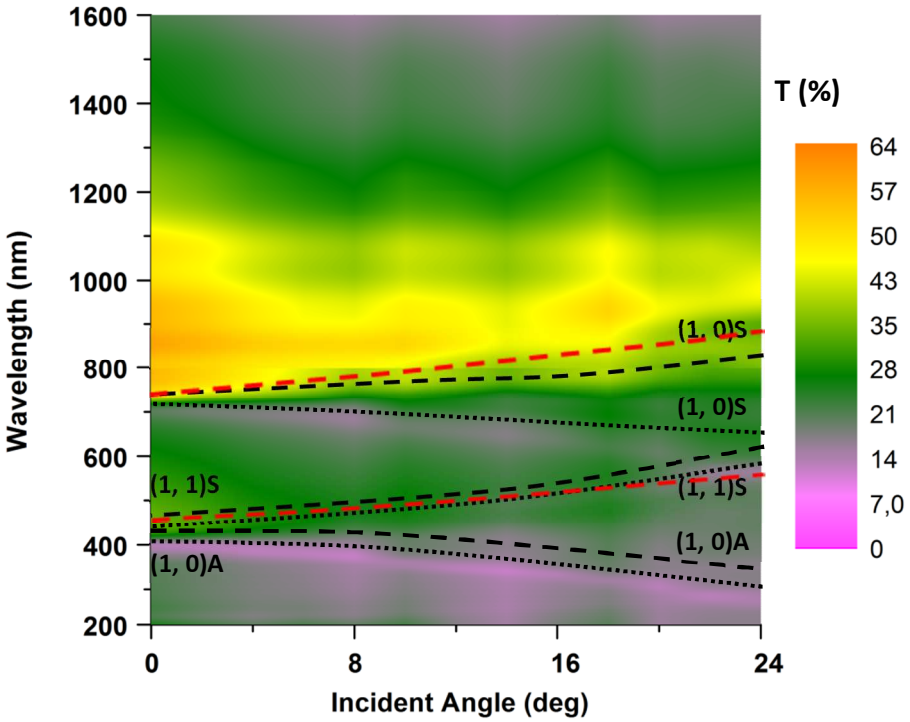

Fig. 4.8 *Angle dependent measurements mapping of 50 nm thick aluminum perforated film. The black dashed lines denote the evolution of the measured surface plasmons peaks and dotted lines indicate the Wood's anomaly troughs, excited on: S - metal–substrate and A - air–metal interface. The red dashed lines represent the calculated dispersion of (1, 0)S and (1, 1)S surface plasmons.*

For a more detailed study of the origin of enhanced transmission near-field measurements were performed. The results of these measurements are presented in the following section.

4.3.2 Near field results

Following the far-field characterization of the Au and Al hole arrays, we have carried out studies on the near-field optical behavior of the light transmission to determine and point out the main transmission channel for the light through the perforated film. The experiments were performed in illumination mode, giving us the opportunity to locally illuminate the sample using a wavelength of 442 nm. In Fig. 4.9 the results for the gold nanohole arrays with a different film thicknesses of - 20 [a) and b)], 50 [c) and d)], and 120 nm [e) and f)], are presented. The hole diameter of all samples was set to 250 nm. The topography images (upper row) where taken simultaneously with optical images (bottom row).

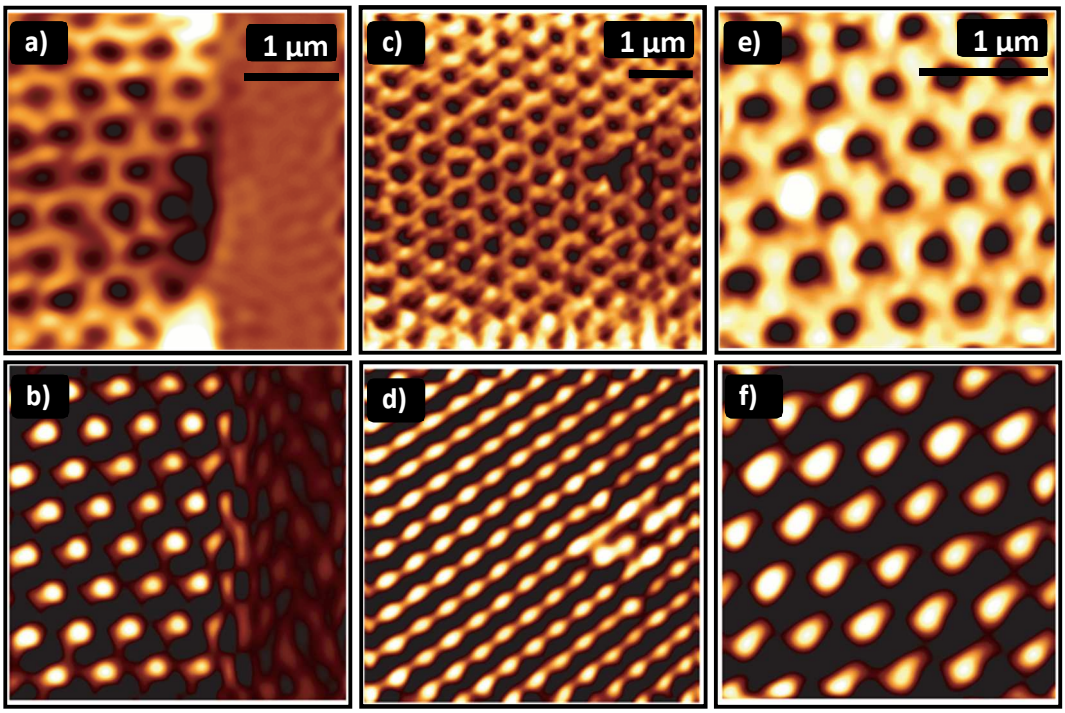

Fig. 4.9 *SNOM images of the Au hole arrays. Top row: Topography images of the samples indicating an interhole distance of~500 nm and a hole diameter of 250 nm. Bottom row: Near-field optical images taken at a wavelength of 442 nm. The recorded light intensity shows an enhanced transmission through the sub-wavelength holes. The thickness of the deposited films is 20 nm (a,b), 50 nm (c,d), and 120 nm (e,f), respectively.*

Comparing now the simultaneously recorded optical and topography images reveal a high transmission of the light directly at the position of the holes. This effect is observable for all of the film thicknesses and might be explained by the direct light

transmission through these subwavelength holes, which is enhanced and supported by the excitation of surface plasmons. The optical images also reveal an elongation of the circular hole-shaped light spots especially in the case of the two thinner films, which on first look would point out to a tip-artifact. However, this is a direct result of the polarization of the incoming light. The elongation is parallel to the direction of the polarization and indicates coupling of the locally launched surface plasmons by the tip of a scanning near-field optical microscope [54, 128] and SPs at the film - air interface. These surface plasmons propagate along the surface of the film until they encounter a hole. There they are scattered into a radiative mode possibly by direct interaction with the edges of the holes. For the thinner films, i.e., 20 and 50 nm thickness, the more probable scenario is that they directly couple to SP modes on the opposite interface of the film and are then scattered into radiative modes [129]. In contrast to the surface plasmon contribution to the measured light intensity, the intensity of the central spots in Fig. 4.9b, d, and f is essentially independent of the light polarization. Thus this peak is attributed to direct transmission through the hole of propagating light modes emitted by the SNOM tip.

The structured films are optically thin enough that they can exhibit intense direct transmission through the film, which is beyond the interest of these measurements. Therefore the contrast of the optical images in Fig. 4.9 had to be increased to emphasize the transmission modulation caused by the nanostructures. The differences between original and contrast-enhanced pictures are shown in Fig. 4.10, which clearly demonstrates the need of filtering of the intensity coming from the direct transmission through the film.

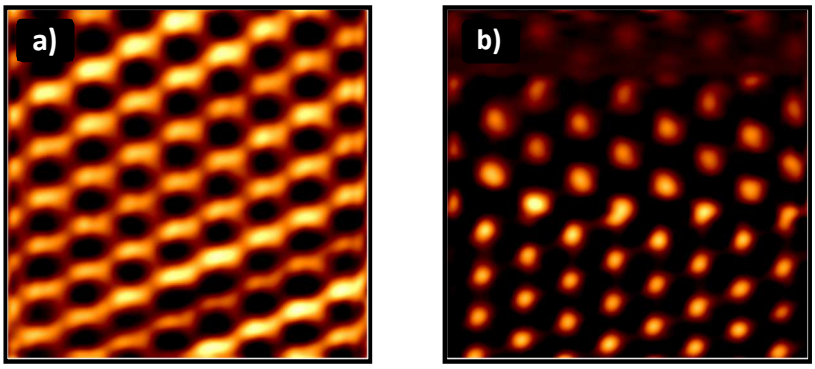

Fig. 4.10 *SNOM optical images a) without enhancement of the contrast and b) with enhanced contrast. The latter shows the direct transmission of the light through the nanoholes.*

Additionally, valid optical images must precisely correlate with the simultaneously recorded topography. If such a correlation does not exhibit then such images are artificial unless some chemical or physical changes were created locally on a surface during a scan without significant changes of the topography [130]. In these results such extra effects are unexpected. To prove that our interpretation of the optical images is correct, we measured at a defect, i.e., a scratch, in the 100 nm thick gold film [Fig. 4.11].

Here, only the optical image is shown. The gold film on the left-hand side of the picture has been removed and the bare sapphire substrate is visible. The line indicates the position of the cross section, which is present in the graph at the right-hand side. The black line indicates the topographic signal at the same position. The clearly visible step represents the boundary of the scratch. The blue line shows the optical intensity along this line. One can see that on the left-hand side the optical signal is stronger than on the side with the film. The large intensity enhancement at the border is an artifact of the measurement technique. Comparing the position of the intensity maxima with the position of the holes (minima in the topographic signal), our interpretation of the contrast in Fig. 4.9 is confirmed since the intensity maxima lie at the position of the holes.

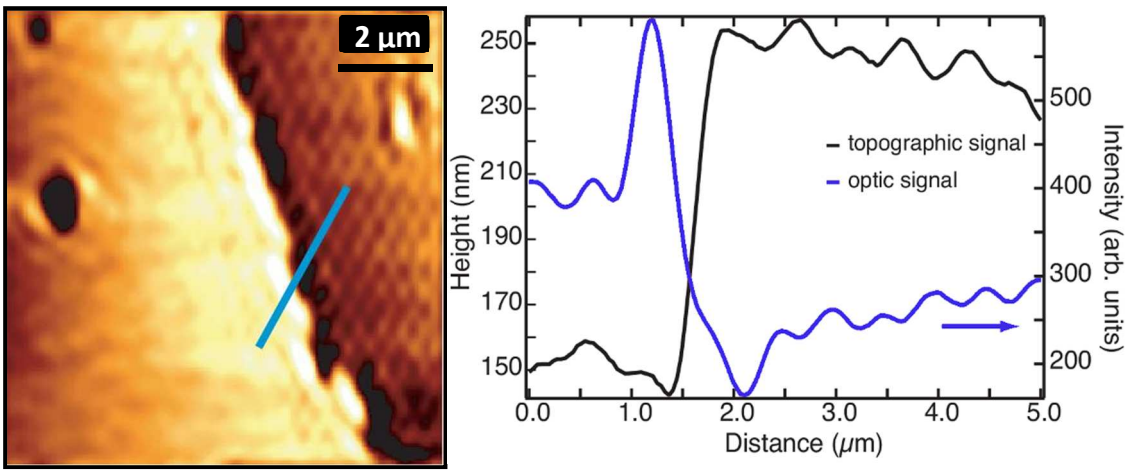

Fig. 4.11 *SNOM image of a scratch in the hole array of the 100 nm-thick Au film. The measured contrast indicates a light transmission through the holes. This is confirmed by the line scan given on the right. The maxima in optical transmission fall into the minima of the topography signal.*

Following the thorough studies on gold structured films, near-field optical transmission through apertures in aluminum films was investigated for comparison. The results are presented on Fig. 4.12, identical as in the case of gold samples a top row represents

topography images for 20 nm [a)], 50 nm [c)] and 120 nm [e)] thick aluminum films. The bottom row reflects optical signal measurement results for 20 nm [b)], 50 nm [d)], and 120 nm [f)] adequately thicknesses taken simultaneously with topography, thus the films had the same thicknesses as the gold equivalents. Exactly as in the case of gold, the observed contrast shows an enhanced transmission of light through the holes and is mostly the result of a direct transmission through the hole of propagating light, with surface plasmon enhancement. In Fig. 4.12 similar to Fig. 4.9 one can observe the elongation of the spots of transmitted light at the position of the holes. This is again connected to the polarization direction. In addition, the influence of the present native oxide layer on those aluminum films was not taken into account, leaving room for further experiments and theoretical calculations to clarify its possible role in the transmission enhancement.

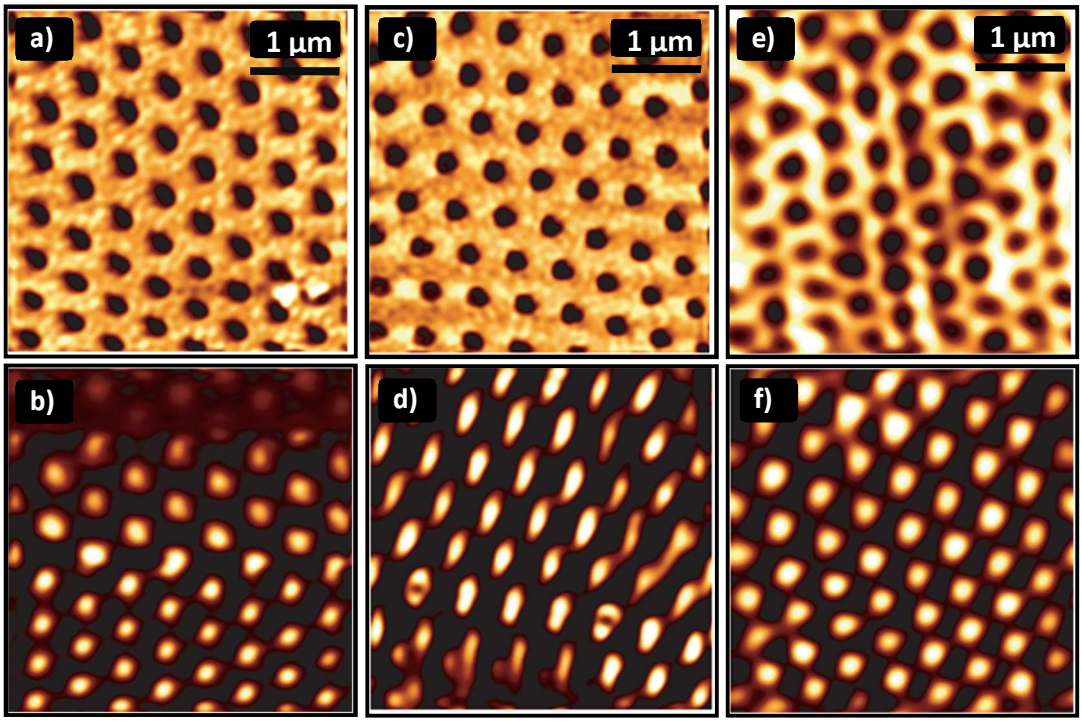

Fig. 4.12 *SNOM images of the hole arrays in the Al films. Left column: Topography images of the samples indicating an inter-hole distance of 500 nm and a hole diameter of 250 nm. Right column: Near-field optical images at a wavelength of 442 nm. The recorded light intensity again shows an enhanced transmission through the sub-wavelength holes. The thicknesses of the deposited films are 20 nm (a,b), 50 nm (c,d), and 120 nm (e,f), respectively.*

To better understand the processes governing the light propagation through our hole arrays, 3D FDTD simulations [131] were performed in the group of Prof. Kempa

(Boston College), modeling the field distribution in our films [132]. They have used periodic boundary conditions associated with the hexagonal hole structure, and absorption conditions to truncate the directions parallel to the film surface. The thickness of the film was taken to be 50 nm, the inter-hole distance is 500 nm, and the diameter of the holes d = 250 nm, to match the experimental conditions. The discretization step size of 2 nm assures good numerical convergence. The time-domain auxiliary differential equation approach was used to implement the FDTD method to our case of the dispersive metal. The frequency-dependent permittivity of Au was taken from Ref. [131]. The in-plane field intensity profiles shown in Fig. 4.13 are calculated in a single unit cell, at 10 nm away from the film surface, on the far side of the film. The chosen color-coding scheme shows high-intensity regions in a darker color. The light wavelength is λ=442 nm in Fig. 4.13a, and λ=1000 nm in Fig. 4.13b. The insets show the corresponding in-plane electric field amplitude profiles across the film. In the marginal subwavelength regime ($d < \lambda$, Fig. 4.13a), the overall transmission of light through the film and holes is very high (mostly due to the plasmon enhancement), as shown in the inset. The corresponding in-plane intensity map shows that the transmission is larger inside the holes, which stays in a very good agreement with the experiment. In the strongly subwavelength regime ($d << \lambda$, Fig. 4.13b), the light propagation through the metal is marginal (in part since little plasmon enhancement occurs in this range), but is quite large through the holes. This is obvious from the inset showing out of plane field intensity, as well as, the corresponding in-plane intensity map. An overall transmission coefficient through this film at this wavelength (λ = 1000 nm) is much smaller than that for λ = 442 nm, as evidenced by the insets in Fig. 4.13a and b. A maximum in transmission coefficient is indeed observed at λ= 442 nm in all curves in Fig. 4.5a, followed by a smaller, much broader maximum at λ= 1000 nm.

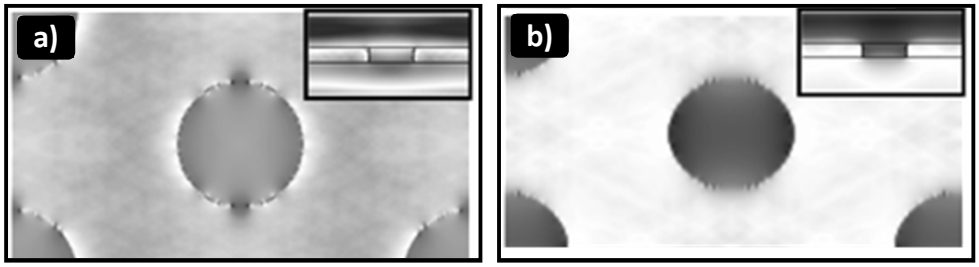

Fig. 4.13 *Simulation of the light transmission through the Au film with an array of holes. Parameters: inter-hole distance: 500 nm, hole diameter 250 nm, film thickness 50 nm, wavelength of the light is 442 nm (a), and 1000 nm (b). Main figures show light intensity 10 nm away from the film surface on the far side. Darker regions represent higher intensity. Insets show the corresponding in-plane electric field amplitudes.*

4.4 Plasmonic properties of an array of nanowires: Gold and Iron

Since Ebbesen reported enhanced transmission on arrays of subwavelength holes in metal films [17], many research groups started to investigate the possibility of enhanced transmission in different structures. In particular, one-dimensional reflection and transmission gratings have been widely studied. Throughout the last two decades a great number of theoretical [134-149], as well as experimental investigations [61, 116, 150-165] have been carried out. In the beginning of the 1990s, resonances of TM polarized light (electric field vector of incident light perpendicular to the wires) were discovered on gold-wire gratings [162]. It was shown experimentally as well as numerically that these kind of resonances can yield to almost 100% transmission of the incident light for highly conducting grating wires. Among those many interesting and unexpected optical characteristics of complex origin have been found. Scientists reported that depending on the geometrical parameters numerous effects can be found, such as: cavity modes [148, 150], Wood-Rayleigh anomalies [141, 148], as well as different types of surface plasmon resonances (horizontally oriented SPs (HSPs), SPs coupled on air - metal interfaces and vertically oriented SPs on the vertical walls of opposite sides of the grooves of the gratings) [148, 154]. The excitation of surface plasmons on wire gratings has been extensively studied since 1994 [60]. Further studies revealed later that the excitation of surface plasmons plays a key role in the enhanced transmission that was observed [142, 166]. These grating like structures have found potential applications in various fields, as optical polarizers [159, 160], color filtering devices [158, 161, 163], in solar cells [155], for biosensing [165] and for the generation of second and higher harmonics [163]. The complex optical response with addition of possible application in various fields makes these structures a very valuable material class. This is the reason why there is such a demanding need for low-cost fabrication techniques comparable to the semiconductor industry.

NSL leaves us with the ability to prepare such structures of similar - grating like morphology (see chapter 3.7). These 1-D morphologies can exhibit completely different properties than those presented in the previous sections for two dimensional structures. Thus, in the following section will focus on the optical characterization of the prepared nanowire arrays.

4.4.1 Far field results

In this section we present the optical characterization of the nanowire arrays. The typical far field transmission spectra are shown in Figure 4.14 and Figure 4.16. As distinct from hole arrays, we have decided to use iron instead of aluminum as a second material. The reason is a possible use of this sample in future characterizations of magnetic properties, i.e., magnetic force measurements. The spectra were taken on samples covered with Au [Fig. 4.14] and Fe [Fig. 4.16] with the following parameters: line width: 140 nm, thickness of Au or Fe: 35 nm, the distance between lines varies from 210 nm and 255 nm as mentioned in section 3.7. All spectra cover a range between 200 and 2500 nm and were referenced to the transmission spectrum of a bare sapphire substrate. The measurement consists of a series of spectra where the sample is rotated clockwise from 0° to 90°. This allows to study the influence of the light polarization to the transmitted intensity.

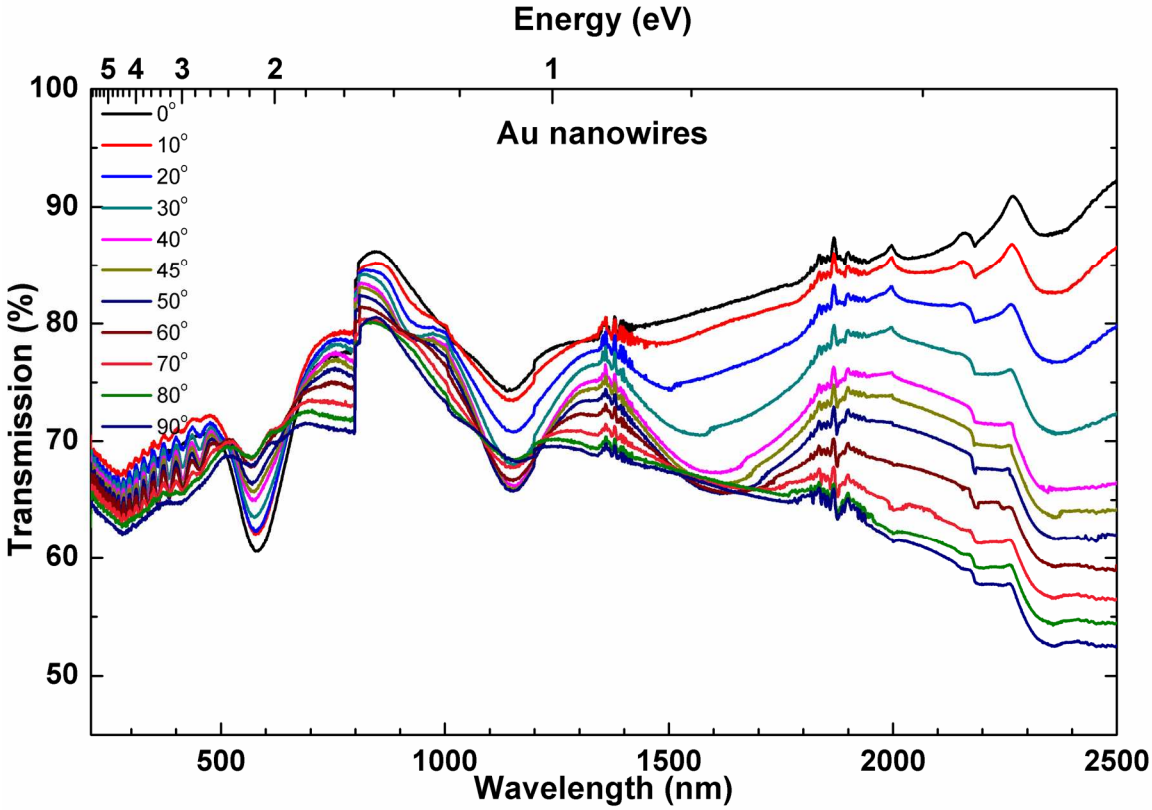

Fig. 4.14 *UV-Vis-NIR transmission spectra of the gold nanowires with a thickness of 35 nm. Each spectrum is taken after rotation of 10° of the sample (according to its previous position) showing differences in the spectral response.*

In Fig 4.14, a well pronounced trough in the transmission spectra at around 590 nm (2.1 eV) is observed for TM polarization (electric field vector of incident light perpendicular to the wires). While the polarization is gradually changed to TE polarization, the depth of this trough is reduced while simultaneously shifting to 572 nm. This feature is directly related to material properties, i.e., a localized plasmon resonance in an individual gold wire [157, 167]. The strongest resonant absorption of this band is only visible for TM polarization where the electric field of the incident light is inducing collective plasma oscillations in the wire. While the polarization is changed the oscillation becomes less pronounced and finally when the electric field vector is parallel to the wire, it vanishes, due to the infinite dimension in the direction where a plasma resonance could occur. Unlike to nanoparticles, where a spherical geometry allows for a polarization independent plasmon excitation, plasmon resonances in a nanowire can only be excited by an electric field oriented perpendicular to the wire axis (only in this direction the spatial confinement of the electrons is provided by the interface of the nanowire and the adjacent medium) [143, 151]. Since these nanowires are packed in between to dielectric materials (sapphire substrate and air) it should be possible to excite the surface plasmons at both sides. The missing momentum is provided by the grating vector, thus one can make use of Eq. 2.17 and calculate the wavelength at which surface plasmon could occur. Because measurements were carried out at normal incidence of light, thus for theoretical considerations Eq. 2.18 applies. Yet, this equation has to be modified, due to the fact that it omits the presence of interface between metal and adjacent medium. Thus the wavelength at which SP resonance along the plane that comprises the metal/substrate interface of each nanowire is expected to occur at [168]:

$$\lambda_{SP} = \frac{a_0}{m}\sqrt{\frac{\varepsilon_m \varepsilon_d}{\varepsilon_m + \varepsilon_d}} \qquad \text{Eq. 4.3}$$

where a_0 is a grating periodicity, m is the order of the grating vector, ε_m and ε_d are the dielectric constants of metal and adjacent dielectric (air and sapphire).
The calculated wavelengths are presented in the table 4.

Table 4 *Calculated wavelengths at which surface plasmon resonance is expected.*

λ-SP_A	(m)	λ-SP_S	(m)
380	1	585	1
191	2	292	2

For a clear view these results are depicted in the Fig. 4.15, and are denoted with the dashed line symbols (black - surface at metal – air SP_A and blue at metal – substrate SP_S interface). The solid black line in the Fig. 4.15 represents the transmission spectrum for the TM polarization of the light. Here, one can observe that the calculated position for SP_s (m=1) matches the aforementioned trough at 2.1 eV and the SP_s for the higher order of the grating vector (m=2) also stays in agreement with the experimentally measured trough at around 290 nm. On both: Fig. 4.14 and Fig. 4.15 a trough at around 1150 nm is possible to observe. This feature could belong to the surface plasmon resonance SP_s (m=1), however for two times longer grating vector (two times larger period of the grating). Then, this SP would be expected at 1170 nm which stays very good in agreement with the measured value.

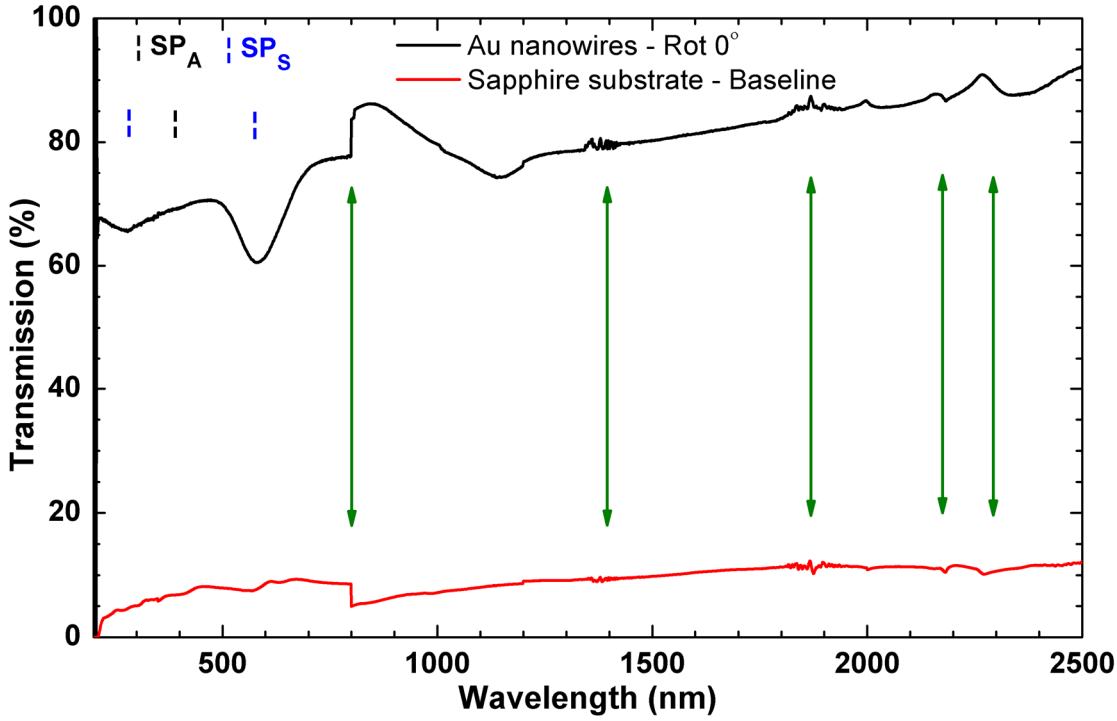

Fig. 4.15 *Transmission spectrum of the gold nanowire array – black line vs. bare sapphire substrate – red line.*

For the TE polarization (rotation angle 90°) one can observe a peak at around 620 nm. For this “enhanced” transmission an electromagnetic resonance in the gap between the wires is responsible, which is not connected to a surface plasmon mode [158]. One can also observe a series of features in the strong subwavelength regime at 930 nm, and 1600 nm. Since these troughs appear for polarizations between the TM and TE one has to exclude an excitation of surface plasmons since symmetry forbids an excitation for polarizations other than TM [147]. Most likely these features are due to grating effects. Further experiments to understand the origin of these troughs better are currently in preparation. In the Fig. 4.14 in a higher energy range, for wavelengths shorter than 500 nm a series of small peaks is visible. These features are typical for the thin film interference. Here, the incoming light interferes with the light which is reflected from the back side of the 35 nm thick Au nanowire.
Figure 4.15 includes also a bare sapphire substrate spectrum (red line) which was used as a baseline for measurements of gold and iron nanowire arrays. Comparing both spectra of gold nanowires (black line) and baseline one can still observe influence of sapphire substrate on the results (green arrows) of the measurements of the gold nanowires array. This points towards spectrophotometer baseline correction problem. The two noisy features at 1400 nm and 1850 nm belong to the water vapors absorption bands [169]. Additionally, the sudden drop in transmission at 800 nm is visible. This is a measurement artifact which arose from wrong calibration and appeared by the change of the detectors from infrared to visible inside the spectrometer.

For better understanding of the plasmonic response of this structure the same measurements were performed on a geometrically identical Fe nanowire array. Figure 4.16 shows transmission spectra for the same manipulation of the polarization of the incoming light as in the case of Au wires. Since iron doesn’t exhibit plasmonic properties in the visible regime, one can’t observe a particle plasmon transmission trough at around 2.1 eV. Like the spectra for the gold wires, the far field characterization for the iron grating shows essentially similar results for the different polarization directions. The features in the IR region are present at nearly the same frequencies as in the gold case. This confirms rather a geometric origin of these features than a plasmonic one. Only a peak at around 900 nm is better visible than in the case of gold. The transmission of light through the iron wires has a maximum intensity for TM polarization. This is apparent for the whole spectral range. There are more similarities to the gold nanowire grating, like the features at wavelengths shorter than 700 nm arising from interference resulting from the thickness of the wires. Due to different refraction index of iron compared to gold, these features are present already

at lower frequencies than in the gold structures. Still one can observe the same experimental artifacts in the results, such as the step in transmission signal at 800 nm or the bad baseline correction at the same wavelengths as for Au sample.

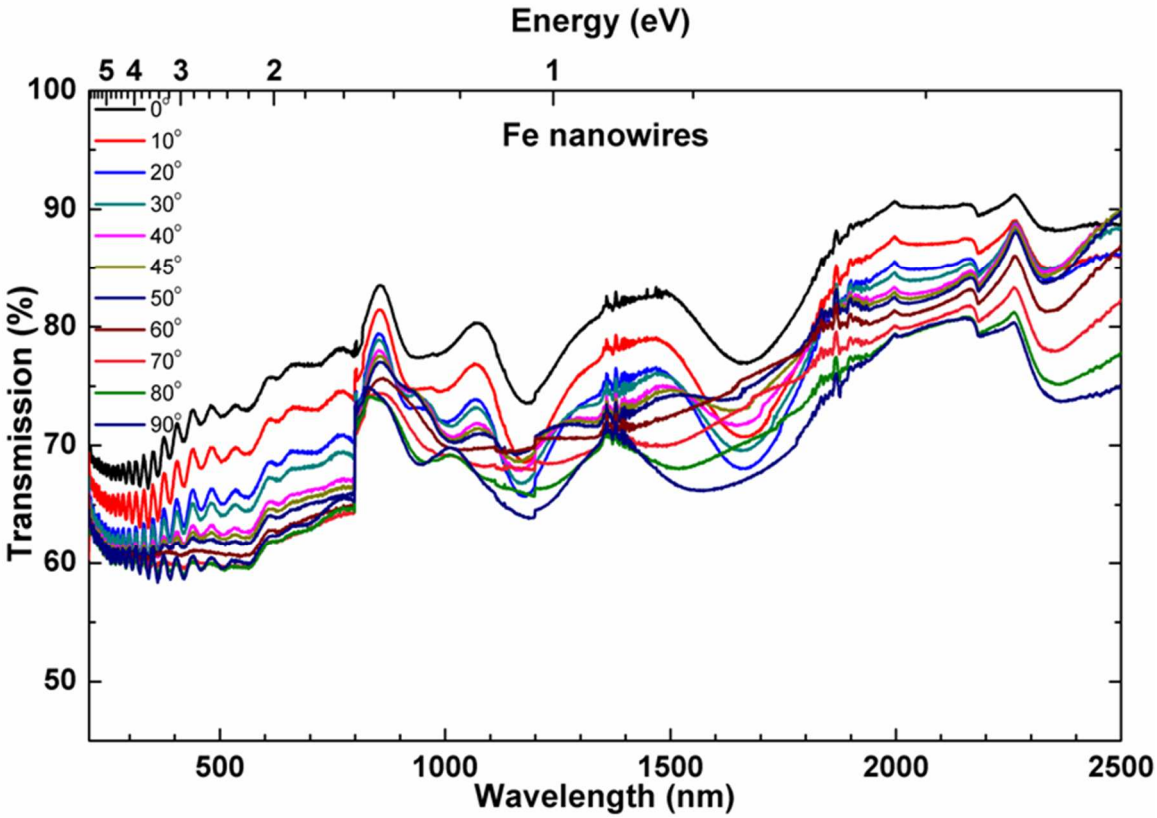

Fig. 4.16 *UV-Vis-NIR transmission spectra of iron nanowires with a thickness of 35 nm. Each spectrum is taken after rotation of 10° of the sample (according to its previous position) showing differences in the spectral response.*

Figure 4.17 shows an intensity map for a full rotation of the Au [Fig. 4.17a] and Fe [Fig. 4.17b] sample, where spectra were taken every 5°. It expresses a remaining in high symmetry optical response of the samples on the impinging light. In Fig. 4.17a one can observe a periodic vanishing and recovering of the feature at 2.1 eV (590 nm) as well as an overall drop in transmission intensity with the polarization change from TM to TE. This is due to a fact that such a nanowire array acts like a wire-grid polarizer, which allows only the vertically aligned electric field to pass more efficiently. In Fig. 4.17b an intensity map for different incident light polarizations for Fe nanowires array is shown. Here one can observe the evolution of the signal arising from interference in the nanowire thickness. Interesting is the fact that this feature is more emphasized for

other rotation angles than for gold sample. The investigations of the origin of this discrepancy are in preparation. It is also possible that some of the effects of the optical response are not very pronounced. This is due to the fact that EBE deposition does not allow the preparation of monocrystalline wires. The polycrystalline wires might prevent large propagation lengths of surface plasmons due to their roughness [170].

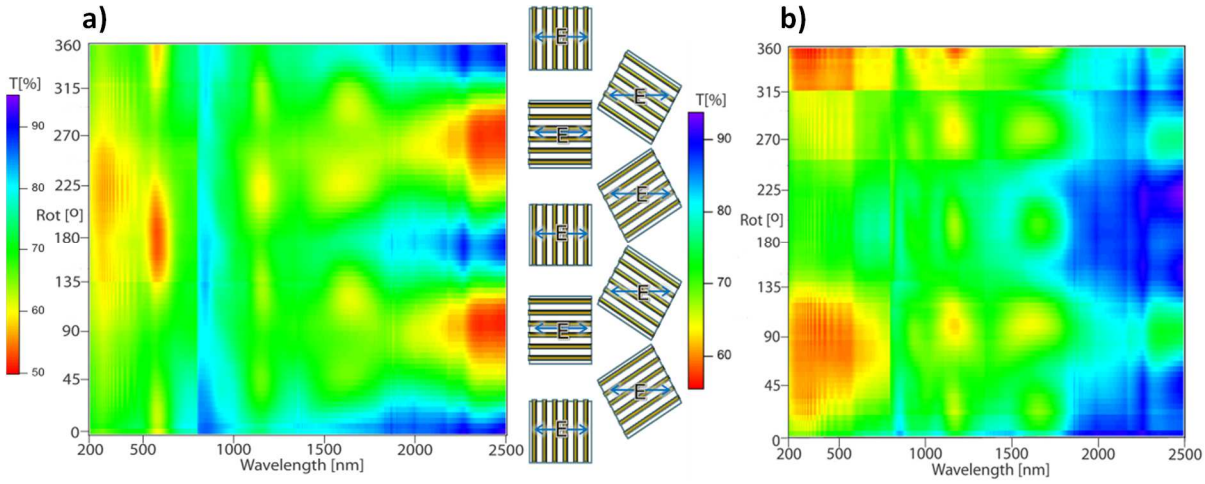

Fig. 4.17 *Transmission spectra map of a nanowire array with 35 nm thick a) Gold and b) Iron wires. Both samples show high symmetry in transmission depending on the change of polarization. In between of the transmission maps the position of the electrical vector in relation to the nanowire grating is schematically shown.*

Following the far field measurements a study of the behavior of the light transmission through the Au grating-like structure in the near field has been carried out.

4.4.2 Near field results

We have performed the experiments in illumination mode, which gave us the possibility for local illumination of the sample. Figure 4.18 presents the near-field images for 35 nm thick gold wires for two light polarizations: a) TE - parallel and b) TM - perpendicular to the lines. The topographic and the optical signal were recorded simultaneously (Fig. 4.18 left and right respectively).

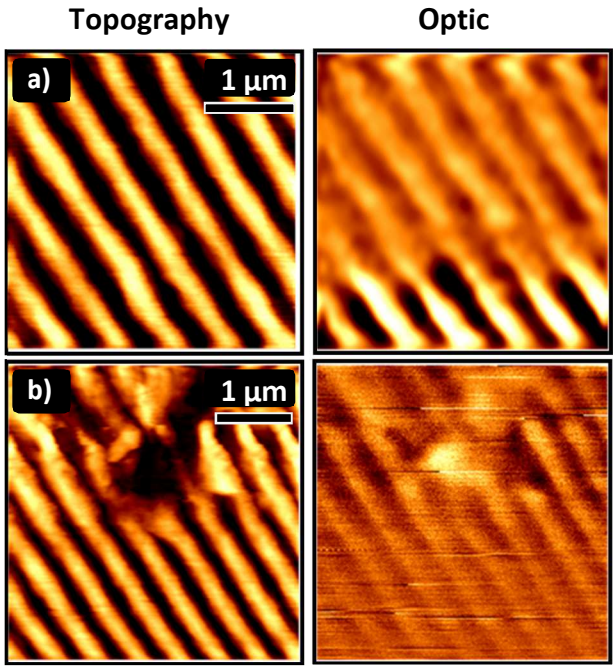

Fig. 4.18 *SNOM images of the Au nanowire array. Left column: Topography images of the samples. Right column: Near-field optical images taken at λ = 442 nm. The light intensity shows a direct transmission through a 240 nm broad gap between wires for two different light polarizations: a) parallel and b) perpendicular to the lines.*

The resolution of around 100 nm in the optical image results from the aperture of the coated fiber. The resolution limits us from obtaining more detailed information on enhanced transmission through the grating. Despite this fact the presented results reveal a direct transmission at the position of the gaps. Additionally, the optical image reveals that the transmitted light-lines are slightly broader than the gaps between the wires. This effect is visible for both polarization directions of the light but more pronounced for the TM polarization [Fig. 4.18b] At first glance this could be related to the partial transmission of the light through the nanowire-film. A second possible explanation is based on the excitation of a localized surface plasmon in the gold wire. It was mentioned in section 4.3.2 that it is possible to couple the locally excited surface plasmons by the tip of a scanning near-field optical microscope [54, 128] and the SPs between the wire and air interface. These surface plasmons propagate along the surface of the wire until they encounter an edge. Then they are transformed into radiation. Moreover, the surface plasmons on gold are damped much stronger when propagating along the surface compared to plasmons excited in silver. The propagation of the surface plasmon is along the direction of the electric field. This approach may explain the increased intensity of the signal in the vicinity of the line edges and its dependence on the light polarization. When the light is TE polarized then the coupled

surface plasmon will propagate along the line edges and as a result of an infinite resonator length it will decay. If the light is TM polarized the surface plasmon will propagate perpendicular to the lines and will couple into a photon when reaching the line edge.

5. Conclusions and Outlook

The preparation of various shaped nanostructures, as well as the results on their structural characterization were presented in chapter 3. Depending on the desired morphology of the structure, the fabrication includes self assembly of a colloidal mask and its modification, followed by a material deposition process. In chapter 4 the optical characterization of previously prepared samples was carried out with an emphasis on plasmonic properties. In this section a conclusion on the obtained experimental results will be given.

The creation of a hcp monolayer of spheres, which exhibit a long range order is crucial for the fabrication of large areas of defect free arrays of nanostructures. Therefore, the quality of the produced crystals was estimated by observations of the iridescence coloring caused by the diffraction of white light illuminating the sample (section 3.1 Fig. 3.2). By choosing the size of the spheres used for colloidal mask preparation (section 3.1 Fig. 3.4). One has a huge influence on the geometric parameters of the final morphology of the structures (Section 3.5 especially Fig. 3.10). Nanostructures of various shapes can be obtained by additional processing of the masks in order to control their interparticle voids. For instance for 440 nm spheres the reactive ion etching (RIE) method provides the smooth reduction of their diameter through a change in processing time (Fig. 3.7). The experimental results have also shown that a disturbance of the hexagonally aligned spheres (Fig. 3.8a), caused by the plasma - treatment can be effectively inhibited by 5 – 10 s pre-annealing of a mask on a heating plate at 105 °C before RIE (Fig. 3.8b).
After or before the etching process the mask orientation on the substrate can be determined by diffraction pattern where a laser beam is diffracted on the periodic monolayer crystal. The hexagonally arranged diffraction spots (Fig. 3.18a) corresponding to the six-fold symmetry of the layer provide the necessary information

on the quality of the monolayer and orientation of the mask. The latter determines the evaporation direction (Fig. 3.18b) for the preparation of nanowire arrays (section 3.7). The combination of mask processing and sample orienting during the material deposition process results in creation of different shaped nanostructures. The simplest to obtain are thereby triangular-shaped nanoislands (section 3.5). It is shown that the triangles'size can be well controlled by the choice of the appropriate diameter of the PS-spheres used (Fig. 3.10 and Fig. 3.11) and by evaporation of the desired thickness of the material (structures height Fig. 3.10d).

It was shown that an etching process of the colloidal mask together with perpendicular evaporation of the material results in hexagonal arrays of subwavelength holes. The geometric parameters such as: interhole spacing, mesh diameter, and the perforation depth directly depend on the initial (Fig. 3.17) and the etched (Fig. 3.14) sphere size as well as on the deposited material thickness (Fig. 3.15), respectively. The preparation of the nanowires is the most complicated, since it requires not only the reduction of the sphere size but also the determination of the crystal orientation on the substrate together with a proper sample alignment during the evaporation process. The measured values of width, spacing, and thickness of the wires (Fig. 3.20), can again be controlled via the sphere diameter used for assembly of the mask (Fig. 3.21), latex particle diameter after the etching process, and thickness of the deposited material.

The NSL-based ordered Au triangular particles were examined for their optical properties. The far field investigation results are dominated by plasmon resonances of different orders. This resonant response on the light is correlated with the size and thus the circumference of the individual triangle, which is directly connected to the size of the latex particles used for the preparation of the mask (Fig. 3.11 and Eq. 4.2). Simulations performed in the group of Prof. Kempa [105] are in excellent agreement with the experiment, and confirm that observed effects are governed by a surface/edge plasmon polariton resonating in these nanoparticles. In general, the regime of plasmonic response can be tuned by judicious choice of the sphere diameter for the mask assembling process.

Extending the single hole to a periodic array of subwavelength holes in a metal film results in an extraordinary transmission through the film, as was shown by Ebbesen and co-workers [17]. In our experiments, we have shown that the transmission of the light through a hexagonal array of subwavelength holes in a metallic film is governed by surface plasmons and Wood anomalies. The spectra can be completely understood with help of these two phenomena, which was confirmed with calculations using the Eq. 2.21 and Eq. 2.23. It was presented that the spectral response is dependent on the geometric properties of the structure and the optical properties, i.e., the dielectric function of the metal. The first ones can be controlled by the choice of the desired

sphere size and the etching parameters during the structure preparation. The optical properties can be controlled through selection of the various materials used for the deposition process. The metal's environment plays also a very important role since surface plasmons excitation as well as propagation is possible on the metal / dielectric interface. Thus, the proper choice of the dielectric medium can mediate the plasmonic properties. The change of incidence angle of the light also influences the optical response of the sample. Increase of the angle can either enlarge or decrease the component of the incident photon's wavevector in the plane of the array (Eq. 2.19). One can shift spectral features which belong to different plasmonic orders and are excited at different dielectric environment towards longer or shorter wavelengths, simultaneously creating a plasmonic band structure (Fig. 4.7). It is shown that theses plasmonic bands can be separated or approached to each other (Fig. 4.8). Depending on the metal it is also possible to separate the optical responses which originate from the material and structural properties. In case of gold nanohole structures, the plasmonic response overlaps with materials interband transition (Fig. 4.5a). The use of aluminum let us to separate these responses (Fig. 4.5b). This leaves us enough place to tune the plasmonic answer for the desired spectral range. It has been observed that the intensity of the transmitted light through the holes overcame the proposed limit of around 10^{-3} of the incoming light. This is achieved, as already mentioned, by extending the single hole to an array and thus, giving the possibility to excite the surface plasmon polaritions using thereby the array to overcome momentum mismatch. The latter ones are responsible for the extraordinary transmission of the light. Additionaly, near-field investigations showed that, although the films were optically thin and despite the huge background (Fig. 4.10), it was possible to identify the propagation path of the light (Fig. 4.9, Fig. 4.11 and Fig. 4.12). We clearly saw a plasmon-assisted enhanced transmission through the subwavelength holes, which is in excellent agreement with theoretical calculations prepared in the group of Prof. Kempa [132]. As it was mentioned, the plasmonic response is assisted by a closely following Wood's anomaly. These features are independent of the material from which the film with holes is made of, but they strongly depend on the dielectric function of the environment and symmetry of the structure (Eq. 2.23).

We have shown that use of magnetic material for creation of the hole array, can influence the optical response of the structure; these results are not presented in this thesis. The light transmission through such a film strongly depends on the external magnetic field. The change of this field influences and tunes the position of the surface plasmons which govern the transmission of the light. We were the first to report on these magneto-plasmonic experimental measurements [171].

In the case of the nanowire array, it has been presented that TM polarized light is transmitted more efficiently through the structure, than TE polarized light. Therefore, such a nanowire grating can be used directly as an optical polarization device. In addition it has been pointed out that the plasmonic response from a grating made of gold is also affected by slight changes of the light polarization (Fig. 4.14). The change of polarization from TM to TE revealed the possibility to control the transmission efficiency of light in the wavelength region from 500 to 700 nm (Fig. 4.14) which is governed by surface plasmons (Fig. 4.15). Our nanowire grating can therefore act as a band polarizer. The working band could moreover be tuned by choosing a material with different optical properties (Fig. 4.16). It has been also observed that for the high energy regime of the optical response the interference in the film thickness is responsible. The regime of this answer can also be controlled by judicious choice of the material.

The presented optical characteristics of different types of structures which were mainly made of gold are just a small part of measurements that can be done.
All of the experimental results fit very well to the proposed theories on surface plasmon excitation in different types of nanostructures presented in this thesis. It will be very useful to test these theories for nanostructure arrays of different morphologies and various materials. Change of some structural parameters, i.e., hole diameter, interhole distance, wire width, spacing, periodicity, height (thickness) can have a tremendous influence on the optical response of the samples in far field spectroscopy. Further investigations concerning the wavelength dependence of the transmission in the near field can be a valuable reference in detailed understanding of proceeded effects.
It was presented that structural parameters of the samples can be well controlled with NSL giving an opportunity to prepare not only the nanostructures of the same morphology and different geometrical parameters but also of different shape. Combining it with a material deposition technique such as electron beam evaporation, where a large number of materials can be used, opens up a vast space of possibilities. It will be very interesting to investigate how polycrystallinity of the structures influences the plasmonic response of the samples in comparison to monocrystalline samples, i.e., how scattering losses and random scattering can alter the excitation and propagation of the surface plasmon polaritons. It is known that monocrystalline structures cannot be prepared by electron beam evaporation. Therefore, use of some post processing such as thermal annealing should be applied. Nanosphere lithography allows the preparation of masks on various substrates, thus gives us a direct control on

the dielectric environment of the fabricated structures. The change of the ε_d leads to changes in the surface plasmon position in the spectra (Eq. 2.21).

It would be also very interesting to separate the direct transmission of light from that assisted by plasmon. This could be achieved by use of grazing incident light. Thus, one should observe the vanishing of the Fano profile of the resonance in the spectrum, which in our case is present due to interference of the non resonant (direct) and resonant (surface plasmon polariton assisted) transmission. Subwavelength holes can be used as cavities which can be filled with nanoparticles or quantum dots. This procedure will locally affect the dielectric function. Thereby a change in the transmission efficiency or the plasmonic response of the holes is expected. Furthermore, in the case of quantum dots, one expects a change in the emission rate through the changed local density of states of the surrounding medium.

The variety of future experiments can reveal many interesting properties of such nanostructures, which can be used for application in many scientific as well as industrial areas.

In summary, the optical characterization gave us the answer to the question which was the basis for this thesis, namely: Is it possible to control the plasmonic response of the nanostructure? This can be done by judicious choice of sample material and morphology. Certainly, the method which was used in this thesis for preparing the nanostructures leaves us the freedom to control the structural parameters such as the sample shape, resulting in triangular nanoislands, arrays of subwavelength holes or nanowires. Moreover, it is a tool to control the morphology of each type of nanostructure. It allows to fabricate triangular nanoislands of different size, arrays of holes with different interhole distance, hole diameter and depth, and also nanowires with different width, spacing and height. By changing these parameters, it is possible to change the absorption or transmission properties to the desired wavelength regions and therefore manipulate the light propagation through the film, the latter being the main aim in the field of plasmonics.

6. Summary

The present work introduces shadow nanosphere lithography as a time – efficient and low – cost lithographic method to produce large arrays of nanostructures. We thereby use 2D colloidal crystals made of polystyrene (PS) spheres that serve as the lithographic mask. Using different materials and evaporating them at different angles onto the mask leaves the freedom of producing nanostructures of various shapes, for which investigations of optical properties were carried out. It has been presented that structures of different morphologies and made of different materials exhibit interesting optical response on the incident light. It appeared, that mainly these responses are driven by the excitation of the surface plasmons.

We have presented far field characterization of arrays of triangular shaped nanostructures made by deposition of gold material through masks assembled by use of different size of spheres. Such a structure exhibit a strong localized surface plasmon response, whose spectral position as well as number of excitations is strongly dependent on the circumference of single nanostructure. This geometrical parameter can be well controlled by use of desired sphere size for mask assembling. Thus giving us a tool to manipulate the plasmonic response of such structure. It has been also presented that depending on the order of the excited plasmon it originates from different effects. Lower orders are surface/edge plasmons and higher orders are related to Mie resonances.

The modification of the colloidal mask by use of reactive ion etching allows us to prepare arrays of subwavelength holes with hexagonal symmetry. The type of symmetry differs from the squared lattices of holes being under a great interest in last decade because of their enhanced light transmission properties. Our investigations in far - as well as in near - field showed that our mesh, with single hole diameter of 250 nm, which were made of gold and aluminum exhibit also extraordinary transmission of light. The spectral responses are dominated by two phenomena, namely: surface

plasmons and Wood's anomalies, which are strongly dependent on samples' material and geometric parameters. The near – field measurements carried out by scanning near – field optical microscopy revealed the transmission of light through the subwavelength holes. This is possible due to the coupling of surface plasmons excited on both sides of the metal film (air - metal and metal – substrate interface). This statement is confirmed by theoretical simulations. The last characterized samples were nanowires fabricated in a shape of an array forming a grating - like structure. Investigations of these structures revealed a change in intensity of the transmitted light. It has been shown that this effect is strongly dependent on the polarization of the incident light. Additionally, it has been presented that gratings made of gold exhibits a plasmonic response which is also polarization dependent. In summary, this thesis presented that it is possible to control the plasmonic response of the nanostructure. The response can be tuned by proper choice of sample's material and morphology. Both of these properties can be adjusted by use of shadow nanosphere lithography as a method for sample fabrication. The plasmonic properties of these structures together with simplicity and low-cost preparation method make them a promising material for application in many scientific and industrial branches.

7. Appendix

7.1 Abbreviations

1D – one-dimensional
2D – two-dimensional
3D- three dimensional
AFM – atomic force microscope(y)
EBE – electron beam evaporator
FDTD - finite-difference time-domain
hcp – hexagonal closed-pack
LSPR – localized surface plasmon resonance
MACS – multiplex atmospheric cassette system
NIR – near infrared
NMP – 1-methyl 2-pyrrolidone
NSL – nanosphere lithography
PMMA - poly-methylmethacrylate
PS – polystyrene
QCM – quartz crystal microbalance
RIE – reactive ion etching
SEM – scanning electron microscope(y)
SERS – surface enhanced Raman spectroscopy
SNOM – scanning near-field optical microscope(y)
SNSL – shadow nanosphere lithography
SP – surface plasmon
SPASER – surface plasmon amplification by stimulated emission of radiation
SPP – surface plasmon polariton
TE – transverse electric
THF – tetrahydrofuran
TM – transverse magnetic
UV – ultra violet
Vis – visible

7.2 Tables of applied materials

Within this section materials and chemicals used for preparation of experimental samples are listed. Table 4 contains information about colloidal particles that were used for preparations of lithographic colloidal masks. The substrates used for mask transfer and metal deposition are listed in Table 5**.** Different organic solvents used for preparation of colloidal particles dispersions and for mask removal process after material evaporation are presented in Table 6.

Table 5 *Information about colloidal particles for mask preparation*

Colloidal Particles			
No.	Name, article No. ; batch No.	Company	Description
1	Surfactant-free sulfate white polystyrene latex PS440 nm; 1-500; 2140	Interfacial Dynamics Corporation (IDC), USA	Dispersed in de-ionized water; Diameter: 440 nm; CV = 3.0%; Surface with sulfate groups; negatively charged: 5.2 µC/cm2; Percent solids: 4 %;
2	Surfactant-free sulfate white polystyrene latex PS470 nm; 1-500; 1713	Interfacial Dynamics Corporation (IDC), USA	Dispersed in de-ionized water; Diameter: 470 nm; CV = 2.6%; Surface with sulfate groups; negatively charged: 4.9 µC/cm2; Percent solids: 6.9 %;
3	Surfactant-free sulfate white polystyrene latex PS540 nm; 1-500; 2028	Interfacial Dynamics Corporation (IDC), USA	Dispersed in de-ionized water; Diameter: 540 nm; CV = 2.2 %; Surface with sulfate groups; negatively charged: 6.3 µC/cm2; Percent solids: 8 %;
4	Polystyrene plain particles PS980 nm; PS-R-1.0; PS-R-B288	Microparticles GmbH	Dispersed in de-ionized water; Diameter: 980 nm; CV = 4%; Surface with sulfate groups; negatively charged; Percent solids:8%;
5	Poly(methyl metacrylate) particles PMMA 1060 nm; PMMA-R-1.0; PMMA-F-L1057-1	Microparticles GmbH	Dispersed in de-ionized water; Diameter: 1060 nm; Percent solids: 10%

Table 6 *Information about substrates for colloidal mask transfer and metal deposition*

Colloidal Particles			
No.	Name, article No. ; batch No.	Company	Description
1	Sapphire wafer; ALA76D05C2; PO#51214/05	MTI corporation, USA	Formula: $Al_2O_3(\alpha)$, A-plane crystal; purity 99.99%; Surface roughness <0.5nm
2	Silicon wafer; SIA76B05D4;PO#81624/05	Si-Mat Silicon Materials	Formula: Si; <100>; purity 99.99%; Surface roughness <1 nm

Table 7 *Information about solvents for colloidal mask removal*

Colloidal Particles			
No.	Name, article No. ; batch No.	Company	Description
1	1-methyl 2-pyrrolidone (NMP); 8.06072.1000	Merck	C_5H_9NO, pure for analysis (99.5%)
2	Ethanol (EthOH); Rotipuran® 9065.4	Carl Roth GmbH	C_2H_6O, pure for analysis (99.8%)
3	2-Propanol; Rotipuran® 6752.4	Carl Roth GmbH	C_3H_8O, pure for analysis (99.8%)
4	Acetone; Rotipuran® 9372.5	Carl Roth GmbH	C_3H_6O, pure for analysis (99.8%)
5	MiliQ water: PURELAB MAXIMA	USF ELGA	Ultra-pure, de-ionized water (18.2 MΩcm)
6	Tetrahydrofuran THF; 4745.3	Carl Roth GmbH	C_4H_8O, pure for synthesis (99.5%)
7	Toluene; Rotipuran® 7115.2	Carl Roth	C_7H_8, pure for analysis (99.5%)

7.3 List of figure captions

8. References

[1] Drexler, K. E. Nanosystems: Molecular Machinery, Manufacturing, and Computation; John Wiley & Sons Ltd., New York **(1992)**

[2] Drexler, K. E. Engines of Creation: The Coming Era of Nanotechnology; Anchor Books, USA **(1986)**

[3] Hall, J. S. Nanofuture: What's Next For Nanotechnology; Prometheus Books, New York **(2007)**

[4] Brongersma, M. L.; Kik, P. G. Surface Plasmon Nanophotonics; Springer **(2007)**

[5] Bergmann, D. J.; Stockman, M. I. Surface Plasmon Amplification by Stimulated Emission of Radiation: Quantum Generation of Coherent Surface Plasmons in Nanosystems, Phys. Rev. Lett. **(2003)**,90, 027402

[6] Noginov, M. A.; Zhu, G.; Belgrave, A. M.; Bakker, R.; Shalaev, V. M.; Narimanov, E. E.; Stout, S.; Herz, E.; Suteewong, T.; Wiesner, U. Demonstration of spaser-based nanolaser, *Nature* **(2009)**, 460, 1110

[7] Kim, S.; Jin, J.; Kim, Y. J.; Park, I. Y.; Kim, Y.; Kim, S. W. High-harmonic generation by resonant plasmon field enhancement, Nature **(2008)**, 453, 757

[8] Zijlstra, P.; Chon, J. W. M.; Gu, F. Five-dimensional optical recording mediated by surface plasmons in gold nanorods, Nature **(2009)**, 459, 410

[9] Tominaga, J. Surface Plasmon Nanophotonics: Localized Surface Plasmons for Optical Data Storage Beyond the Diffraction Limit, Springer Series in Optical Sciences **(2007)**, 131, 235

[10] Mansuripur, M.; Zakharian, A. R.; Lesuffleur, A.; Oh, S-H.; Jones, R. J.; Lindquist, N. C.; Im, H.; Kobyakov, A.; Moloney, J. V. Plasmonic nano-structures for optical data storage, Opt. Express **(2009)**, 17, 16, 14001

[11] O'Connor, D.; Zayats, A. V. Data storage: The third plasmonic revolution, Nature Nanotechnology **(2010)**, 5, 482

[12] Homola, J. Surface Plasmon Resonance Based Sensors, Springer, New York **(2006)**

[13] Loo, C; Lin, A.; Hirsch, L.; Lee, M.; Barton, J.; Halas, N.; West, J.; Drezek, R. Nanoshell-Enabled Photonics-Based Imaging and Therapy of Cancer, Technology in Cancer Research & Treatment **(2004)**, 3, 1, 33

[14] Fourkal, E.; Velchev, I.; Taffo, A.; Ma, C.; Khazak, V.; Skobeleva, N. Photo-Thermal Cancer Therapy Using Gold Nanorods, World Congress on Medical Physics and Biomedical Engineering **(2009)**, IFMBE Proceedings, 25, 761

[15] www.sciencedirect.com

[16] Takahara, J.; Yamagishi, S.; Taki, H.; Morimoto, A.; Kobayashi, T. Guiding of a one-dimensional optical beam with nanometer diameter, Opt. Lett. **(1997)**, 22, 475

[17] Ebbesen, T. W.; Lezec, H. J.; Ghaemi, H. F.; Thio, T.; Wolff, P. A. Extraordinary optical transmission through subwavelength hole arrays, Nature **(1998)**, 391, 667

[18] Pendry, J. Negative refraction makes a perfect lens, Phys. Rev. Lett. **(2000)**, 85, 396

[19] Veselago, V. G. The Electrodynamic of substances with simultaneously negative values of ε and μ, Usp. Fiz. Nauk. **(1967)**, 92, 517

[20] Alù, A.; Engheta, N. Emission Enhancement in a Plasmonic Waveguide at Cut-Off, Materials **(2011)**, 4, 1, 141

[21] Bozhevolnyi, S. I. Plasmonic Nanoguides and Circuits, Pan Stanford Publishing Ptc. Ltd., Singapore **(2009)**

[22] Zouhdi, S.; Sihvol, A.; Vinogradov, A. P. Metamaterials and Plasmonics: Fundamentals, Modelling, Applications, NATO Science for Peace and Security Series B: Physics and Biophysics, Springer **(2009)**

[23] Cui, T. J.; Smith, D.; Liu, R. Metamaterials: Theory, Design, and Applications, Springer, New York **(2009)**

[24] Sommerfeld, A. Fortpffanzung elektrodynamischer Wellen an einem zylindnschen Leiter, Ann. der Physik und Chemie **(1899)**, 67, 233

[25] Mie, G. Beiträge zur Optik trüber Medien, speziell kolloidaler Metallösungen, Ann. Phys. **(1908)**, 330, 377

[26] Barnes, W. L. Comparing experiment and theory in plasmonics, J. Opt. A: Pure Appl. Opt. **(2009)**, 11, 114002

[27] Liz-Marzán, L. M.; Correa-Duarte, M. A.; Pastoriza-Santos, I.; Mulvaney, P.; Ung, T.; Giersig, M.; Kotov, N. A. Handbook of Surfaces and Interfaces of Materials: Core-Shell Nanoparticles and Assemblies Thereof, Vol. 3, Ch. 5, Academic Press, San Diego **(2001)**

[28] Kittel, C. Introduction to Solid State Physics, Wiley: New York **(1956)**

[29] Link, S.; El-Sayed, M. A. Spectral Properties and Relaxation Dynamics of Surface Plasmon Electronic Oscillations in Gold and Silver Nanodots and Nanorods, J. Phys. Chem. B **(1999)**, 103, 40, 8410

[30] Kreibig, U.; Vollmer, M. Optical Properties of Metal Clusters, Springer, Berlin **(1995)**

[31] Krebig, U.; Genzel, L. Optical Absorption of Small Metallic Particles, Surf. Sci. **(1985)**, 156, 678

[32] Mulvaney, P. Surface Plasmon Spectroscopy of Nanosized Metal Particles, Langmuir **(1996)**, 12, 3, 788

[33] Hosteler, M. J.; Wingate, J.E.; Zhong, C. J. Alkanethiolate Gold Cluster Molecules with Core Diameters from 1.5 to 5.2 nm: Core and Monolayer Properties as a Function of Core Size, Langmuir **(1998)**, 14, 1, 17

[34] Gans, R. Über die Form ultramikroskopischer Goldteilchen, Ann. Phys. **(1912)**, 342, 881

[35] Lisiecki, I.; Billoudet, F.; Pilenii, M. P. Control of the Shape and the Size of Copper Metallic Particles, J. Phys. Chem. **(1996)**, 100, 10, 4160

[36] S. Link, M. B. Mohamed, and M. A. El-Sayed, Simulation of the Optical Absorption Spectra of Gold Nanorods as a Function of Their Aspect Ratio and the Effect of the Medium Dielectric Constant, J. Phys. Chem. B **(1999)**, 103, 16, 3073

[37] Drude, P. Zur Elektronentheorie der metalle, Ann. Phys. **(1900)**, 306, 3, 566

[38] Drude, P. Zur Elektronentheorie der Metalle: II. Teil. Galvanomagnetische und thermomagnetische Effecte, Ann. Phys. **(1900)**, 308, 11, 369

[39] Tonks, L.; Langmuir, I. Oscillations in Ionized Gases, Phys. Rev. **(1929),** 33, 195

[40] Fröhlich, H.; Pelzer, H. Plasma Oscillations and Energy Loss of Charged Particles in Solids, Proc. Phys. Soc. **(1955)**, A68, 525

[41] Raether, H. Surface Plasmons, Springer-Verlag, Berlin **(1998)**

[42] Sambles, J. R.; Bradbery, G. W.; Yang, F. Z. Optical-excitation of surface-plasmons - an introduction, Contemp. Phys. **(1991),** 32, 173

[43] Burstein, E.; De Martini, F. Polaritons, Pergamon Press, New York **(1974)**

[44] Ritchie, R. H. Plasma Losses by Fast Electrons in Thin Films, Phys. Rev. **(1957)**, 106, 5, 874

[45] Kanazawa, H. On the Plasma Oscillations in Metal Foils, Prog. Theor. Phys. **(1961)**, 26, 851

[46] Otto, A. Exitation of nonradiative surface plasma waves in silver by the method of frustrated total reflection, Z. Phys. **(1968)**, 216, 398

[47] Kretschmann, E.; Raether, H. Radiative decay of nonradiative surface plasmons excited by light, Z. Naturforsch. **(1968)**, A23, 2135

[48] Pitarke, J. M.; Silkin, V. M.; Chulkov, E. V.; Echenique, P. M. Theory of surface plasmons and surface-plasmon polaritons, Rep. Prog. Phys. **(2007)**, 70, 1

[49] Papavassiliou, G. C. Optical properties of small inorganic and organic metal particles, Prog. Solid st. Chem **(1979)**, 12, 3-4, 185

[50] Kerker M. The Scattering of Light and Other Electromagnetic Radiation, Academic Press: New York **(1969)**

[51] Bohren, C. F.; Huffman, D. R. Absorption and Scaterring of light by small Particles, Wiley: New York **(1983)**

[52] Liz-Marzan, L. M. Tailoring Surface Plasmons through the Morphology and Assembly of Metal Nanoparticles, Langmuir **(2006)**, 22, 1

[53] Noguez, C. Surface Plasmons on Metal Nanoparticles: The Influence of Shape and Physical Environment, J Phys Chem. C **(2007)**, 111, 10, 3806

[54] Hecht, B.; Bielefeldt, H.; Novotny, L.; Inouye, Y.; Pohl, D. W. Local excitation, scattering, and interference of surface plasmons. Phys. Rev. Lett. **(1996)**, 77, 1889

[55] Ditlbacher, H.; Krenn, J. R.; Felidj, N.; Lamprecht, B.; Schider, G.; Salerno, M.; Leitner, A.; Aussenegg, F. R. Fluorescence imaging of surface plasmon fields Appl. Phys. Lett. **(2002)**, 80, 404

[56] Ritchie, R. H.; Arakawa, E. T.; Cowan, J. J.; Hamm, R. N. Surface-plasmon resonance effect in grating diffraction. Phys. Rev. Lett. **(1968)**, 21, 1530

[57] Wood, R. W. On a remarkable case of uneven distribution of light in a diffraction grating spectrum, Phil. Mag. **(1902)**, 4, 396

[58] Moreland, J.; Adams, A.; Hansma, P. K. Efficiency of light emission from surface plasmons, Phys. Rev. B **(1982)**, 25, 2297

[59] Worthing, P. T.; Barnes, W. L. Efficient coupling of surface plasmon polaritons to radiation using a bi-grating, Appl. Phys. Lett. **(2001)**, 79, 3035

[60] Lochbihler, H. Surface polaritons on gold-wire gratings, Phys. Rev. B **(1994)**, 50, 4795

[61] Lochbihler, H. Surface polaritons on metallic wire gratings studied via power losses ,Phys. Rev. B **(1996)**, 53, 10289

[62] Ghaemi, H. F.; Thio, T.; Grupp, D. E.; Ebbesen, T. W.; Lezec, H. J. Surface plasmons enhance optical transmission through subwavelength holes, Phys. Rev. B **(1998)**, 58, 6779

[63] Wood, R. W. On a remarkable case of uneven distributin of light in a diffraction grating spectrum, Philos. Mag. **(1902)**, 4, 396; Wood, R. W.; Hopkins, Anomalous Diffraction Gratings, J. Phys. Rev. **(1935)**, 48, 928

[64] Bethe, H. A. Theory of Diffraction by Small Holes, Phys. Rev. **(1994)**, 66, 163

[65] Kosiorek, A.; Kandulski, W.; Chudzinski, P.; Kempa, K.; Giersig, M. Shadow Nanosphere Lithography: Simulation and Experiment, Nano Lett. **(2004)**, 4, 1359

[66] Kosiorek, A.; Kandulski, W.; Glaczynska, H.; Giersig, M. Fabrication of Nanoscale Rings, Dots, and Rods by Combining Shadow Nanosphere Lithography and Annealed Polystyrene Nanosphere Masks, Small **(2005)**, 1, 4, 439

[67] Deckman, H. W.; Dunsmuir, J. H. Natural lithography, Appl. Phys. Lett. **(1982)**, 41, 377

[68] Giersig, M.; Mulvaney, P. Preparation of ordered colloid monolayers by electrophoretic deposition, Langmuir **(1993)**, 9, 12, 3408

[69] Hulteen, J. C.; Van Duyne, R. P.; Nanosphere lithography: A materials general fabrication process for periodic particle array surfaces, J. Vac. Sci. Technol. A **(1995)**, 13, 3

[70] Winzer, M.; Kleiber, M.; Dix, N.; Wiesendanger, R. Fabrication of nano-dot- and nano-ring-arrays by nanosphere lithography, Appl. Phys. A **(1996)**, 63, 6, 617

[71] Micheletto, R.; Fukuda, H.; Ohtsu, M. A Simple Method for the Production of a Two-Dimensional, Ordered Array of Small Latex Particles, Langmuir **(1995)**, 11, 9, 3333

[72] Burmeister, F.; Badowsky, W.; Braun, T.; Wieprich, S.; Boneberg, J.; Leiderer, P. Colloid monolayer lithography - A flexible approach for nanostructuring of surfaces, Applied Surface Science **(1999)**, 144-145, 461

[73] Denkov, N. D.; Velev, O. D.; Kralchevsky, P. A.; Ivanov, I. B.;Yoshimura, H.; Nagayama, K. Mechanism of formation of two-dimensional crystals from latex particles on substrates, Langmuir **(1992)**, 8, 12, 3183

[74] Kern, W.; Puotinen D. Cleaning solutions based on hydrogen peroxide for use in silicon semiconductor technology, RCA Review **(1970)**, 31, 187

[75] Sugawara, M. Plasma Etching: Fundamentals and Applications, Oxford University Press **(1998)**

[76] Madou M.J. Fundamentals of microfabrication, the science of miniaturization, second edition, CRC Press, London **(2002)**

[77] Kosiorek, A. Optical, Magnetical and Structural Properties of Periodic Metallic Nanostructures, PhD Thesis, Technical University of Poznań **(2007)**

[78] Mosier-Boss, P. A.; Lieberman, S. H. Comparison of Three Methods to Improve Adherence of Thin Gold Films to Glass Substrates and Their Effect on the SERS Response, Applied Spectroscopy **(1999)**, 53, 7, 862

[79] Sánchez-Iglesias, A.; Pastoriza-Santos, I.; Pérez-Juste, J.; Rodríguez-González, B.; García de Abajo, F. J.; Liz-Marzán, L. M. Synthesis and Optical Properties of Gold Nanodecahedra with Size Control, Adv. Mater. **(2006)**, 18, 2529

[80] Johnson, C. J.; Dujardin, E.; Davis, S. A.; Murphy, C. J.; Mann, S. Growth and form of gold nanorods prepared by seed-mediated, surfactant-directed synthesis, J. Mater. Chem. **(2002)**, 12, 1765

[81] Chen, C; H.; Wang, J.; Yu, H.; Yang, H.; Xie, S.; Li, J. Transmission Electron Microscopy Study of Pseudoperiodically Twinned Zn2SnO4 Nanowires, J. Phys. Chem. B **(2005)**, 109, 2573

[82] Wang, Z. L.; Mohamed, M. B.; Link, S.; El-Sayed, M. A. Crystallographic facets and shapes of gold nanorods of different aspect ratios, Surf. Sci. **(1999)**, 440, L809

[83] Kirkland, I.; Edwards, P. P.; Jefferson, D. A.; Duff, D. G. The structure, characterization, and evolution of colloidal metals, Rep. Prog. Chem.: Sect. C: Phys. Chem. **(1990)**, 87, 247

[84] Jin, R.; Cao, C. Y.; Hao, E.; Métraux, G.; Schatz, G. C.; Mirkin, C. A. Controlling anisotropic nanoparticle growth through plasmon excitation, Nature **(2003)**, 425, 487

[85] Lofton, C.; Sigmund, W. Mechanisms Controlling Crystal Habits of Gold and Silver Colloids, Adv. Funct. Mater. **(2005)**, 15, 1197

[86] Le Ru, E. C.; Etchegoin, P. G.; Grand, J.; Félidj, N.; Aubard, J.; Lévi, G.; Hohenau A.; Krenn, J. R. Surface enhanced Raman spectroscopy on nanolithography-prepared substrates, Cur. Appl. Phys. **(2008)**, 8, 467

[87] Galarreta, B. C.; Norton, P. R.; Lagugne-Labarthet, F. Hexagonal Array of Gold Nanotriangles: Modeling the Electric Field Distribution, J. Phys. Chem. C **(2010)**, 114, 47, 19952

[88] Bruchez, M.; Moronne, M.; Gin, P.; Weiss, S.; Alivisatos, A. P. Semiconductor nanocrystals as fluorescent biological labels, Science **(1998)**, 281, 2013

[89] Han,M.; Gao, X.; Su, J. Z.; Nie, S. Quantum-dot-tagged microbeads for multiplexed optical coding of biomolecules, Nature Biotechnol. **(2001)**, 19, 631

[90] Schmid, G. Large clusters and colloids.Metals in the embryonic state, Chem. Rev. **(1992)**, 92, 1709

[91] Sun, S., Murray, C. B., Weller, D., Folks, L.; Moser, A. Monodisperse FePt nanoparticles and ferromagnetic FePt nanocrystal superlattices, Science **(2000)**, 287, 1989

[92] Willets, K. A.; Van Duyne, R. P. Localized surface plasmon resonance spectroscopy and sensing, Annu. Rev. Phys. Chem. **(2007)**, 58, 267

[93] Haynes, C. L.; Van Duyne, R. P. Nanosphere Lithography: A Versatile Nanofabrication Tool for Studies of Size-Dependent Nanoparticle Optics, J. Phys. Chem. B **(2001)**, 105, 5599

[94] Sherry, L. J.; Jin, R.; Mirkin, C. A.; Schatz, G. C.; Van Duyne, R. P. Localized Surface Plasmon Resonance Spectroscopy of Single Silver Triangular Nanoprisms, Nano Lett. **(2006)**, 6, 9, 2060

[95] Sherry, L. J.; Chang, S. H.; Schatz, G. C.; Van Duyne, R. P.; Wiley, B. J.; Xia, Y. Localized Surface Plasmon Resonance Spectroscopy of Single Silver Nanocubes, Nano Lett. **(2005)**, 5, 10, 2034

[96] Huang, W. Y.; Qian, W.; El-Sayed, M. A. Coherent Vibrational Oscillation in Gold Prismatic Monolayer Periodic Nanoparticle Arrays, Nano Lett. **(2004)**, 4, 9, 1741

[97] Nie, S. M.; Emory, S. R. Probing Single Molecules and Single Nanoparticles by Surface-Enhanced Raman Scattering, Science **(1997)**, 275, 5303, 1102

[98] Zhao, J.; Das, A.; Zhang, X. Y.; Schatz, G. C.; Sligar, S. G.; Van Duyne, R. P. Resonance Surface Plasmon Spectroscopy: Low Molecular Weight Substrate Binding to Cytochrome P450, J. Am. Chem. Soc. **(2006)**, 128, 34, 11004

[99] Haes, A. J.; Hall, W. P.; Chang, L.; Klein, W. L.; Van Duyne, R. P. A Localized Surface Plasmon Resonance Biosensor: First Steps toward an Assay for Alzheimer's Disease, Nano Lett. **(2004)**, 4, 6, 1029

[100] Dieringer, J. A.; McFarland, A. D.; Shah, N. C.; Stuart, D. A.; Whitney, A. V.; Yonzon, C. R.; Young, M. A.; Zhang, X. Y.; Van Duyne, R. P. Surface enhanced Raman spectroscopy: new materials, concepts, characterization tools, and applications, Faraday Discuss. **(2006)**, 132,9

[101] Murray, W. A.; Suckling, J. R.; Barnes, W. L. Overlayers on Silver Nanotriangles: Field Confinement and Spectral Position of Localized Surface Plasmon Resonances, Nano Lett. **(2006)**, 6, 8, 1772

[102] Nehl, C. L.; Liao, H. W.; Hafner, J. H. Optical Properties of Star-Shaped Gold Nanoparticles, Nano Lett. **(2006)**, 6, 4, 683

[103] Kolwas, K. Plasmon Resonances in a Spherical Sodium Cluster and in a Flat Surface with a Soft Optical Edge, Appl. Phys. B: Lasers Opt. **(1998)**, 66, 467

[104] Bréchignac, C.; Connerade, J. P. The giant resonance in atoms and clusters, J. Phys. B **(1994)**, 27, 3795

[105] Peng, Y.; Marcoux, C.; Patoka, P.; Hilgendorff, M.; Giersig, M.; Kempa, K. Plasmonics of thin film quasitriangular nanoparticles, Appl. Phys. Lett. **(2010)**, 96, 133104 and references within

[106] Wang, X.; Kempa, K. Negative refraction and subwavelength lensing in a polaritonic crystal, Phys. Rev. B **(2005)**, 71, 233101

[107] Levine, H.; Schwinger, J. On the Theory of Diffraction by an Aperture in an Infinite Plane Screen, J. Phys. Rev. **(1948)**, 74, 958

[108] Bouwkamp, C. J. On Bethe's theory of diffraction by small holes, Philips Res. Rep. 1950, 5, 321; Bouwkamp, C. J. Diffraction Theory, Rep. Prog. Phys. **(1954)**, 17, 35

[109] Dürig, U.; Pohl, D. W.; Rohner, F. J. Near-field optical-scanning microscopy, Appl. Phys. **(1986)**, 59, 3318

[110] Andrews, C. L. Diffraction Pattern of a Circular Aperture at Short Distances, Phys. Rev. **(1947)**, 71, 777

[111] Kolb, G.; Karrai, K.; Abstreiter, G. Optical photodetector for near-field optics, Appl. Phys. Lett. **(1994)**, 65, 3090

[112] Ctistis, G.; Schimek, O.; Fumagalli, P.; Paggel, J. J. Polarization-dependent measurement of the near-field distribution of a waveguide with subwavelength aperture, J. Appl. Phys. **(2006)**, 99, 014505

[113] Krishnan, A.; Thio, T.; Kim, T. J.; Lezec, H. J.; Ebbesen, T. W.; Wolff, P. A.; Pendry, J.; Martin-Moreno, L.; Garcia-Vidal, F. Evanescently coupled resonance in surface plasmon enhanced transmission, J. Opt. Commun. **(2001)**, 200, 1

[114] Thio, T.; Pellerin, K. M.; Linke, R. A.; Ebbesen, T.W.; Lezec, H. J. Enhanced light transmission through a single subwavelength aperture, Opt. Lett. **(2001)**, 26, 1972

[115] Lezec, H. J.; Thio, T. Diffracted evanescent wave model for enhanced and suppressed optical transmission through subwavelength hole arrays; Opt. Express **(2004)**, 12, 16, 3629

[116] Pacifici, D.; Lezec, H. J.; Atwater, H. A.; Weiner, J. Quantitative Determination of Optical Transmission through Subwavelength Slit Arrays in Ag films: The Essential role of Surface Wave Interference and Local Coupling between Adjacent Slits, Phys. Rev. B **(2008)**, 77, 115411

[117] Brechignac, C.; Houdy, P.; Lahmani, M. Nanomaterials and Nanochemistry, Springer, Berlin **(2007)**

[118] Ricard, D. Optical Nonlinearities of Composite Materials: etc. in Nonlinear Optical Materials: Principles and Applications, (Proceedings of the International School of Physics), Varenna **(1993)**

[119] Kim, T. J.; Thio, T.; Ebbesen, T. W.; Grupp, D. E.; Lezec, H. J. Control of optical transmission through metals perforated with subwavelength hole arrays, Opt. Lett. **(1999)**, 24, 256

[120] Sarrazin, M.; Vigneron, J.-P.; Vigoureux, J.-M. Role of Wood anomalies in optical properties of thin metallic films with a bidimensional array of subwavelength holes, Phys. Rev. B **(2003)**, 67, 085415

[121] Genet, C.; van Exter, M. P.; Woerdman, J. P. Fano-type interpretation of red shifts and red tails in hole array transmission spectra, Opt. Commun. **(2003)**, 225, 331

[122] Bonod, N.; Enoch, S.; Li, L.; Popov, E.; Neviere, M. Resonant optical transmission through thin metallic films with and without holes, Opt. Express **(2003)**, 11, 482

[123] Degiron, A.; Lezec, H. J.; Barnes, W. L.; Ebbesen, T. W. Effects of hole depth on enhanced light transmission through subwavelength hole arrays, Appl. Phys. Lett. **(2002)**, 81, 4327

[124] Segall, B. Energy Bands of Aluminum, Phys. Rev. **(1961)**, 124, 1797; Brust, D. Band structure and optical properties of aluminum, Solid State Commun. **(1970)**, 8, 413

[125] Guo, C.; Rodriguez, G.; Lobad, A.; Taylor, A. J. Structural Phase Transition of Aluminum Induced by Electronic Excitation, Phys. Rev. Lett. **(2000)**, 84, 4493

[126] Ehrenreich, H.; Phillipp, J. R.; Segall, B. Optical properties of aluminum, Phys. Rev. **(1963)**, 132, 1918

[127] Ctistis, G.; Papaioannou, E.; Patoka, P.; Gutek, J.; Fumagalli, P.; Giersig, M. Optical and Magnetic Properties of Hexagonal Arrays of Subwavelength Holes in Optically Thin Cobalt Films, Nano Lett. **(2009)**, 9, 1, 1

[128] Bouhelier, A.; Huser, Th.; Freyland, J. M.; Guntherodt, H. J.; Pohl, D. W. Plasmon transmissivity and reflectivity of narrow grooves in a silver film, J. Microsc. **(1999)**, 194, 571

[129] Sönnichsen, C.; Duch, A. C.; Steininger, G.; Koch, M.; von Plessen, G. Launching surface plasmons into nanoholes in metal films, Appl. Phys. Lett. **(2000)**, 76, 140

[130] Kaupp, G.; Herrmann, A.; Haak, M. Artifacts in scanning near-field optical microscopy (SNOM) due to deficient tips. Journal of Physical Organic Chemistry **(1999)**, 12, 797

[131] Taflove, A. Computational Electrodynamics: The Finite-Difference Time-Domain Method, 2nd ed., Artech House: Norwood, MA **(2000)**

[132] Ctistis, G.; Patoka, P.; Wang, X.; Kempa, K.; Giersig, M. Optical transmission of subwavelength hole arrays in thin metal films, Nano Lett. **(2007)**, 7, 9, 2926

[133] Palik, E. D. Handbook of Optical Constants in Solids Vol.1, Academic Press: Boston **(1991)**

[134] Weiner, J. Phase shifts and interference in surface plasmon polariton waves, Opt. Express **(2008)**, 16, 2, 950

[135] Astilean, S.; Lalanne, Ph.; Palamaru, M. Light transmission through metallic channels much smaller than the wavelength, Opt. Commun. **(2000)**, 175, 265

[136] Wang, B.; Lalanne, P. How many surface plasmons are locally excited on the ridges of metallic lamellar gratings?, Appl. Phys. Lett. **(2010)**, 96, 051115

[137] Treacy, M. M. J. Dynamical diffraction in metallic optical gratings, Appl. Phys. Lett. **(1999)**, 75, 5, 606

[138] Palamaru, M. Astilean, S. Sub-wavelength Metallic Gratings of Very High Transmission Efficiency, Journal of Optoelectronics and Advanced Materials **(1999)**, 1, 2, 35

[139] Benabbas, A.; Halté, V.; Bigot, J.-Y. Analytical model of the optical response of periodically structured metallic films, Opt. Express **(2005)**, 13, 22, 8730

[140] Chen, Y.-B.; Chen, J.-S.; Hsu, P-F. Impacts of geometric modifications on infrared optical responses of metallic slit arrays, Opt. Express **(2009)**, 17, 9803

[141] Hessel, A.; Oliner, A.A. Wood's Anomaly Effects on Gratings of Large Amplitude, Opt. Commun. **(1986)**, 59, 5, 6

[142] Treacy, M. M. J. Dynamical diffraction explanation of the anomalous transmission of light through metallic gratings, Phys. Rev. B **(2002)**, 66, 195105

[143] Garcia-Vidal, F. J.; Martin-Moreno, L. Transmission and focusing of light in one dimensional periodically nanostructured metals, Phys. Rev. B (2002), 66, 155412

[144] Barnes, W. L.; Preist, T. W.; Kitson, S. C.; Sambles, J. R. Physical origin of photonic energy gaps in the propagation of surface plasmons on gratings, Phys. Rev. B. **(1996)**, 54, 9, 1654

[145] Popov, E.; Bonod, N.; Enoch, S. Non-Bloch plasmonic stop-band in real-metal gratings, Opt. Express **(2007)**, 15, 10, 6241

[146] Palamaru, M. Astilean, S. Sub-wavelength Metallic Gratings of Very High Transmission Efficiency, Journal of Optoelectronics and Advanced Materials **(1999)**, 1, 2, 35

[147] Moreno, E.; Martin-Moreno, L.; Garcia-Vidal, F. J. Extraordinary optical transmission without plasmons: the s-polarization case, J. Opt. A: Pure Appl. Opt. **(2006)**, 8, S94–S97

[148] Crouse, D.; Keshavareddy, P. Polarization independent enhanced optical transmission in one-dimensional gratings and device applications, Opt. Express **(2007)**, 15, 1415

[149] Cao, Q.; Lalanne, P. Negative Role of Surface Plasmons in the Transmission of Metallic Gratings with Very Narrow Slits, Phys. Rev. Lett. **(2002)**, 88, 5, 057403

[150] Zhang, J.; Cai, L.; Bai, W.; Xu, Y.; Song, G. Slow light at terahertz frequencies in surface plasmon polariton assisted grating waveguide, J. Appl. Phys.**(2009)**, 106, 103715

[151] Schider, G.; Krenn, J. R.; Gotschy, W.; Lamprecht, B.; Ditlbacher, H.; Leitner, A.; Aussenegg, F. R. Optical properties of Ag and Au nanowire gratings, J. Appl. Phys. **(2001)**, 90, 8, 15

[152] Crouse, D.; Keshavareddy, P. Role of optical and surface plasmon modes in enhanced transmission and applications, Opt. Express **(2005)**, 13, 20, 7760

[153] Guillaumée, M.; Nikitin, A. Yu.; Klein, M. J. K.; Dunbar, L. A.; Spassov, V.; Eckert, R.; Martín-Moreno, L.; García-Vidal, F. J.; Stanley, R. P. Observation of enhanced transmission for s-polarized light through a subwavelength slit, Opt. Express **(2010)**, 18, 9, 9722

[154] Crouse, D.; Jaquay, E.; Maikal, A.; Hibbins, A. P. Light circulation and weaving in periodically patterned structures, Phys. Rev. B **(2008)**, 77, 195437

[155] Kang, M.-G.; Kim, M.-S.; Kim, J.; Guo, L. J. Organic Solar Cells Using Nanoimprinted Transparent Metal Electrodes, Adv. Mater. **(2008)**, 20, 4408

[156] Liang, Z.; Jing, L.; Cheng-Fang, L.; Fei, Z. A Novel Nano-grating Structure of Polarizing Beam Splitters, Chin. Phys. Lett. **(2006)**, 23, 7

[157] Christ, A.; Tikhodeev, S.G.; Gippius, N. A.; Kuhl, J.; Giessen, H. Waveguide-Plasmon Polaritons: Strong Coupling of Photonic and Electronic Resonances in a Metallic Photonic Crystal Slab, Phys. Rev. Lett. **(2003)**, 91, 183901

[158] Lochbihler, H. Colored images generated by metallic subwavelength gratings, Opt. Express **(2009)**, 17, 14

[159] Zhang, X.; Liu, H.; Tian, J.; Song, Y.; Wang, L.; Song, J.; Zhang, G. Optical polarizers based on gold nanowires fabricated using colloidal gold nanoparticles, Nanotechnology **(2008)**, 19, 285202

[160] Zhang, X.; Liu, H.; Tian, J.; Song, Y.; Wang, L. Band-Selective Optical Polarizer Based on Gold-Nanowire Plasmonic Diffraction Gratings, Nano Lett. **(2008)**, 8, 9, 2653

[161] Hsu, S.-Y.; Lee, M.-Ch. Extraction enhancement in organic light emitting devices by using metallic nanowire arrays, Appl. Phys. Lett. **(2008)**, 92, 013303

[162] Lochbihler, H. Enhanced transmission of TE polarized light through wire gratings, Phys. Rev. B **(2009)**, 79, 245427

[163] Kang, M.; Li, Y.; Lou, K.; Li, S.-M.; Bai, Q.; Chen, J.; Wang, H.-T. Second-harmonic generation in one-dimensional metal gratings with dual extraordinary transmissions, J. Appl. Phys. **(2010)**, 107, 053108

[164] Lochbihler, H.; Depine, R. Highly conducting wire gratings in the resonance region, Applied Optics **(1993)**, 32, 19

[165] Singh, B. K.; Hillier, A. C. Surface Plasmon Resonance Enhanced Transmission of Light through Gold-Coated Diffraction Gratings, Anal. Chem. **(2008)**, 80, 3803

[166] Schröter, U.; Heitmann, D. Surface-plasmon-enhanced transmission through metallic gratings, Phys. Rev. B **(1998)**, 58, 23

[167] Linden, S.; Kuhl, J.; Giessen, H. Controlling the Interaction between Light and Gold Nanoparticles: Selective Suppression of Extinction, Phys. Rev. Lett. **(2001)**, 86, 4688

[168] Sun, Z.; Jung, S.-Y.; Kim, H.-K. Role of surface plasmons in the optical interaction in metallic gratings with narrow slits, Appl. Phys. Lett. **(2003)**, 83, 15

[169] Plyler, E. K. The infrared Absorption Bands of Water Vapor, Phys. Rev. **(1932)**, 39, 77

[170] Ditlbacher, H.; Hohenau, H.; Wagner, D.; Kreibig, U.; Rogers, M.; Hofer, F.; Aussenegg, F. R.; Krenn, J. R. Silver Nanowires as Surface Plasmon Resonators, Phys. Rev. Lett. **(2005)**, 95, 257403

[171] Ctistis, G.; Papaioannou, E.; Patoka, P.; Gutek, J.; Fumagalli, P.; Giersig, M. Optical and Magnetic Properties of Hexagonal Arrays of Subwavelength Holes in Optically Thin Cobalt Films, Nano Lett. **(2009)**, 9, 1

List of publications

1. Patoka, P.; Skeren, T.; Hilgendorff, M.; Zhi, L., Paudel, T.; Kempa, K.; Giersig, M. *Tuning plasmonic resonances in magnetic nanocavities*, submitted to NanoLetters

2. Torrado, J. F.; Papaioannou, E. Th.; Ctistis, G.; Patoka, P.; Giersig, M.; Armelles, G.; Garcia-Martin, A. *Plasmon induced transverse magneto-optical effects in Fe antidot arrays,* Phys. Status Solidi RRL **(2010)**, 4, 10, 271

3. Peng, Y.; Marcoux, C.; Patoka, P.; Hilgendorff, M.; Giersig, M.; Kempa, K. *Plasmonics of thin film quasitriangular nanoparticles,* Appl. Phys. Lett. **(2010)**, 96, 133104

4. Papaioannou, E. Th.; Kapaklis, V.; Patoka, P.; Giersig, M.; Fumagalli, P.; Garcia-Martin, A.; Ferreiro-Vila, E.; Ctistis, G. *Magneto-optic enhancement and magnetic properties in Fe antidot films with hexagonal symmetry,* Phys. Rev. B **(2010)**, 81, 054424

5. Bayati, M.; Patoka, P.; Giersig, M.; Savinova, E. R. *An Approach to Fabrication of Metal Nanoring Arrays,* Langmuir **(2010)**, 26, 5, 3549

6. Ctistis, G.; Papaioannou, E.; Patoka, P.; Gutek, J.; Fumagalli, P.; Giersig, M. *Optical and Magnetic Properties of Hexagonal Arrays of Subwavelength Holes in Optically Thin Cobalt Films,* Nano Lett. **(2009)**, 9, 1, 1

7. Gwinner, M. C.; Koroknay, E.; Fu, L.; Patoka, P.; Kandulski, W.; Giersig, M.; Giessen, H. *Periodic Large-Area Metallic Split-Ring Resonator Metamaterial Fabrication Based on Shadow Nanosphere Lithography,* Small **(2009)**, 5, 400

8. Ctistis, G.; Patoka, P.; Wang, X.; Kempa, K.; Giersig, M. *Optical transmission of subwavelength hole arrays in thin metal films*, Nano Lett. **(2007)**, 7, 9, 2926

Conference contributions

Talks:

1. Patoka, P.; Ctistis, G.; Hilgendorff, M.; Fumagalli, P.; Giersig, M.
   Nanomaterials – their structural and optical characterization
   VI Seminar on STM/AFM
   December 1 – 5, 2010, Zakopane, Poland
2. Patoka, P.; Ctistis, G.; Hilgendorff, M.; Fumagalli, P.; Giersig, M.
   Structural and optical properties of Gold and Iron nanowires
   Spring meeting of the German Physical Society
   March 21 – 26, 2010, Regensburg, Germany
3. Patoka, P.; Ctistis, G.; Giersig, M.
   Structural and Optical Properties of Gold Nanolines
   E-MRS Fall Meeting
   September 15-19, 2008, Warsaw, Poland
4. Ctistis, G.; Papaioannou, E.; Patoka, P; Fumagalli, P.; Giersig, M.
   Optic and magnetic properties of Co films with subwavelength hole array
   CLEO Europe 2009
   June 15-19, 2009, Munich, Germany
5. Ctistis, G.; Papaioannou, E.; Patoka, P; Gutek, J.; Fumagalli, P.; Giersig, M.
   Optical and magnetic properties of hexagonal arrays of subwavelength holes in thin metal films
   SPIE Optics & Photonics
   August 11-15, 2008, San Diego, USA
6. Ctistis, G.; Papaioannou, E.; Patoka, P; Gutek, J.; Fumagalli, P.; Giersig, M.
   Magneto-optical study of hexagonal hole arrays in thin magnetic films
   Spring meeting of the German Physical Society
   February 25-29, 2008, Berlin, Germany
7. Ctistis, G. ;Patoka, P.; Giersig, M.
   Optical transmission through hexagonal sub-wavelength hole arrays in thin metal films
   Spring meeting of the German Physical Society
   March 26-30, 2007, Regensburg, Germany

Posters:

1. Patoka, P.; Ctistis, G.; Hilgendorff, M.; Fumagalli, P.; Giersig, M.
   Nanomaterials and Their Potential Application in Optics
   Colloquium: French-German Research: 50 Years in The Light of The Laser
   November 5-6, 2010, Berlin, Germany
2. Papaioannou, E.; Ctists, G.; Patoka, P.; Giersig, M.; Fumagalli, P.
   Magnetic properties of nanohole arrays of Co, Fe and Ni thin films
   International Colloquium on Magnetic Films and Surfaces (ICMFS)
   July 20 - 24, 2009, Berlin, Germany
3. Ctistis, G.; Patoka, P.; Rybczyński, J.; Kempa, K.; Giersig, M.
   Creation of nanostructures and their light transmission
   International Conference On Nanoscience and Nanotechnology (ICONN)
   February 25-29, 2008, Melbourne, Victoria, Australia
4. Ctists, G.; Patoka, P.; Wang, X.; Kempa, K.; Giersig, M.
   Optical transmission through hexagonal sub-wavelength hole arrays in thin metal films
   Third International Conference on Surface Plasmon Photonics (SPP3)
   June 17-22, 2007, Dijon, France

Acknowledgement

On this page I would like to acknowledge my gratitude to a number of different people without who, this work could not be realized. First of all I would like to thank my supervisor Prof. Dr. Michael Giersig for introducing me to the fascinating world of nanodimensions, for giving me the opportunity to do this study, and for always keeping me motivated and supporting me with useful advice. I am particularly grateful to Prof. Dr. Stephanie Reich for accepting to be a co-referee of this thesis. My special thanks goes to Dr. Georgios Ctistis, for fruitful collaboration and most important for his help and guidance, without which this thesis wouldn't have taken the present shape.
Separately I would like to thank Prof. Dr. Paul Fumagalli for giving me the opportunity to finish my thesis in his group. I thank Dr. Michael Hilgendorff for many essential discussions and support with his deep knowledge in chemistry and guidance throughout the work in the chemical laboratory. I am grateful to Prof. Dr. Kris Kempa for many valuable discussions and for providing theoretical calculations, which brought more understanding. I would like to thank Prof. Dr. Marcus Antonietti and Prof. Dr. Helmut Möhwald from the Max Planck Institute in Golm (Germany) for their financial support.
My gratitude goes also to the Helmholtz-Zentrum Berlin für Materialien und Energie GmbH for their financial support. I would like to also express my gratitude to Soliton GmbH company especially to Dr. Toni Beckmann for financial support in final stage of preparation of this thesis. I thank Dr. Dang Sheng Su and Mrs. Gisela Weinberg for help in SEM measurements. Thanks to present and past members of the caesar institute in Bonn, where most of the experimental part of this work had been done. Especially I would like to thank Peter Holik and Rene Borowski who helped me during my work in the clean room. Many special thanks goes to my office mates Bjorn Lewitz and Michael Karcher, and to Axel Luchterhand and Tobias Homberg for their help not only in scientific issues and for a great atmosphere during my stay at the Freie Universität. I would like to express my gratitude to my parents Lidia and Mieczysław who always support me and encouraged me with their best wishes.
Separately I would like to thank to my parents-in-law Teresa and Krzysztof for giving me a continuous boost and help.
Finally I would like to thank to my wife Anna without whom this effort would have been worth nothing. Your love, support and constant patience have taught me so much.

Abstract

In this thesis we investigate the structural as well as optical properties of our by means of nanosphere lithography fabricated nanostructures. We can thereby control the fabrication process to get arrays of nanostructures such as quasitriangular shaped nanoislands, subwavelength holes, as well as grating like oriented nanowires.

The various structural characterization methods presented here revealed a crucial dependence of the sample preparation process on the final form of the structure. It could be demonstrated that by changing the sphere size of the mask building polystyrene latex spheres and by altering the material deposition angle, the geometry of the structure could be controlled. As deposition materials, however, we carefully chose three metals: Gold for its well known and desired plasmonic response, aluminum as a “lossy” metal, and iron for its magnetic properties.

The optical characterization of the samples was carried out in the far as well as in the near field. We used therefore standard spectroscopic techniques and near-field optical microscopy. The studies revealed that the optical response of the gold samples was mainly due to the coupling of the light to surface plasmons. This excitation of surface plasmon polaritons was responsible for the measured enhanced transmission of the light through, e.g., our subwavelength hole arrays. Furthermore we could show that the plasmonic response can be controled by judicious choice of structure morphology.

Kurzfassung

In dieser Arbeit werden strukturelle und optische Eigenschaften unserer durch Nanosphere-Lithographie erstellten Nanostrukturen untersucht. Mit Hilfe dieser Methode können wir den Wachstumsprozess beeinflussen, um verschiedene nanostrukturierte Oberflächen, wie zum Beispiel quasi-dreieckige Nanoinseln, Sub-Lambda-Löcher (Löcher mit einem Durchmesser kleiner als die Wellenlänge des Lichtes) und gitterartig ausgerichtete Nanodrähte zu erhalten. Die verschiedenen in der Arbeit vorgestellten strukturellen Untersuchungsmethoden zeigen eine starken Einfluss des Präparationsvorgangs auf die sich ergebende Morphologie sowie den daraus resultierenden Eigenschaften der Nanostrukturen. Es konnte gezeigt werden, dass durch die Wahl der Größe der Polystyrol-Kugeln aus denen die Maske besteht, sowie Veränderung des Aufdampfwinkels die Geometrie der Struktur kontrolliert beeinflusst werden kann. Als Materialien für die Schicht wurden bewusst drei verschiedene Metalle gewählt: Gold wegen seiner gut bekannten und erwünschten optischen und plasmonischen Eigenschaften, Aluminium als optisch dämpfendes Metall und Eisen wegen seiner magnetischen Eigenschaften.

Die optische Charakterisierung der Proben wurde sowohl im Fern- wie im Nahfeld durchgeführt. Es wurden spektroskopische Standardverfahren und Nahfeldmikroskopie verwendet. Im Verlauf er Arbeit wurde nachgewiesen, dass die optische Antwort der Goldproben von der Wechselwirkung zwischen Licht und Oberflächenplasmonen bestimmt wird. Die Anregung von Plasmon-Polaritonen führt zu der gemessenen verstärkten Transmission durch Strukturen wie den periodischen Sub-Lambda-Löchern. Außerdem konnte gezeigt werden, dass die plasmonische Antwort durch Wahl einer passenden Morphologie gezielt beeinflusst werden kann, wodurch sich viele Anwendungsperspektiven ergeben.

Curriculum Vitae

Der Lebenslauf ist in der Online-Version aus Gründen des Datenschutzes nicht enthalten.